TECHNISCHE
UNIVERSITÄT
WIEN

DISSERTATION

Three-particle correlations and where to find them

ausgeführt am Institut für Festkörperphysik
der Technischen Universität Wien

unter der Anleitung von
Univ.Prof. Dipl.-Phys. Dr.rer.nat. Karsten Held

durch

Patrick Michael Kappl

December 8, 2023 _____

Abstract

Strongly correlated electron systems offer exciting and interesting physics but also great theoretical and numerical challenges. Independent (quasi-)particles are insufficient to describe them and in the language of Feynman diagrammatics vertex corrections have to be taken into account. Hitherto such corrections have by and large only been studied up to the two-particle level. The present thesis, however, looks beyond that and into the realm of electronic correlations on the level of three-particle Feynman diagrams. For this, it is necessary to generalize many concepts and terms that are well-known and understood on the two-particle level. The diagrammatic representation and decomposition of the three-particle Green's function is studied and the fully connected three-particle vertex is introduced. We also present the expansion of the three-particle Green's function in terms of the full two-particle vertex and compute its first few terms.

A possible option to make numerics easier is to restrict ourselves to bosonic three-particle correlators. These only have two instead of five frequency or time arguments. More importantly, however, they are required for nonlinear response theory and thus provide a physical application for three-particle corrections. Numerical simulations for an Anderson impurity model and Hubbard model are used to find areas where such response functions in second order in the applied fields become sizeable. It turns out that in these parameter regimes simple approximations with bare or bubble-like diagrams yield bad results and three-particle vertex corrections must indeed be considered.

The next chapter of this thesis focuses on three-particle ladders. After generalizing the Bethe–Salpeter equation to three particles, an approximation for the three-particle ladder is introduced. It is built as a geometric series of diagrams based only on irreducible two-particle vertices and Green's function lines. The numerical results computed for an Anderson impurity model (AIM) are not very rewarding, though. They are only qualitatively good for small values of the local Coulomb interaction.

Finally, statistical error estimation of post-processed quantum Monte Carlo quantities is studied. Specifically, the error propagation through diagrammatic equations on the one- and two-particle level, is analyzed. This is not directly tied to three-particle correlations and based on an earlier project. However, since most numerical results in this thesis are based on dynamical mean-field theory calculations, error estimations for the self-energy turned out to be generally very useful.

Zusammenfassung

Stark korrelierte Elektronensysteme bergen spannende und interessante Physik aber auch große theoretische und numerische Herausforderungen. Unabhängige (Quasi-)Teilchen reichen nicht mehr aus um sie zu beschreiben und Vertexkorrekturen, wie sie in der Sprache der Feynman-Diagrammatik heißen, müssen berücksichtigt werden. Bisher sind solche Korrekturen weitestgehend nur auf dem Ein- und Zweiteilchenniveau untersucht worden. Die vorliegende Dissertation blickt jedoch über diesen Tellerrand hinaus und in das Reich der elektronischen Korrelationen der Dreiteilchendiagramme. Dafür werden die Terminologie und die Konzepte, die bereits vom Zweiteilchenniveau bekannt sind, auf drei Teilchen verallgemeinert. Die diagrammatische Darstellung und Zerlegung der Dreiteilchen-Green'schen-Funktion werden untersucht und der volle, verbundene Dreiteilchenvertex wird eingeführt. Weiters wird die Entwicklung der Dreiteilchen-Green'schen-Funktion bezüglich dem vollen Zweiteilchenvertex vorgestellt und die ersten Terme werden berechnet.

Eine Möglichkeit um die Numerik zu vereinfachen ist es, dass wir uns auf bosonische Dreiteilchenkorrelatoren beschränken. Diese haben nur zwei anstatt fünf Frequenz- oder Zeitargumente. Viel wichtiger ist jedoch, dass sie für die Berechnung nichtlinearer Antwortfunktionen verwendet werden können und somit eine physikalische Anwendung für Dreiteilchenkorrekturen darstellen. Mithilfe von numerischen Simulationen werden für ein Anderson-Impurity-Modell und ein Hubbard-Modell Parameterbereiche gesucht in denen die Antwortfunktionen in zweiter Ordnung in den externen Feldern möglichst groß sind. Wie sich herausstellt, sind einfache Approximation die nur aus Green'schen Funktionen bestehen in diesen Bereichen nicht ausreichend. Echte Dreiteilchenkorrekturen müssen berücksichtigt werden.

Im nächsten Kapitel liegt der Fokus auf Dreiteilchenleitern. Nach der Verallgemeinerung der Bethe-Salpeter-Gleichung auf drei Teilchen, wird eine Approximation für die Dreiteilchenleiter vorgestellt. Diese basiert auf einer geometrischen Reihe von irreduziblen Zweiteilchenvertices und Green'schen Funktionslinien. Leider bleiben die numerischen Ergebnisse, die für ein Anderson-Impurity-Modell berechnet wurden, hinter den Erwartungen. Sie sind nur qualitativ gut und das bei kleinen Werten der lokalen Coulomb-Wechselwirkung.

Schließlich wird noch die statistische Fehlerschätzung bei der Weiterverarbeitung von Quantum-Monte-Carlo-Größen untersucht. Genauer gesagt wird die Fehlerfortpflanzung durch diagrammatische Gleichungen am Ein- und Zweiteilchenniveau analysiert. Dies steht nicht in direkter Verbindung zu Dreiteilchenkorrelationen, sondern basiert auf einem früheren PhD-Projekt des Autors. Da jedoch die meisten numerischen Ergebnisse dieser Dissertation auf Berechnungen mit der dynamischen Molekularfeld-Theorie aufbauen, stellt sich die Fehlerschätzung für die Selbstenergie im Allgemeinen als äußerst nützlich heraus.

Contents

Abbreviations and acronyms vii

1. Introduction 1

2. Theoretical background 5
- 2.1. One-particle Green's function . . . 5
- 2.2. Feynman diagrams . . . 8
- 2.3. Self-energy . . . 11
- 2.4. Two-particle Green's function . . . 12
- 2.5. Full two-particle vertex . . . 14
- 2.6. Irreducible two-particle vertices . . . 15
- 2.7. Schwinger–Dyson equations . . . 17
- 2.8. Nonlinear response theory . . . 18

3. Models and methods 21
- 3.1. Anderson impurity model . . . 21
- 3.2. Hubbard model . . . 22
- 3.3. Dynamical mean-field theory . . . 22
- 3.4. Beyond DMFT: dynamical vertex approximation . . . 25

4. Three-particle Green's function 27
- 4.1. Definition . . . 27
- 4.2. Frequency notations . . . 28
- 4.3. Spin components and symmetries . . . 29
- 4.4. Decomposition . . . 33
- 4.5. Vertex expansion . . . 34

5. Three-particle correlators and nonlinear response 45
- 5.1. Introduction . . . 45
- 5.2. Theory . . . 47
- 5.3. Models . . . 51
- 5.4. Results . . . 53
- 5.5. Conclusion . . . 66
- 5.6. Outlook . . . 66

6. Three-particle ladder 69
- 6.1. Three-particle Bethe–Salpeter-like equations . . . 69

6.2. Approximate three-particle ladder . . . 72
6.3. Numerical results . . . 82
6.4. Conclusion and outlook . . . 89

7. Statistical error estimation with jackknife **91**
7.1. Introduction . . . 91
7.2. Methods . . . 92
7.3. Statistical analysis of the input: two-particle Green's function . . . 100
7.4. Self-energy . . . 102
7.5. Susceptibilities . . . 106
7.6. Maximum entropy analytic continuation . . . 110
7.7. Conclusion and discussion . . . 112

8. Summary and outlook **115**

A. Supplemental material: three-particle correlators and nonlinear response **117**
A.1. From spin correlators to second-order response functions . . . 117
A.2. Lehmann formula for the three-particle correlator . . . 119
A.3. Asymptotic behavior of $\chi^{(2)}$ . . . 120

Acknowledgements **123**

List of publications **125**

Bibliography **127**

Abbreviations and acronyms

1PI one-particle irreducible 11, 15, 23, 25, 70–72, 79

1PR one-particle reducible 11, 70, 72, 79, 82

2PI two-particle irreducible 71, 72

2PR two-particle reducible 70

3PI three-particle irreducible 70–72

3PR three-particle reducible 70, 71

ADGA ab initio dynamical vertex approximation 93, 96, 99, 100, 103

AIM Anderson impurity model iii, 21–26, 45, 47, 51, 53, 54, 57–61, 64–66, 93, 115, 121

CT-HYB continuous-time quantum Monte Carlo in the hybridization expansion 25, 93, 112

DFT density functional theory 1

DΓA dynamical vertex approximation 25, 26, 91–93, 96, 97, 99, 100, 102–106, 108, 112, 113, 115

DMFT dynamical mean-field theory iii, 1, 12, 21–26, 45–47, 53, 66, 82, 84, 91–93, 95–97, 100, 102–109, 112, 113, 115, 116

DOS density of states 22, 53, 59–61, 64–66

ED exact diagonalization 25, 53, 54, 57, 58, 69, 84–87

HM Hubbard model iii, 14, 22–26, 46, 47, 51, 53, 65, 66, 82, 100, 102, 106, 115

QFT quantum field theory 2, 5, 8, 45

QMC quantum Monte Carlo iii, 3, 25, 53, 54, 57, 58, 66, 82, 91–93, 97, 100, 102, 103, 106, 112, 116

SEM standard error of the mean 98, 102–104, 108, 113

1. Introduction

"The whole is greater than the sum of its parts." Most people will probably connect this saying with seminars about synergy, or have heard it at team building events. However, in physics, more specifically many-body physics, this wisdom also holds true [1]. In general, a system of n particles cannot be described as n single-particle systems. Why? Because there are interactions and the particles influence one another. This makes life very difficult for solid-state physicists. Due to the huge amount of particles typically interacting in solids, exact solutions, even numerical ones, are basically impossible to find.

However, when big numbers are involved, statistics can often help. If the interaction between the electrons is weak enough, we can average it and describe it by a mean charge field through which a single electron moves. These mean-field methods, most famously density functional theory (DFT) employed with current, approximate exchange–correlation functionals, have been successfully applied to many problems and materials over the past decades. For some systems, however, they fail miserably: the mean-field is no longer an accurate description as the strong interaction between the electrons becomes important. In more mathematical terms, this means that in such a system the expectation value of two observables does not factorize, i.e.,

$$\langle \hat{A}\hat{B} \rangle \neq \langle \hat{A} \rangle \langle \hat{B} \rangle. \tag{1.1}$$

The difference between the two sides of the inequality is called correlation, and systems with a sizable difference are aptly named strongly correlated systems. They can show a plethora of fascinating phenomena based on collective behavior such as Mott–Hubbard metal–insulator transitions, heavy fermion behavior, and, probably most famously, unconventional superconductivity. However, strong correlations do not only lead to such exciting and interesting effects, but also make their theoretical treatment notoriously difficult. Independent (quasi-)particles are insufficient to describe the relevant physics and corrections due to scattering of (quasi-)particles have to be taken into account.

In the language of Feynman diagrammatics these corrections are called vertex corrections, and they are often categorized by the number of particles involved. By and large such corrections are only considered up to the two-particle level. In the one-particle case they help us describe, e.g, quasiparticle renormalizations, and metal–insulator transitions, while two-particle vertex corrections modify linear response functions of the system. Dynamical mean-field theory (DMFT) also relies on Feynman diagrams with one in- and outgoing particle, while its diagrammatic extensions incorporate two-particle vertices as

well. Correlations beyond the two-particle level, however, are for the most part terra incognita. After exploratory forays into this area [2–4] the goal of the present thesis is to be the second proper expedition to these unexplored lands, generalizing existing theoretical frameworks and formalisms, and finding out what physical insights await

The outline of the present thesis is as follows:

Chapter 2 recapitulates theoretical formalisms and concepts necessary for the later chapters. This includes first and foremost methods of quantum field theory (QFT) for many-electron systems. We discuss one- and two-particle Green's functions and use the Matsubara formalism to deal with finite temperatures. Feynman diagrams are introduced since they play an important role throughout this thesis. We also shed light on some topological properties of one- and two-particle diagrams. At the end, a short derivation of nonlinear response theory necessary for chapter 5 is given.

Chapter 3 introduces, on the one hand, the models used in this thesis to study three-particle correlations, and on the other hand, the methods employed to solve them. We briefly recall the most important facts and equations, but do not focus on implementation details and numerics.

Chapter 4 lays the foundation for this thesis by studying the theoretical aspects of the three-particle Green's function. Definitions, properties, and concepts from the one- and two-particle level are generalized, and we see that channels, notations, symmetries, and decompositions all get more complex. The three-particle level also allows a new form of expansion of the full vertex, for which the first few orders are calculated.

Chapter 5 focuses on bosonic three-particle correlators. Since they have fewer time and frequency arguments than the full three-particle Green's function they are much easier to handle numerically. The most important aspect is, however, that they provide a physical application for three-particle corrections: nonlinear response theory. We scan the parameter space of our models to find regimes with large second-order response functions.

Chapter 6 goes back to the full three-particle vertex and tries to represent it as a geometric series of diagrams. As it turns out a Bethe–Salpeter-like equation is much more difficult to find on the three-particle level than on the two-particle one. Therefore, an ad-hoc approximation based on intuition from two-particle ladders is derived and studied.

Chapter 7 is a bit of an outlier as it does not discuss three-particle correlations. Instead, it focuses on an earlier project about statistical error estimation of post-processed quantum Monte Carlo (QMC) quantities. Specifically, it studies the error propagation through diagrammatic equations on the one- and two-particle level, namely the Dyson and Bethe–Salpeter equations.

Chapter 8 finally gives a summary of the most important achievements of this thesis. It also provides an outlook and lists some unanswered questions.

Acknowledgements and a list of publications are found at the end, after the appendix. Throughout the thesis, vertical bars mark parts taken from already published work by the author.

Units

At this point let us make a short comment about units. In his book *Quantum field theory in a nutshell*, A. Zee writes: "For the same reason we no longer use a certain king's feet to measure distance we use natural units in which the speed of light c and the Dirac symbol $\hbar$ are both set equal to 1." [5] We fully agree with him and additionally set the Boltzmann constant k_B and the Bohr magneton μ_B to 1.

2. Theoretical background

> It is well known to those who know well.
>
> Peter van Nieuwenhuizen

In this chapter we introduce and recapitulate the theoretical background that is necessary to explain the methods in chapter 3, upon which the main part of this thesis builds. This contains many-body quantum field theory (QFT) at finite temperature, Green's functions, the Matsubara formalism, and Feynman diagrams. We start with the one-particle Green's function or propagator G_1 which we also use to explain how to get from quantum mechanical expectation values to Feynman diagrams. This allows us to discuss some topological properties, like reducibility. The two-particle level is, however, where the diagrammatics really start to get interesting. After a general discussion about the two-particle Green's function G_2 we perform decompositions based on topological properties of the Feynman diagrams. This leads us right to the parquet equation, the Bethe–Salpeter equations and the Schwinger–Dyson equations. In the last section we study nonlinear response theory and its connection to n-particle correlation functions.

2.1. One-particle Green's function

Green's functions, also called propagators, are the theoretical work horse of this thesis. For the most part we are concerned with finding ways to compute them for certain many-body problems, study their symmetries and properties, and connect them to experimental observables. Since we want to do our QFT calculations at finite temperature we use the so-called Matsubara formalism [6], where we perform a Wick rotation [7] $t \to -\mathrm{i}\tau$ from real times t to imaginary times τ. This allows us to interpret the Boltzmann factor $\mathrm{e}^{-\beta\hat{H}}$ in thermal expectation values as just another imaginary time evolution. As we will see later when introducing Feynman diagrams this turns out to be very convenient.

In second quantization, at finite temperature, and in imaginary times the one-particle Green's function G_1 is defined as

$$G_{1,12}(\tau_1, \tau_2) := (-1)^1 \langle \mathrm{T}\, \hat{c}_1(\tau_1) \hat{c}_2^\dagger(\tau_2) \rangle, \tag{2.1}$$

where $\langle ... \rangle = \mathrm{Tr}\, \mathrm{e}^{-\beta\hat{H}} ...$ denotes the thermal expectation value at inverse temperature $\beta = 1/T$ with respect to the full Hamiltonian $\hat{H}$, and T is the time-ordering operator.

Furthermore, $\hat{c}_i(\tau)$ and $\hat{c}_i^\dagger(\tau)$ are the annihilation and creation operators at time τ with all other degrees of freedom like lattice site, spin, or orbital condensed into a single flavor index i. This definition means that the Green's function measures the probability amplitude for an electron with flavor 2 to appear at τ_2, and one of flavor 1 to vanish at τ_1. The usual interpretation is that an electron propagates from 2 to 1, hence also the name propagator.

If the Hamiltonian of the system is time translation invariant one can show that the Green's function only depends on a single imaginary time argument [8]

$$G_1(\tau_1, \tau_2) = G_1(\tau_1 - \tau_2, 0) =: G_1(\tau). \tag{2.2}$$

Similarly, if the Hamiltonian is invariant under translation by a lattice vector $\mathbf{R}$ it only depends on a single lattice site parameter [8]

$$G_1^{\mathbf{R}_1\mathbf{R}_2} = G_1^{\mathbf{R}_1-\mathbf{R}_2\,\mathbf{0}} =: G_1^{\mathbf{R}}. \tag{2.3}$$

Both those symmetries hold for the Hamiltonians used in this thesis (see chapter 3). They are also SU(2) symmetric which means that in the paramagnetic phase the one-particle Green's function is also independent of spin: $G_{1,\uparrow\uparrow} = G_{1,\downarrow\downarrow} = G_1$.

With lattice systems it is often most convenient to work in the reciprocal space, where the one-particle Green's function is periodic in the first Brillouin zone and can therefore be represented as a Fourier series:

$$G_1(\mathbf{k}_1, \mathbf{k}_2) = \sum_{\mathbf{R}_1}\sum_{\mathbf{R}_2} \mathrm{e}^{\mathrm{i}\mathbf{R}_1\mathbf{k}_1}\mathrm{e}^{-\mathrm{i}\mathbf{R}_2\mathbf{k}_2} G_1^{\mathbf{R}_1\mathbf{R}_2}. \tag{2.4}$$

Using eq. (2.3), i.e., translation invariance in real space, we can rewrite this as

$$\begin{aligned} G_1(\mathbf{k}_1, \mathbf{k}_2) &= \sum_{\mathbf{R}_1}\sum_{\mathbf{R}_2} \mathrm{e}^{\mathrm{i}\mathbf{R}_1\mathbf{k}_1}\mathrm{e}^{-\mathrm{i}\mathbf{R}_2\mathbf{k}_2} G_1^{\mathbf{R}_1-\mathbf{R}_2} \\ &= \sum_{\mathbf{R}_2} \mathrm{e}^{-\mathrm{i}\mathbf{R}_2(\mathbf{k}_2-\mathbf{k}_1)} \sum_{\mathbf{R}=\mathbf{R}_1-\mathbf{R}_2} \mathrm{e}^{\mathrm{i}\mathbf{R}\mathbf{k}_1} G_1^{\mathbf{R}} \\ &=: V_{\mathrm{BZ}}\delta(\mathbf{k}_1 - \mathbf{k}_2) G_1(\mathbf{k_1}) \end{aligned} \tag{2.5}$$

where V_{BZ} is the volume of the first Brillouin zone, and we introduce the single-momentum Green's function $G_1(\mathbf{k})$ in the last line. The formula for the Fourier coefficients is what gets us back from reciprocal to real space. It is given by

$$G_1^{\mathbf{R}} = \frac{1}{V_{\mathrm{BZ}}} \int_{\mathrm{BZ}} \mathrm{d}\mathbf{k}\, \mathrm{e}^{-\mathrm{i}\mathbf{R}\mathbf{k}} G_1(\mathbf{k}). \tag{2.6}$$

We can do a similar Fourier transformation in imaginary time. Since the one-particle Green's function is anti-periodic in τ with period β [8], we can again express it as:

$$G_1(\tau_1, \tau_2) = \frac{1}{\beta^2} \sum_{\nu_1}\sum_{\nu_2} \mathrm{e}^{-\mathrm{i}\nu_1\tau_1}\mathrm{e}^{\mathrm{i}\nu_2\tau_2} G_1^{\nu_1\nu_2}. \tag{2.7}$$

This time the Fourier coefficients $G_1^{\nu_1\nu_2}$ are defined on discrete frequencies $\nu_i = (2n_i + 1)\pi/\beta$ with $n_i \in \mathbb{Z}$. Note that bosonic functions are periodic in τ with the same period β [8] and therefore their coefficients are defined on different frequencies $\omega_i = 2n_i\pi/\beta$ with $n_i \in \mathbb{Z}$. These two sets of discrete frequencies are called fermionic and bosonic Matsubara frequencies, respectively.[1]

The Fourier coefficients in Matsubara space are given by

$$G_1^{\nu_1\nu_2} = \iint_0^\beta \mathrm{d}\tau_1\,\mathrm{d}\tau_2\,\mathrm{e}^{\mathrm{i}\nu_1\tau_1}\mathrm{e}^{-\mathrm{i}\nu_2\tau_2}G_1(\tau_1,\tau_2). \tag{2.8}$$

Using eq. (2.2), i.e., time translation invariance, we can again get rid of one parameter

$$\begin{aligned} G_1^{\nu_1\nu_2} &= \iint_0^\beta \mathrm{d}\tau_1\,\mathrm{d}\tau_2\,\mathrm{e}^{\mathrm{i}\nu_1\tau_1}\mathrm{e}^{-\mathrm{i}\nu_2\tau_2}G_1(\tau=\tau_1-\tau_2) \\ &= \int_0^\beta \mathrm{d}\tau_2\,\mathrm{e}^{-\mathrm{i}(\nu_2-\nu_1)\tau_2}\int_{-\tau_2}^{\beta-\tau_2}\mathrm{d}\tau\mathrm{e}^{\mathrm{i}\nu_1\tau}G_1(\tau) \\ &= \int_0^\beta \mathrm{d}\tau_2\,\mathrm{e}^{-\mathrm{i}(\nu_2-\nu_1)\tau_2}\int_0^\beta\mathrm{d}\tau\mathrm{e}^{\mathrm{i}\nu_1\tau}G_1(\tau) \\ &=: \beta\delta^{\nu_1\nu_2}G_1^{\nu_1}, \end{aligned} \tag{2.9}$$

and define the single-frequency one-particle Green's function G_1^ν. Note that from line two to line three, we can shift both integration boundaries of the τ integral by the same amount τ_2, because the integrand is β periodic, and we integrate over a full period.

Looking at the two Fourier series for time and space we see that the prefactors for the transformations differ. This choice is made deliberately based on considerations about units. For a single-band, spin-symmetric system with space translation invariance in the noninteracting limit, the Hamiltonian is diagonal in momentum space, and the one-particle Green's function can trivially be calculated to be

$$G_{1,0}^\nu(\mathbf{k}) = \frac{1}{\mathrm{i}\nu - \epsilon(\mathbf{k}) + \mu}, \tag{2.10}$$

where $\epsilon(\mathbf{k})$ is the dispersion relation and μ the chemical potential. The dimension of the Green's function in this case is inverse energy (frequency) or time. In imaginary time and real space it is, however, 1. We can see this when realizing that the expectation value $\langle \mathrm{T}\,\hat{c}_i^\dagger(\tau)\hat{c}_i(\tau)\rangle$ is the occupation n_i at site i which is just a number. Therefore, the creation and annihilation operators in τ and real space as well as all expectation values built thereof are dimensionless. Our choice of prefactors do not change the dimensions when going between real and reciprocal space because in eq. (2.6) the dimension of $\mathrm{d}\mathbf{k}$ cancels with that of V_{BZ}. In eqs. (2.8) and (2.9), however, we see that that is not the case

[1] Unless stated otherwise we will denote fermionic Matsubara frequencies with ν's and bosonic ones with ω's in this thesis.

for $\mathrm{d}\tau$ and therefore, we get one dimension of time for each frequency, which matches with eq. (2.10). The following gives a dimensional summary:

$$[\langle \mathrm{T}\, \hat{c}_i^\dagger(\tau)\hat{c}_i(\tau)\rangle] = [n_i] = 1, \tag{2.11}$$

$$[G_1^{\mathbf{R}_1\mathbf{R}_2}(\tau_1,\tau_2)] = [G_1^{\mathbf{R}}(\tau)] = 1, \tag{2.12}$$

$$[G_1^{\mathbf{R}}] = [G_1(\mathbf{k})] = 1, \tag{2.13}$$

$$[G_1^{\nu_1\nu_2}] = [\,\mathrm{d}\tau_1\,\mathrm{d}\tau_2] = [\tau]^2, \tag{2.14}$$

$$[G_1^{\nu}] = [G_{1,0}^{\nu}] = [\tau], \tag{2.15}$$

where $[\cdot]$ denotes the dimension of the quantity.

After all those rather technical details let us mention that the one-particle Green's function is also connected to an experimental observable, the so-called spectral function $A(\omega,\mathbf{k})$, observable in photoemission measurements. It is given by

$$A(\omega,\mathbf{k}) = -\frac{1}{\pi}G_1(\omega,\mathbf{k}), \tag{2.16}$$

where it is important to note that ω is a real frequency, which can be obtained from the Matsubara frequency by analytic continuation, i.e., $\mathrm{i}\nu \to \omega + \mathrm{i}0^+$.

As a final note, from now on we usually drop the index 1. If the particle-ness cannot be inferred from the (number of) arguments, (e.g., if we only write G) we always mean the one-particle Green's function.

2.2. Feynman diagrams

Feynman diagrams are an important tool in the field of QFT and used extensively in this thesis. Therefore, we give a short repetition of where they come from and what they are.

It all starts with the problem of calculating expectation values for interacting systems. Assume we can split the Hamiltonian describing such a system into a noninteracting part $\hat{H}_0$ and an interacting one $\hat{H}_{\mathrm{int}}$. In this thesis we only consider Hamiltonians that only have a four-point interaction, i.e., their interacting part is of the following form:

$$\hat{H}_{\mathrm{int}} = \frac{1}{2}\sum_{1234} U_{1234}\hat{c}_1^\dagger\hat{c}_3^\dagger\hat{c}_2\hat{c}_4, \tag{2.17}$$

where U is the Coulomb interaction, and all quantum numbers and other parameters are condensed into indices 1 to 4. Our goal is now to find a perturbative solution for the interacting problem around the noninteracting limit. For this we use the interaction picture which is convenient because there the time-evolution of an operator only uses $\hat{H}_0$:

$$\hat{A}_{\mathrm{I}}(\tau) = \mathrm{e}^{\hat{H}_0\tau}\hat{A}\mathrm{e}^{-\hat{H}_0\tau}. \tag{2.18}$$

Since the expectation value $\langle \hat{A} \rangle$ must be the same in all pictures, the time-evolution operator, or S-matrix, $\hat{S}(\tau)$ in the interaction picture is given by

$$\hat{S}(\tau) = \mathrm{e}^{\hat{H}_0 \tau} \mathrm{e}^{-\hat{H}\tau}. \tag{2.19}$$

The solution to its equation of motion

$$\frac{\partial \hat{S}(\tau)}{\partial \tau} = \mathrm{e}^{\hat{H}_0 \tau}(\hat{H}_0 - \hat{H})\mathrm{e}^{-\hat{H}\tau} = -\hat{H}_{\mathrm{int}} \hat{S}(\tau), \tag{2.20}$$

is the time-ordered exponential of the interaction Hamiltonian

$$\hat{S}(\tau) = \mathrm{T}\, \mathrm{e}^{-\int_0^\tau \hat{H}_{\mathrm{int}}(\tau_1)\, \mathrm{d}\tau_1} \tag{2.21}$$

which can be written as the following series

$$\hat{S}(\tau) = \sum_{n=0}^{\infty} \frac{(-1)^n}{n!} \int_0^\tau \mathrm{d}\tau_1 \ldots \int_0^\tau \mathrm{d}\tau_n\, \mathrm{T}\, \hat{H}_{\mathrm{int}}(\tau_1) \ldots \hat{H}_{\mathrm{int}}(\tau_n). \tag{2.22}$$

The reason for going through all of this is that we can rewrite the thermal expectation value of the full system as the one of the noninteracting one with an additional S-matrix:

$$\langle \mathrm{T} \ldots \rangle = \frac{\mathrm{Tr}\, \mathrm{e}^{-\beta \hat{H}}\, \mathrm{T} \ldots}{\mathrm{Tr}\, \mathrm{e}^{-\beta \hat{H}}} = \frac{\mathrm{Tr}\, \mathrm{e}^{-\beta \hat{H}_0}\, \mathrm{T}\, \hat{S}(\beta) \ldots}{\mathrm{Tr}\, \mathrm{e}^{-\beta \hat{H}_0} \hat{S}(\beta)} = \frac{\langle \mathrm{T} \ldots \hat{S}(\beta) \rangle_0}{\langle \hat{S}(\beta) \rangle_0}. \tag{2.23}$$

Here, $\langle \cdot \rangle_0$ denotes the expectation value with respect to the noninteracting Hamiltonian. Combining eqs. (2.22) and (2.23) we see that we can expand any correlation function in terms of the interaction Hamiltonian using only noninteracting expectation values. In the case of the one-particle Green's function this yields

$$G_{12}(\tau) = -\frac{1}{\langle \hat{S}(\beta) \rangle_0} \sum_{n=0}^{\infty} \frac{(-1)^n}{n!} \int_0^\tau \mathrm{d}\tau_1 \ldots \int_0^\tau \mathrm{d}\tau_n \langle \mathrm{T}\, \hat{c}_1(\tau) \hat{c}_2^\dagger \hat{H}_{\mathrm{int}}(\tau_1) \ldots \hat{H}_{\mathrm{int}}(\tau_n) \rangle_0. \tag{2.24}$$

Feynman diagrams are a graphical representation of the terms in this series. They are often easier to reason about than the normal representation since high-order terms quickly become unwieldy. Especially topological properties are easier to see in the diagrammatic form.

One such property is the connectedness. The linked-cluster theorem tells us that we only need to compute diagrams where all parts are connected or linked to one of the external points (1 and 2 in case of G_{12}) since the disconnected diagrams exactly cancel the denominator in eqs. (2.23) and (2.24) [9]. This is already a big simplification, but we still need one more step: Wick's theorem. It states that for noninteracting expectation values arbitrary products of creation and annihilation operators reduce to sums of pairwise contractions [10]. This means that we can write any term appearing in the expansion of a correlation function as a product of noninteracting or bare one-particle Green's

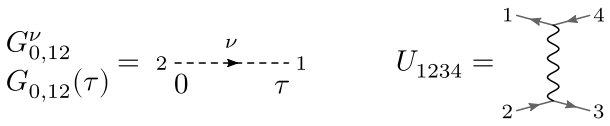

Figure 2.1.: Diagrammatic representation of the bare one-particle Greens function in imaginary times and Matsubara frequencies, and the bare interaction vertex. The gray lines of U_{1234} are not Green's functions, they just show how a potential Green's function would connect to the interaction line.

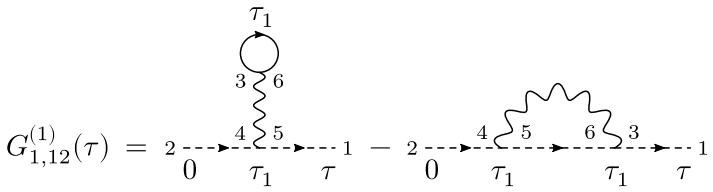

Figure 2.2.: Diagrammatic representation of eq. (2.25), the first-order terms in the expansion of the one-particle Green's function. The different signs between the diagrams and eq. (2.25) come from the minus sign in the definition of the one-particle Green's function [see eq. (2.1)].

functions $G_{0,12}$ and bare interaction vertices U_{1234}. As shown in fig. 2.1 we depict them with dashed and wiggly lines respectively.

As an example, let us compute the series expansion up to first order for the one-particle Green's function. The zeroth-order term is trivial and just contains the bare Green's function. For $n = 1$ we get a single interaction Hamiltonian in eq. (2.24), i.e., the sum over an interaction U as well as two creation and annihilation operators. Since one of the creation operators must be connected to the external annihilation operator and vice versa we end up with $2 \cdot 2 = 4$ terms. Two of them, however, are identical, which can be shown by relabeling the dummy indices $3456 \to 5634$, so we end up with

$$\begin{aligned} G^{(1)}_{1,12}(\tau) = \sum_{3456} \int_0^\beta \mathrm{d}\tau_1 U_{3456} \big[&- \langle \mathrm{T}\, \hat{c}_1(\tau) \hat{c}^\dagger_5(\tau_1) \rangle_0 \langle \mathrm{T}\, \hat{c}_6(\tau_1) \hat{c}^\dagger_3(\tau_1) \rangle_0 \langle \mathrm{T}\, \hat{c}_4(\tau_1) \hat{c}^\dagger_2 \rangle_0 \\ &+ \langle \mathrm{T}\, \hat{c}_1(\tau) \hat{c}^\dagger_3(\tau_1) \rangle_0 \langle \mathrm{T}\, \hat{c}_6(\tau_1) \hat{c}^\dagger_5(\tau_1) \rangle_0 \langle \mathrm{T}\, \hat{c}_4(\tau_1) \hat{c}^\dagger_2 \rangle_0 \big]. \end{aligned} \tag{2.25}$$

The corresponding Feynman diagrams are shown in fig. 2.2. With their help it is easier to see where the identical terms come from. If the interaction line in a diagram is plugged out, rotated by 180°, and plugged in again, we end up with the same diagram, just different internal labels that are summed over anyway. This means that for each interaction line in a diagram we get two identical terms in our series expansion. If we have more than one interaction line in a diagram we can also permute them without changing the topology of the diagram because the interaction lines are indistinguishable. Therefore, we get another $n!$ identical terms for each diagram of order n that we can draw.

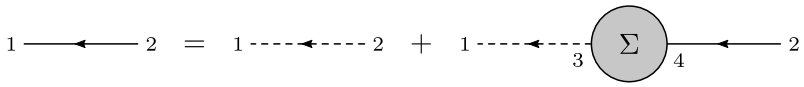

Figure 2.3.: Diagrammatic representation of eq. (2.26), the Dyson equation.

Putting all this together shows that it is sufficient to just draw topologically inequivalent diagrams and adjusting the prefactors accordingly. The factor 1/2 from eq. (2.17) is cancelled by the rotation trick and the factor $1/n!$ from the series expansion cancels with the permutations of the interaction lines. This means that the prefactor for all Feynman diagrams is ± 1, depending on the permutations required to get to a specific order of creation and annihilation operators and the $(-1)^n$ prefactor from the series expansion.

2.3. Self-energy

In his book *From here to infinity* [11], Ian Stewart introduces a dictionary that contains all possible combinations of the 26 letters of the alphabet: the Hyperwebster. It is split into 26 volumes each one containing all words starting with the same letter, so Volume A, e.g., lists the words A, AA, AAA, ..., AB, ABA, ABAA, ..., AZZZZ.... The publisher then drops the first letter of each word because it is already in the title of the volume. In doing so they not only save infinite amounts of ink but, due to the unintuitive nature of infinity, they also end up with a full copy of the whole Hyperwebster again.

We can do something similar with our infinite series of Feynman diagrams for the one-particle Green's function. For this we need the concept of one-particle reducibility. A diagram is said to be one-particle reducible (1PR), if it can be separated into two disconnected parts by cutting a single, Green's function line. If that is not possible, we call the diagram one-particle irreducible (1PI). Instead of dropping the first letter of each word we can now cut off the left-most 1PI part of every 1PR diagram in our expansion to generate the whole series again. This yields the Dyson equation [12]

$$G_{12} = G_{0,12} + \sum_{34} G_{0,13}\Sigma_{34}G_{42}, \tag{2.26}$$

where Σ_{34} is the 1PI one-particle vertex better known as the self-energy. It is shown diagrammatically in fig. 2.3. Bringing the implicit Dyson equation into an explicit form for the full Green's function

$$G^{-1} = G_0^{-1} - \Sigma, \tag{2.27}$$

and using eq. (2.10), we get

$$G^{\nu}(\mathbf{k}) = \frac{1}{\mathrm{i}\nu - \epsilon(\mathbf{k}) + \mu - \Sigma^{\nu}(\mathbf{k})} \tag{2.28}$$

for a spin-symmetric, single-band system.

Shifting our problem from the one-particle Green's function to the self-energy does not seem like much of an improvement. In dynamical mean-field theory (DMFT), however, which is discussed in more detail in section 3.3, the self-energy plays an important role.

2.4. Two-particle Green's function

The two-particle Green's function G_2 is defined as

$$G_{2,1234}(\tau_1,\tau_2,\tau_3,\tau_4) := (-1)^2\langle \mathrm{T}\,\hat{c}_1(\tau_1)\hat{c}_2^\dagger(\tau_2)\hat{c}_3(\tau_3)\hat{c}_4^\dagger(\tau_4)\rangle, \tag{2.29}$$

where we, again, use compound indices 1 to 4 for all remaining parameters and quantum numbers. Time and space translation invariance as well as Fourier transformations all work analogously to the one-particle case, so we only explicitly show the transformation to Matsubara space:

$$\begin{aligned} G_{2,1234}^{\nu_1\nu_2\nu_3\nu_4} &= \iiiint_0^\beta \mathrm{d}\tau_1\,\mathrm{d}\tau_2\,\mathrm{d}\tau_3\,\mathrm{d}\tau_4\, G_{2,1234}(\tau_1,\tau_2,\tau_3,\tau_4)\mathrm{e}^{\mathrm{i}(\nu_1\tau_1-\nu_2\tau_2+\nu_3\tau_3-\nu_4\tau_4)} \\ &= \beta\delta^{\nu_1-\nu_2+\nu_3-\nu_4,0}\iiint_0^\beta \mathrm{d}\tau_1'\,\mathrm{d}\tau_2'\,\mathrm{d}\tau_3'\, G_{2,1234}(\tau_1',\tau_2',\tau_3')\mathrm{e}^{\mathrm{i}(\nu_1\tau_1'-\nu_2\tau_2'+\nu_3\tau_3')} \\ &=: \beta\delta^{\nu_1-\nu_2+\nu_3-\nu_4,0}G_{2,1234}^{\nu_1\nu_2\nu_3}. \end{aligned} \tag{2.30}$$

With this we can infer the dimension of the two-particle Green's function in imaginary time and Matsubara space:

$$[G(\tau_1,\tau_2,\tau_3,\tau_4)] = [G(\tau_1,\tau_2,\tau_3,\tau_4)] = 1, \tag{2.31}$$

$$[G^{\nu_1\nu_2\nu_3\nu_4}] = [\tau]^4, \tag{2.32}$$

$$[G^{\nu_1\nu_2\nu_3}] = [\tau]^3. \tag{2.33}$$

Since we have more than one frequency argument even after using time-translation invariance, there are different frequency notations. Usually they are divided into three so-called channels: the particle–hole (ph), transversal particle–hole ($\overline{\text{ph}}$), and particle–particle (pp) channel. One possible choice for a consistent set of frequency notations in those three channels is defined in table 2.1 and shown diagrammatically in fig. 2.4. It is, however, not the only choice since we can shift all frequencies by the same amount without violating energy conservation (we differ, e.g., from the notation used in ref. [8]).

If momenta are involved nothing really changes. They can easily be incorporated by replacing the frequency indices with four-indices combining frequency and momentum: $\nu \to k = (\nu, \mathbf{k})$ and $\omega \to q = (\omega, \mathbf{q})$.

Of course the different notations are all equivalent in the sense that they don't change the physical content of G_2, but for some equations it is more convenient to choose one notation over the other. We will see an example of that in section 2.6.

Table 2.1.: A consistent set of frequency notations for the ph, pp, and $\overline{\text{ph}}$ channel. See fig. 2.4 for a diagrammatic representation.

Channel	ν_1	ν_2	ν_3	ν_4
ph	ν	$\nu - \omega$	$\nu' - \omega$	ν'
pp	ν	$\omega - \nu'$	$\omega - \nu$	ν'
$\overline{\text{ph}}$	ν	ν'	$\nu' - \omega$	$\nu - \omega$

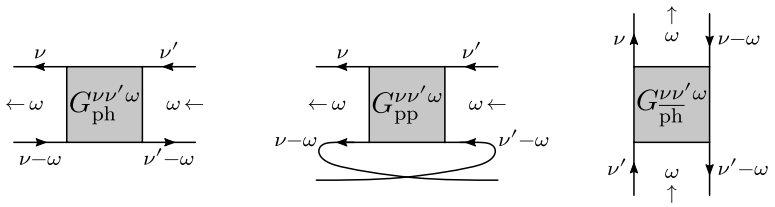

Figure 2.4.: Feynman diagrams of the two-particle Green's function in the three frequency notations form table 2.1

After the frequency and momentum indices we now take a closer look at the spin of the two-particle Green's function. All Hamiltonians considered in this thesis conserve spin. Therefore, most of the $2^4 = 16$ spin components of $G_{2,\sigma_1\sigma_2\sigma_3\sigma_4}$ vanish; only the following six do not:

$$\sigma_1 = \sigma_2 = \sigma_3 = \sigma_4, \qquad \sigma_1 = \sigma_2 \neq \sigma_3 = \sigma_4, \qquad \sigma_1 = \sigma_4 \neq \sigma_2 = \sigma_3. \tag{2.34}$$

This allows us to introduce a compact spin notation:

$$\begin{aligned} G_{2,\sigma\sigma'} &= G_{2,\sigma\sigma\sigma'\sigma'}, \\ G_{2,\overline{\sigma\sigma'}} &= G_{2,\sigma\sigma'\sigma'\sigma}. \end{aligned} \tag{2.35}$$

In the paramagnetic phase we can further simplify things by using SU(2) symmetry to get down to only three independent spin components: $G_{2,\uparrow\uparrow}$, $G_{2,\uparrow\downarrow}$, and $G_{2,\overline{\uparrow\downarrow}}$.

The last symmetry we consider is the crossing symmetry which directly stems from the Pauli principle. Looking at the definition of the two-particle Green's function in eq. (2.29), we see that exchanging the two creation or annihilation operators requires three permutations, so we get

$$\begin{aligned} G_{2,1234}(\tau_1, \tau_2, \tau_3, \tau_4) &= -G_{2,1432}(\tau_1, \tau_4, \tau_3, \tau_2) \\ &= -G_{2,3214}(\tau_3, \tau_2, \tau_1, \tau_4) \\ &= +G_{2,3412}(\tau_3, \tau_4, \tau_1, \tau_2). \end{aligned} \tag{2.36}$$

In Feynman diagrams this means that swapping the two in- or outgoing legs of the two-particle Green's function only introduces a minus sign.

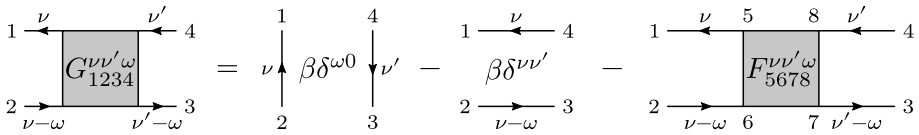

Figure 2.5.: Decomposition of the two-particle Green's function into two disconnected terms and a connected term, introducing the full two-particle vertex F

From now on we drop the index 2 whenever the two-particle-ness can be inferred from the (number of) arguments. Also, if not stated otherwise we use ph notation.

2.5. Full two-particle vertex

When we perform a series expansion of the two-particle Green's function, as introduced in section 2.2, we realize that a lot of terms contain parts that are identical to the expansion of the one-particle Green's function. We can resum those terms which effectively means that from now on we draw Feynman diagrams with solid lines for full, interacting, one-particle Green's functions G instead of dashed lines for bare ones G_0. To avoid double counting, our diagrams must not contain one-particle insertions, i.e., parts that can be separated from the rest of the diagram by cutting two Green's function lines, because they already appear in the expansion of G. We call such diagrams, only drawn with full Green's functions, skeleton diagrams.

Furthermore, most terms have interaction lines connecting the two in- and outgoing particles. We can collect them into a single interaction vertex which we call the full two-particle vertex F_2.[2] With this the whole series expansion of the two-particle Green's function can be drawn with just three diagrams. This decomposition of G_2 is shown in fig. 2.5. The corresponding equation reads

$$G^{\nu\nu'\omega}_{1234} = \beta\delta^{\omega 0} G^{\nu}_{12} G^{\nu'}_{34} - \beta\delta^{\nu\nu'} G^{\nu}_{14} G^{\nu-\omega}_{32} - G^{\nu}_{15} G^{\nu-\omega}_{62} F^{\nu\nu'\omega}_{5678} G^{\nu'}_{37} G^{\nu'-\omega}_{84}, \tag{2.37}$$

We call the first two terms disconnected but not in the same sense as when talking about the linked-cluster theorem.[3] There a disconnected diagram was one where part of it is not connected to any external line. From now on, however, we call diagrams connected or disconnected depending on whether all external points are connected with each other or not.

The sign of the vertex in eq. (2.37) is just convention. Our choice leads to the following weak coupling terms of F for the single-band Hubbard model (HM):

$$\lim_{U\to 0^+} F_{\uparrow\downarrow} = \lim_{U\to 0^+} +U, \qquad \lim_{U\to 0^+} F_{\overline{\uparrow\downarrow}} = \lim_{U\to 0^+} -U. \tag{2.38}$$

[2] Again, we usually drop the particle-ness index if it can be inferred from the (number of) arguments.
[3] In the language of the linked cluster theorem all these diagrams are connected (to at least one external point).

From eq. (2.37) we can also deduce the dimension of the full vertex to be

$$[F^{\nu\nu'\omega}] = [\tau]^{-1}. \tag{2.39}$$

This matches our expectations since the bare interaction U also has the dimension of energy or inverse time.

2.6. Irreducible two-particle vertices

Similarly to section 2.3 we can classify two-particle diagrams in terms of their reducibility. Since we only have a two-particle interaction term we can only go from two to two particles, or from three to one and vice versa. It is not possible to go from two particles to one so all two-particle diagrams are inherently 1PI.

On the two-particle level, of course, we also need to think about two-particle reducibility. This means that we check if diagrams can be separated into two disconnected parts by cutting two Green's function lines or not. In principle this is a binary property as well, but we can refine it and also care about which pairs of external points stay connected or, alternatively, which pairs of Green's functions have to be cut: a particle–hole pair that runs horizontally, a particle–hole pair that runs vertically, or a particle–particle pair. These are the three channels (ph, $\overline{\text{ph}}$, pp) we already mentioned in section 2.4 when introducing the different frequency notations. While the latter are just different notations for the same object, there is of course a real difference if a diagram is reducible in one channel or another. As it turns out every two-particle diagram is at most reducible in one of the three channels [13–15]. This allows us to uniquely split up the full two-particle vertex F into four terms

$$F_{1234} = \Lambda_{1234} + \Phi_{\text{ph},1234} + \Phi_{\overline{\text{ph}},1234} + \Phi_{\text{pp},1234}, \tag{2.40}$$

where Λ is the fully irreducible two-particle vertex, and the reducible diagrams are collected in Φ_{ph}, $\Phi_{\overline{\text{ph}}}$, and Φ_{pp}. Equation (2.40) is called parquet equation or parquet decomposition. Its diagrammatic representation is shown in fig. 2.6, where scissors mark the lines that can be cut to separate a diagram.

Let us now briefly talk about the crossing symmetry of the different terms in eqs. (2.37) and (2.40). Since the full two-particle Green's function is crossing symmetric and the two disconnected terms in eq. (2.37) each maps to the other one under crossing, the full two-particle vertex is crossing symmetric as well. Things are similar for the components of the parquet decomposition in eq. (2.40). When swapping the two in- or outgoing legs, the ph channel turns into the $\overline{\text{ph}}$ channel and vice versa. The fully irreducible vertex Λ can never map to any reducible diagram no matter what one does with the external

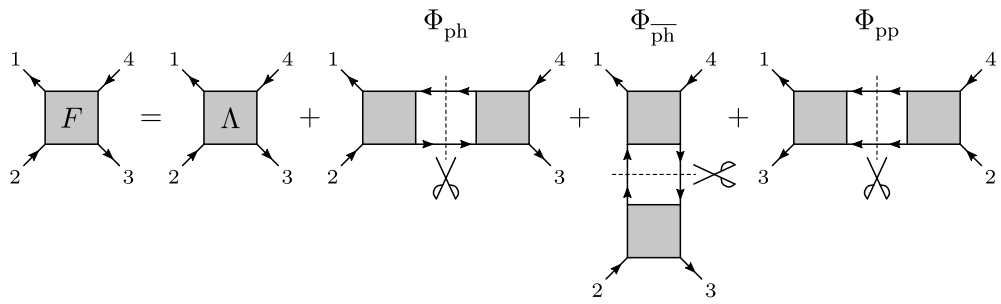

Figure 2.6.: Diagrammatic representation of the parquet equation [eq. (2.40)]. Scissors mark the Green's function lines that can be cut to separate a diagram. Note that in the diagram for the pp channel, the legs of the two-particle vertices are drawn in a different order: the in- and outgoing legs are on the same side of the square instead of diagonally across.

legs, and Φ_{pp} cannot map to Λ for the same reason. Therefore, these two components are crossing symmetric on their own. Putting everything together we have

$$\begin{aligned} F_{1234} &= -F_{3214} = -F_{1432}, \\ \Lambda_{1234} &= -\Lambda_{3214} = -\Lambda_{1432}, \\ \Phi_{\mathrm{ph},1234} &= -\Phi_{\overline{\mathrm{ph}},3214} = -\Phi_{\overline{\mathrm{ph}},1432}, \\ \Phi_{\overline{\mathrm{ph}},1234} &= -\Phi_{\mathrm{ph},3214} = -\Phi_{\mathrm{ph},1432}, \\ \Phi_{\mathrm{pp},1234} &= -\Phi_{\mathrm{pp},3214} = -\Phi_{\mathrm{pp},1432}. \end{aligned} \tag{2.41}$$

Equation (2.40) is not the only useful decomposition of the full two-particle vertex F, regarding reducibility. Instead of working with the fully irreducible vertex Λ we can look at one channel at a time and define vertices Γ that are only irreducible in a single one:

$$\Gamma_r = F - \Phi_r, \quad r \in \{\mathrm{ph}, \overline{\mathrm{ph}}, \mathrm{pp}\}. \tag{2.42}$$

With this we are back to a binary property for each channel r and in a situation similar to section 2.3. From every reducible diagram in Φ_r we can cut off the left-most irreducible part and again be left with the whole series of diagrams for the full vertex F. If we do the math properly, we get the so-called Bethe–Salpeter equations [16]

$$\begin{aligned} F_{1234} &= \Gamma_{\mathrm{ph},1234} + \sum_{5678} \Gamma_{\mathrm{ph},1256} G_{67} G_{85} F_{7834}, \\ F_{1234} &= \Gamma_{\overline{\mathrm{ph}},1234} - \sum_{5678} \Gamma_{\overline{\mathrm{ph}},1654} G_{67} G_{85} F_{7238}, \\ F_{1234} &= \Gamma_{\mathrm{pp},1234} + \frac{1}{2} \sum_{5678} \Gamma_{\mathrm{pp},1836} G_{67} G_{85} F_{7254}, \end{aligned} \tag{2.43}$$

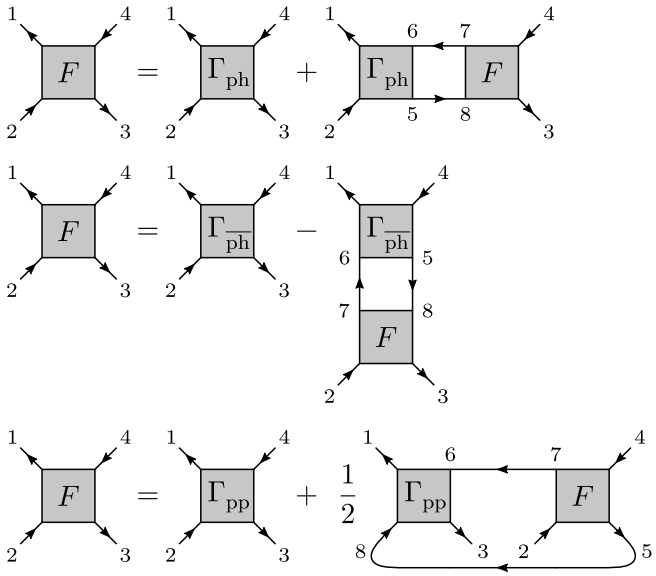

Figure 2.7.: Diagrammatic representation of eq. (2.43), the Bethe–Salpeter equations. Contrary to fig. 2.6 we use the normal order of legs also for the pp vertices. This makes it is easier to understand the indices in eq. (2.43).

where the different signs between the ph and $\overline{\text{ph}}$ channels respect the crossing relations in eq. (2.41) and the factor 1/2 in the pp channel comes from the indistinguishability of the particles [15].[4] Figure 2.7 shows the corresponding Feynman diagrams.

Even though we suppressed the frequency and momentum indices it is worth noting that the Bethe–Salpeter equations are diagonal in the bosonic transfer four-index $q = (\omega, \mathbf{q})$ if the frequency notation matches the reducibility channel. This is convenient for numerical implementations as it allows us to treat the vertices at different q as independent matrices in the indices k and k'. The explicit form of the equations like, e.g.,

$$F^q_{\text{ph},1234} = \frac{\Gamma^q_{\text{ph},1234}}{1 - (\Gamma_{1256} G_{64} G_{35})^q} \tag{2.44}$$

can therefore be solved via simple matrix inversion.

2.7. Schwinger–Dyson equations

The last important equations that we need to mention in the Green's function formalism are the Schwinger–Dyson equations. They are the equations of motion of the Green's

[4] We find that this standard argument is rather unsatisfactory. For a detailed explanation of why the factor of 1/2 is necessary see the discussion after eq. (6.15) in section 6.2.

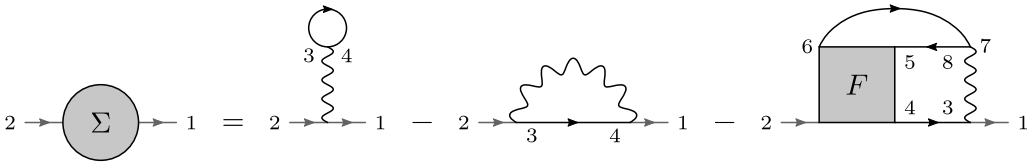

Figure 2.8.: Diagrammatic representation of eq. (2.45), the lowest-order Schwinger–Dyson equation rewritten in terms of the self-energy Σ.

functions [17] and form an infinite stack of coupled equations. More specifically, the equation for the n-particle Green's function depends on $(n+1)$-particle quantities. Still the lowest-order one is very useful and important for many diagrammatic approaches. It is often referred to as just *the* Schwinger–Dyson equation and can be rewritten to connect the full two-particle vertex F to the self-energy Σ [18]. For Hubbard-like Hamiltonians it reads [19]

$$\Sigma_{12} = \sum_{34} U_{3214} n_{34} - \sum_{34} U_{1234} n_{34} - \sum_{345678} F_{6245} U_{8317} G_{76} G_{58} G_{34}, \tag{2.45}$$

where the first two terms are the Hartree and Fock contribution to the self-energy, respectively. A diagrammatic representation of the whole equation is shown in fig. 2.8.

2.8. Nonlinear response theory

Response theory is a well studied and important part of physics because the concept of quantifying how a system reacts in response to some perturbation is very general and widely applicable. Since the famous work published by Kubo in 1957 [20] we also have a theoretical description for computing such responses in a quantum mechanical system. Often times people only consider the lowest-order terms, i.e., linear response functions. Their derivation is covered in standard text books like Altland and Simons [21]. In chapter 5, however, we present nonlinear, specifically second-order, response theory as an application for three-particle correlations. Therefore, in this section we basically follow the derivation in Altland and Simons [21] but keep higher-order terms.

Let us assume that our unperturbed system, described by a Hamiltonian $\hat{H}$, couples to external fields $F_j(\tau) \in \mathbb{R}$, with imaginary time τ, and hermitian operators $\hat{A}_j = \hat{A}_j^\dagger$ as

$$\hat{\mathcal{H}}(\tau) = \hat{H} - \sum_j \hat{A}_j F_j(\tau). \tag{2.46}$$

The action for this system is then given by

$$\mathcal{S}[c^+, c, \mathbf{F}] = S[c^+, c] - \sum_{jaa'} \int_0^\beta \mathrm{d}\tau F_j(\tau) c_a^+(\tau) A_j^{aa'} c_{a'}(\tau), \tag{2.47}$$

where c and c^+ are Grassmann-valued fields corresponding to the eigenvalues of $\hat{c}(\tau)$ and $\hat{c}^\dagger(\tau)$ with respect to coherent states, and $A_j^{aa'}$ are the matrix elements of $\hat{A}_j$, i.e., $\hat{A}_j = \sum_{aa'} \hat{c}_a^\dagger A_j^{aa'} \hat{c}_{a'}$. Note that this derivation does not require $\hat{A}$ to be a one-particle operator, even though that is the case for all operators that we are interested in. It works just as well with any hermitian n-particle operator.

Now we compute the expectation value $\langle \hat{A}_i(\tau) \rangle_{\mathbf{F}}$ in the path integral formalism, where

$$\langle ... \rangle_{\mathbf{F}} = \mathcal{Z}^{-1} \int \mathcal{D}c^+ \, \mathcal{D}c \mathrm{e}^{-\mathcal{S}[c^+,c,\mathbf{F}]} \, ... \,, \tag{2.48}$$

$$\mathcal{Z} = \int \mathcal{D}c^+ \, \mathcal{D}c \mathrm{e}^{-\mathcal{S}[c^+,c,\mathbf{F}]}, \tag{2.49}$$

$$\langle \hat{A}_i(\tau) \rangle_{\mathbf{F}} = \frac{\delta}{\delta F_i(\tau)} \ln \mathcal{Z}, \tag{2.50}$$

and expand it in a functional Taylor series around $\mathbf{F} = 0$,

$$\langle \hat{A}_i(\tau) \rangle_{\mathbf{F}} = \sum_n \frac{1}{n!} \int \cdots \int_0^\beta \mathrm{d}\tau_1 \ldots \mathrm{d}\tau_n \sum_{j_1,\ldots,j_n} \times F_{j_1}(\tau_1) \ldots F_{j_n}(\tau_n) \left(\frac{\delta^n}{\delta F_{j_1}(\tau_1) \ldots \delta F_{j_n}(\tau_n)} \langle \hat{A}_i(\tau) \rangle \right)_{\mathbf{F}=0}. \tag{2.51}$$

This allows us to identify the response functions $\chi^{(n)}$ as the functional derivatives of the expectation value of the operator $\hat{A}_i$ with respect to the external fields F_j:

$$\chi^{(n)}_{j_1 \ldots j_n i}(\tau_1, \ldots, \tau_n, \tau) = \left(\frac{\delta^n}{\delta F_{j_1}(\tau_1) \ldots \delta F_{j_n}(\tau_n)} \langle \hat{A}_i(\tau) \rangle_{\mathbf{F}} \right)_{\mathbf{F}=0}. \tag{2.52}$$

As usual the derivatives can be exchanged because the action is just a polynomial of the operators and fields.

Doing the actual differentiation we get for the first-order term, i.e., the linear response function,

$$\begin{aligned} \chi^{(1)}_{ij}(\tau, \tau') &= \left(\frac{\delta^2}{\delta F_i(\tau) \delta F_j(\tau')} \ln \mathcal{Z} \right)_{\mathbf{F}=0} \\ &= -\mathcal{Z}^{-2} \left(\frac{\delta}{\delta F_i(\tau)} \mathcal{Z} \right)_{\mathbf{F}=0} \left(\frac{\delta}{\delta F_j(\tau')} \mathcal{Z} \right)_{\mathbf{F}=0} \\ &\quad + \mathcal{Z}^{-1} \left(\frac{\delta^2}{\delta F_i(\tau) \delta F_j(\tau')} \mathcal{Z} \right)_{\mathbf{F}=0} \\ &= -\langle \hat{A}_i \rangle \langle \hat{A}_j \rangle + \langle \mathrm{T} \, \hat{A}_i(\tau) \hat{A}_j(\tau') \rangle. \end{aligned} \tag{2.53}$$

The second-order response function reads

$$\begin{aligned}
\chi^{(2)}_{ijk}(\tau_1,\tau_2,\tau_3) &= \left(\frac{\delta^3}{\delta F_i(\tau_1)\,\delta F_j(\tau_2)\,\delta F_k(\tau_3)}\ln\mathcal{Z}\right)_{\mathbf{F}=0} \\
&= 2\mathcal{Z}^{-3}\left(\frac{\delta}{\delta F_i(\tau_1)}\mathcal{Z}\right)_{\mathbf{F}=0}\left(\frac{\delta}{\delta F_j(\tau_2)}\mathcal{Z}\right)_{\mathbf{F}=0}\left(\frac{\delta}{\delta F_k(\tau_3)}\mathcal{Z}\right)_{\mathbf{F}=0} \\
&\quad - \mathcal{Z}^{-2}\left(\frac{\delta}{\delta F_i(\tau_1)}\mathcal{Z}\right)_{\mathbf{F}=0}\left(\frac{\delta^2}{\delta F_j(\tau_2)\,\delta F_k(\tau_3)}\mathcal{Z}\right)_{\mathbf{F}=0} \\
&\quad - \mathcal{Z}^{-2}\left(\frac{\delta}{\delta F_j(\tau_2)}\mathcal{Z}\right)_{\mathbf{F}=0}\left(\frac{\delta^2}{\delta F_i(\tau_1)\,\delta F_k(\tau_3)}\mathcal{Z}\right)_{\mathbf{F}=0} \\
&\quad - \mathcal{Z}^{-2}\left(\frac{\delta}{\delta F_k(\tau_3)}\mathcal{Z}\right)_{\mathbf{F}=0}\left(\frac{\delta^2}{\delta F_i(\tau_1)\,\delta F_j(\tau_2)}\mathcal{Z}\right)_{\mathbf{F}=0} \\
&\quad + \mathcal{Z}^{-1}\left(\frac{\delta^3}{\delta F_i(\tau_1)\,\delta F_j(\tau_2)\,\delta F_k(\tau_3)}\mathcal{Z}\right)_{\mathbf{F}=0} \\
&= +2\langle\hat{A}_i\rangle\langle\hat{A}_j\rangle\langle\hat{A}_k\rangle \\
&\quad - \langle\hat{A}_i\rangle\langle\mathrm{T}\,\hat{A}_j(\tau_2)\hat{A}_k(\tau_3)\rangle \\
&\quad - \langle\hat{A}_j\rangle\langle\mathrm{T}\,\hat{A}_i(\tau_1)\hat{A}_k(\tau_3)\rangle \\
&\quad - \langle\hat{A}_k\rangle\langle\mathrm{T}\,\hat{A}_i(\tau_1)\hat{A}_j(\tau_2)\rangle \\
&\quad + \langle\mathrm{T}\,\hat{A}_i(\tau_1)\hat{A}_j(\tau_2)\hat{A}_k(\tau_3)\rangle.
\end{aligned} \tag{2.54}$$

Plugging in eq. (2.53) and reordering some terms finally yields

$$\begin{aligned}
\chi^{(2)}_{ijk}(\tau_1,\tau_2,\tau_3) &= \langle\mathrm{T}\,\hat{A}_i(\tau_1)\hat{A}_j(\tau_2)\hat{A}_k(\tau_3)\rangle \\
&\quad - \langle\hat{A}_i\rangle\chi_{jk}(\tau_2,\tau_3) - \langle\hat{A}_j\rangle\chi_{ik}(\tau_1,\tau_3) - \langle\hat{A}_k\rangle\chi_{ij}(\tau_1,\tau_2) \\
&\quad - \langle\hat{A}_i\rangle\langle\hat{A}_j\rangle\langle\hat{A}_k\rangle.
\end{aligned} \tag{2.55}$$

For the rest of this thesis we will drop the superscript indicating the order of the response function when it can be inferred from the (number of) arguments.

3. Models and methods

> It seems that perfection is attained not when there is nothing more to add, but when there is nothing more to remove.
>
> Antoine de Saint-Exupéry

After refreshing our theoretical background knowledge in the last chapter we can now introduce the models and briefly explain the methods used in the main part of the thesis to study three-particle correlations.

3.1. Anderson impurity model

The Anderson impurity model (AIM) was introduced in 1961 by P. W. Anderson to describe magnetic impurities in metals [22]. Since then, it has become a popular model in the field of correlated many-electron systems. Arguably, this is because even though its Hamiltonian, which is described below, is rather simple it already shows effects of strong correlation, more specifically the Kondo effect [23, 24]. Another important aspect is that its solution is connected to local correlation functions of more complex lattice Hamiltonians. We discuss this in more detail in section 3.3, when we talk about dynamical mean-field theory (DMFT). For an in-depth review of the physics of the AIM and the Kondo problem see refs. [25, 26].

The Hamiltonian of the AIM reads

$$\hat{H}_{\mathrm{AIM}} = \epsilon\hat{n} + U\hat{n}_\uparrow\hat{n}_\downarrow + \sum_{k,\sigma}\epsilon_k\hat{c}^\dagger_{k\sigma}\hat{c}_{k\sigma} + \sum_{k,\sigma}\left(V_k\hat{f}^\dagger_\sigma\hat{c}_{k\sigma} + V_k^*\hat{c}^\dagger_{k\sigma}\hat{f}_\sigma\right). \tag{3.1}$$

The first two terms describe the impurity with one-particle energy ϵ. Electrons on the impurity are created and annihilated with $\hat{f}^\dagger_\sigma$ and $\hat{f}_\sigma$, respectively. As usual the density operators are given by $\hat{n} = \hat{n}_\uparrow + \hat{n}_\downarrow$, with $\hat{n}_\sigma = \hat{f}^\dagger_\sigma\hat{f}_\sigma$. If the impurity is doubly occupied the local Coulomb interaction U comes into play. The third term models a bath of noninteracting electrons with dispersion relation ϵ_k, as well as creation and annihilation operators $\hat{c}^\dagger_{k\sigma}$ and $\hat{c}_{k\sigma}$. The last terms describe the hybridization from the bath to the impurity (V_k) and vice versa (V_k^*).

In this thesis we employ the AIM only with a real, k-independent hybridization $V_k \equiv V \in \mathbb{R}$ and with two different kinds of baths. We either use a discrete set of bath sites and energies, or a continuous bath with a constant density of states (DOS)

$$\rho(\epsilon) = \begin{cases} \rho_0, & -D \leq \epsilon \leq D \\ 0, & \text{otherwise} \end{cases} \tag{3.2}$$

where D is the half bandwidth.

3.2. Hubbard model

Named after J. Hubbard the Hubbard model (HM) actually goes back to not only his work from 1963 [27], but also to works from Kanamori [28] and Gutzwiller [29]. It is one of the fundamental models for strongly correlated electron systems. In its simple description electrons can move through a lattice only by hopping from one site to another. If a site is doubly occupied a local Coulomb comes into play. However, despite its simple nature, the HM can in general not be solved analytically. This is only possible in one dimension [30] and with DMFT in the limit of infinite dimensions or lattice coordination number (see section 3.3). Even after more than 50 years, the HM is not fully understood in the most interesting cases of two and three dimensions since numerical solutions are limited [31].

A general introduction to the HM and its physics can be found in textbooks like, e.g., ref. [26]. For a collection of important works see ref. [32]. The books of the Jülich "Modeling and Simulation" series often follow a more pedagogical but still comprehensive approach. The HM is studied, e.g., in the proceedings of the 2018 Jülich school [33].

In this thesis we only consider the simplest HM with a single band and nearest neighbor hopping on a square lattice. Its Hamiltonian then reads:

$$\hat{H}_{\mathrm{HM}} = -t \sum_{\langle ij \rangle, \sigma} \hat{c}^\dagger_{i\sigma} \hat{c}_{j\sigma} + U \sum_i \hat{n}_{i\uparrow} \hat{n}_{i\downarrow}. \tag{3.3}$$

The first term models the kinetic energy, where t is the hopping energy between neighboring sites, $\hat{c}^\dagger_{i\sigma}/cq_{i\sigma}$ creates/annihilates an electron with spin σ on lattice site i, and $\langle ij \rangle$ denotes the sum over nearest neighbors. The second term describes the on-site Coulomb interaction U with the local density operator for spin σ given by $\hat{n}_{i\sigma} = \hat{c}^\dagger_{i\sigma} \hat{c}_{i\sigma}$.

3.3. Dynamical mean-field theory

Over the past three decades dynamical mean-field theory (DMFT) has become one of the most popular and widely used methods for studying systems with strong electronic correlation [34]. Its development started in 1989 when Metzner and Vollhardt showed

that the self-energy in infinite dimensions is purely local [35]. Three years later in 1992, Georges and Kotliar found the connection between the HM in infinite dimensions and the AIM, writing down the equations for the DMFT self-consistency loop for the first time [36]. In the following we briefly recapitulate the core approximation of DMFT and the self-consistency equations. For more in-depth information see the review by Georges et al. [37], the Jülich summer school book series, e.g., [38], or the review by Held [39].

In section 2.3, more specifically eq. (2.28), we already saw that the self-energy is basically a frequency- and momentum-dependent correction for the full, interacting one-particle Green's function. The core approximation of DMFT is to drop the momentum dependence,

$$\Sigma^{\nu}_{\mathrm{DMFT},12}(\mathbf{k}) = \Sigma^{\nu}_{12}, \tag{3.4}$$

and assume that the self-energy is purely local, i.e., all its diagrams end at the same lattice site i that they started

$$\Sigma^{\nu}_{\mathrm{DMFT},ij,12} = \delta_{ij}\Sigma^{\nu}_{12}. \tag{3.5}$$

Metzner and Vollhardt first showed that this approximation becomes exact in the limit of infinite dimensions or lattice connectivity. What follows is only a brief sketch of the proof. For more details and an in-depth discussion we, again, refer the reader to refs. [37–39].

On a lattice the formal limit of infinite dimensions means that $Z_{\|\mathbf{R}_i-\mathbf{R}_j\|}$ the number of lattice sites at distance $\|\mathbf{R}_i - \mathbf{R}_j\|$ approaches infinity. If we consider the Hamiltonian of the HM defined in the previous section we see that the interaction term is local and therefore does not scale with Z. For the kinetic energy on the other hand we get

$$E_{\mathrm{kin}} = -2\sum_{i\neq j} t_{ij}\langle \hat{c}_i^{\dagger}\hat{c}_j\rangle = -2\sum_{R=\|\mathbf{R}_i-\mathbf{R}_j\|} Z_R t_R G_R(\tau = 0^-). \tag{3.6}$$

To prevent it from diverging in the limit $Z \to \infty$ the hopping amplitudes t_{ij} must be rescaled. Since one-particle Green's function is connected to the hopping [see eq. (2.28)] it scales the same way [39]. Therefore, the only possible rescaling is

$$t^*_{ij} = \frac{t_{ij}}{\sqrt{Z_{\|\mathbf{R}_i-\mathbf{R}_j\|}}}. \tag{3.7}$$

Let us now consider how in self-energy diagrams interaction vertices at different sites are connected. Since the self-energy is one-particle irreducible (1PI) they cannot just be connected by a single Green's function line. If we draw the diagrams with full Green's functions, i.e., as skeleton diagrams, they must also not be connected by just two lines, since that would then be a one-particle insertion. Therefore, each interaction vertex is connected by at least three paths [40] and scales at best with $O(Z^{-\frac{3}{2}}_{\|\mathbf{R}_i-\mathbf{R}_j\|})$. Since the sum over different equivalent neighbors scales with $O(Z_{\|\mathbf{R}_i-\mathbf{R}_j\|})$ all nonlocal contributions to

the self-energy are suppressed by $O(Z^{-\frac{1}{2}}_{\|\mathbf{R}_i-\mathbf{R}_j\|})$. The self-energy thus becomes local in infinite dimensions and DMFT becomes exact.

The observant reader surely notices that we are far from living in infinite dimensions. Fortunately it seems that already in three dimensions, DMFT is a good approximation. See, e.g., ref. [41].

DMFT is not just the local self-energy approximation, though. Even if that already simplifies things greatly, we still need to compute an infinite series of local diagrams, and in general we cannot do that analytically. Georges and Kotliar showed, however, that the problem can be mapped onto an impurity problem. Specifically, the diagrams of the local self-energy of the HM are the same as those for the AIM with an equal local interaction. This solves the problem because there are several numerical impurity solvers.

DMFT is usually implemented as the following self-consistent cycle, where we make frequent use of the Dyson equation in different forms (see eqs. (2.26) to (2.28)).

1. Start with an initial guess for the local self-energy Σ^ν_{12} – in the simplest case just zero.

2. Use the self-energy to compute the local lattice Green's function

$$G^\nu_{12} = \frac{1}{V_{\mathrm{BZ}}}\int_{\mathrm{BZ}} \mathrm{d}\mathbf{k}(\mathrm{i}\nu - \epsilon(\mathbf{k}) + \mu - \Sigma^\nu)^{-1}_{12} = \int \mathrm{d}\epsilon\rho(\epsilon)(\mathrm{i}\nu - \epsilon + \mu - \Sigma^\nu)^{-1}_{12}, \quad (3.8)$$

   where V_{BZ} is the volume of the first Brillouin zone and $\rho(\epsilon)$ is the noninteracting density of states.

3. Since the interacting impurity Green's function $\mathcal{G}^\nu_{12}$ is the same as the local, interacting lattice Green's function G^ν_{12}, compute the noninteracting impurity Green's function as

$$\mathcal{G}^\nu_{0,12} = \left(G^\nu + \Sigma^\nu\right)^{-1}_{12}. \quad (3.9)$$

   This effectively defines the AIM.

4. Use an impurity solver to compute $\mathcal{G}^\nu$, the interacting Green's function of the AIM.

5. Compute a new self-energy by rewriting eq. (3.9):

$$\Sigma^\nu_{\mathrm{new},12} = \left((\mathcal{G}^\nu_0)^{-1} - \mathcal{G}^\nu\right)^{-1}_{12}. \quad (3.10)$$

6. Check if the self-energy is converged, i.e.,

$$\|\Sigma^\nu_{\mathrm{new},12} - \Sigma^\nu_{12}\| < \varepsilon \quad (3.11)$$

   with some norm $\|\cdot\|$, and convergence criterion ε. If not go back to 2 with the new self-energy.

The computationally expensive part of this cycle is calculating $\mathcal{G}^{\nu}$, the interacting Green's function of the AIM. Many solvers have been developed for this over the years using methods like exact diagonalization (ED) [42, 43], numerical renormalization group [44], or quantum Monte Carlo (QMC) [45]. In this thesis we will almost exclusively use continuous-time quantum Monte Carlo in the hybridization expansion (CT-HYB) [46].

3.4. Beyond DMFT: dynamical vertex approximation

DMFT is a very successful and popular tool in the field of strong electronic correlations. It captures, e.g., the Mott metal–insulator transition. However, due to the nature of its approximation it fails to correctly describe systems where nonlocal correlations are important and phenomena like the pseudogap, or d-wave superconductivity arise. See, e.g., ref. [47]. Methods beyond DMFT are required to capture the physics in these cases. For the most part they can be grouped into so-called cluster methods and diagrammatic extensions of DMFT.

As the name suggests cluster methods solve a small cluster of interacting sites that are embedded in a noninteracting bath. The clusters can either be constructed in real or momentum space. Due to the rather small size of the clusters they are best at describing short-range fluctuations, but have nonetheless successfully been applied to the HM for various parameters [48, 49].

Similar as for cluster expansions, there are several flavors of diagrammatic extensions of DMFT. For a comparison and an in-depth discussion see refs. [18, 50]. Many of them extend the idea of DMFT by approximating a two-particle vertex instead of the self-energy to be fully local. Which two-particle vertex is approximated depends on the exact method: For example, the dual fermion approach [51], and the one-particle irreducible approach [52] consider the full two-particle vertex F local, while the dynamical vertex approximation (DΓA) [53] builds upon the local, fully irreducible two-particle vertex Λ_{loc}. In the ladder version of DΓA the two-particle vertex irreducible in channel r, Γ_r, is approximated to be local. Similar ladder approaches are employed for dual fermions. The different methods also construct Feynman diagrams using different equations and different one-particle Green's functions. In this section we focus on full, i.e., not ladder DΓA, briefly recapitulating the necessary approximations and equations. For a more detailed, pedagogical introduction see ref. [38, ch. 10].

The central idea of DΓA is to resum Feynman diagrams in terms of their locality. DMFT already does this on the one-particle level where the 1PI one-particle vertex, the self-energy, is approximated to be local. DΓA extends this to the two-particle level and approximates the fully irreducible two-particle vertex Λ as purely local. Of course one does not need to stop there, but can go to even higher n-particle vertices. In the limit of $n \to \infty$ all possible Feynman diagrams are correctly resummed, and we obtain the exact solution [53].

Not only the approximation, also the equations used in DΓA are somewhat similar to those of DMFT. The latter mainly employs the Dyson equation [eq. (2.26)] to go between the full one-particle Green's function and the irreducible vertex. In DΓA this is replaced with the Bethe–Salpeter equations [eq. (2.43)], that connect the full two-particle vertex F with those reducible in a single channel Γ_r, as well as the parquet equation [eq. (2.40)], which contains the fully irreducible vertex Λ.

The starting point of a DΓA calculation is a converged DMFT solution. This means that we have already mapped our HM to an AIM with the same local interaction U, one-particle Green's function G^ν, and self-energy Σ^ν. This AIM can now also be used to obtain the local, fully irreducible vertex $\Lambda^{\nu\nu'\omega}$.[1] Usually, one actually computes the local two-particle Green's function, subtracts the disconnected terms to get the full local vertex $F^{\nu\nu'\omega}$ [see eq. (2.37)], and then by inverting the local Bethe–Salpeter and parquet equations obtains $\Lambda^{\nu\nu'\omega}$. The first real DΓA step is to use $\Lambda^{\nu\nu'\omega}$ and the nonlocal, i.e., $\mathbf{k}$-dependent DMFT Green's function G^k_{DMFT} in the parquet and Bethe–Salpeter equations to build a full, nonlocal vertex $F^{kk'q}$. This can then be plugged into the Schwinger–Dyson equation to obtain a nonlocal self-energy Σ^k, which in turn can be used to compute a new nonlocal one-particle Green's function G^k in an inner self-consistency. Again, similar to DMFT we can now construct a self-consistency cycle by using this new Green's function (at fixed $\Lambda^{\nu\nu'\omega}$) in the nonlocal Bethe–Salpeter and parquet equations to compute a new $F^{kk'q}$, etc. until convergence.

One could of course also expand the self-consistency cycle by using the new G^k to compute a new local Green's function G^ν and then use that to update the AIM, etc. in a further, outer self-consistency. However, many DΓA calculations do not even use the full parquet self-consistency cycle. Instead, they use so-called ladder DΓA, either self-consistently, see, e.g., ref. [54], or in a one-shot approach with a so-called λ correction, see, e.g., ref. [47]. Even in the original publication [53] the ladder version, where the vertices irreducible in the two particle–hole channels are approximated to be local, was used to study long-range antiferromagnetic fluctuations near a Mott metal–insulator transition.

[1] Here and in the following we distinguish between local and nonlocal quantities by using frequency indices ν, ω or four-momentum indices k, q, respectively.

4. Three-particle Green's function

Parts of this chapter marked with a vertical bar have already been published in Kappl et al. [55]. Minor modifications were made to better distinguish two-particle and three-particle frequency notations and to better match the notation in the rest of the thesis. Sections 4.3 and 4.4 are also based on material from Kappl et al. [55], but in this thesis it is presented in more detail.

The (local) three-particle Green's function and its systematic investigation are at the heart of the present thesis. This chapter lays the theoretical groundwork for that. It generalizes and expands ideas from the one- and two-particle level. However, just based on simple combinatorics it is expected that the three-particle level has a richer and more complex structure – which usually means one has to be more careful and compute more and longer equations. To prevent future physicists from repeating these sometimes tedious calculations this chapter aims at providing a comprehensive reference of definitions, notations, symmetries and other properties of the three-particle Green's function.

4.1. Definition

The three-particle Green's function is defined as

$$G_{3,1\ldots6}(\tau_1,\ldots,\tau_5) \coloneqq (-1)^3\langle \mathrm{T}\,\hat{c}_1(\tau_1)\hat{c}_2^\dagger(\tau_2)\hat{c}_3(\tau_3)\hat{c}_4^\dagger(\tau_4)\hat{c}_5(\tau_5)\hat{c}_6^\dagger(0)\rangle, \tag{4.1}$$

with imaginary times τ_i and all other parameters and quantum numbers condensed into the compound indices $1\ldots6$. Note that we already used time translation invariance to get rid of one time argument, as we did in sections 2.1 and 2.4 for the one- and two-particle Green's functions, respectively. A diagrammatic representation of the three-particle Green's function is shown in fig. 4.1.

The Fourier transformation to fermionic Matsubara frequencies $\nu_i = (2n_i+1)\pi/\beta$, $n_i \in \mathbb{Z}$, is given by

$$G^{\nu_1\ldots\nu_5}_{3,1\ldots6} = \int\cdots\int_0^\beta \mathrm{d}\tau_1\ldots\mathrm{d}\tau_5\, G_{3,1\ldots6}(\tau_1,\ldots,\tau_5)\mathrm{e}^{\mathrm{i}(\nu_1\tau_1-\nu_2\tau_2+\nu_3\tau_3-\nu_4\tau_4+\nu_5\tau_5)}, \tag{4.2}$$

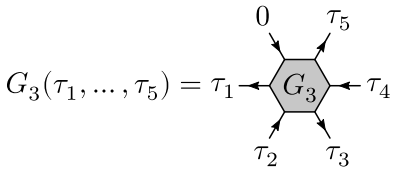

Figure 4.1.: Diagrammatic representation of the three-particle Green's function in imaginary times

and the inverse transformation reads

$$G_{3,1\dots6}(\tau_1, \dots, \tau_5) = \frac{1}{\beta^5} \sum_{\nu_1 \dots \nu_5} G^{\nu_1 \dots \nu_5}_{3,1\dots6} \mathrm{e}^{-\mathrm{i}(\nu_1\tau_1 - \nu_2\tau_2 + \nu_3\tau_3 - \nu_4\tau_4 + \nu_5\tau_5)}. \tag{4.3}$$

The transformations between real and reciprocal space work similarly and are straightforward to generalize from eqs. (2.4) to (2.6). With that we can infer the dimension of the three-particle Green's function in imaginary time and Matsubara space:

$$[G_{3,1\dots6}(\tau_1, \dots, \tau_5)] = 1, \tag{4.4}$$

$$[G^{\nu_1 \dots \nu_5}_{3,1\dots6}] = [\tau]^5. \tag{4.5}$$

From now on we drop the index 3 if the three-particle-ness can be inferred from the (number of) arguments.

4.2. Frequency notations

In section 2.4 we saw that there are three channels for the two-particle Green's function, each with its own frequency notation. They are chosen such that the in- and outgoing particle–particle or particle–hole pairs have a total energy of ω.

Making similar pairwise connections as in fig. 2.4, the number of different two-particle frequency notations for an n-particle function is equal to the number of different ways that the $2n$ points can be connected into pairs. This number of possibilities p is given by the double factorial

$$p(n) = (2n-1)!! = \prod_{k=1}^{n} (2k-1), \tag{4.6}$$

because with $2k$ remaining points there are $2k-1$ possibilities to connect an arbitrarily chosen point to one of the $2k-1$ other ones. The number of pure ph channels is $n!$ since in this case each of the n creation operators must be paired with one of the n annihilation operators and there are $n!$ unique ways to do that.

Table 4.1.: The 15 different two-particle frequency notations of three-particle diagrams

Channel	ν_1	ν_2	ν_3	ν_4	ν_5	ν_6
ph	ν_a	$\nu_a - \omega_a$	ν_b	$\nu_b - \omega_b$	ν_c	$\nu_c - \omega_c$
$\overline{\text{ph}}'$	ν_a	$\nu_b - \omega'_b$	ν_b	$\nu_c - \omega'_c$	ν_c	$\nu_a - \omega'_a$
$\overline{\text{ph}}$	ν_a	$\nu_c - \overline{\omega}_c$	ν_b	$\nu_a - \overline{\omega}_a$	ν_c	$\nu_b - \overline{\omega}_b$
$\text{ph}_{\overline{a}}$	ν_a	$\nu_b - \omega'_b$	ν_b	$\nu_a - \overline{\omega}_a$	ν_c	$\nu_c - \omega_c$
$\text{ph}_{\overline{b}}$	ν_a	$\nu_a - \omega_a$	ν_b	$\nu_c - \omega'_c$	ν_c	$\nu_b - \overline{\omega}_b$
$\text{ph}_{\overline{c}}$	ν_a	$\nu_c - \overline{\omega}_c$	ν_b	$\nu_b - \omega_b$	ν_c	$\nu_a - \omega'_a$
pp_{24-13}	ν_a	ν_b	$\omega_a - \nu_a$	$\omega_b - \nu_b$	ν_c	$\nu_c - \omega_c$
pp_{26-13}	$\omega_b - \nu_b$	ν_a	ν_b	$\nu_c - \omega'_c$	ν_c	$\omega_a - \nu_a$
pp_{26-15}	$\omega_c - \nu_c$	$\omega_a - \nu_a$	ν_b	$\nu_b - \omega_b$	ν_c	ν_a
pp_{46-15}	ν_a	$\nu_b - \omega'_b$	ν_b	$\omega_c - \nu_c$	$\omega_a - \nu_a$	ν_c
pp_{46-35}	ν_a	$\nu_a - \omega_a$	ν_b	ν_c	$\omega_b - \nu_b$	$\omega_c - \nu_c$
pp_{24-35}	ν_a	$\omega_b - \nu_b$	$\omega_c - \nu_c$	ν_b	ν_c	$\nu_a - \omega'_a$
pp_{26-35}	ν_a	ν_b	$\omega_c - \nu_c$	$\nu_a - \overline{\omega}_a$	ν_c	$\omega_b - \nu_b$
pp_{46-13}	$\omega_b - \nu_b$	$\nu_c - \overline{\omega}_c$	ν_b	$\omega_a - \nu_a$	ν_c	ν_a
pp_{24-15}	ν_a	$\omega_c - \nu_c$	ν_b	ν_c	$\omega_a - \nu_a$	$\nu_b - \overline{\omega}_b$

For the three-particle case this results in 15 different two-particle frequency notations which are shown in table 4.1. They can be divided into six ph channels and nine pp channels. A diagrammatic representation is given in figs. 4.2 and 4.3, depicting the ph and pp channels respectively.

Of course, we can also generalize to three-particle frequency notations where we combine either two particle lines and one hole line (pph) or three particle lines (ppp) such that they have a total energy of $\bar{\nu}$. In the pph case there are $\binom{3}{2} \cdot \binom{3}{1} = 9$ such combinations while in the ppp case there is only one for a total of ten three-particle frequency notations. All of them are listed in table 4.2 while a diagrammatic representation is shown for four of them in fig. 4.4.

4.3. Spin components and symmetries

An n-particle quantity has 2^{2n} spin degrees of freedom. However, due to spin conservation the number of nonvanishing spin combinations is lower than that: If k of the n ingoing spins are down, then also k of the n outgoing spins must be down. The order doesn't matter, so there are $\binom{n}{k}^2$ such configurations. Summing this over all possible numbers of ingoing down spins k yields the number of nonvanishing spin combinations. Using

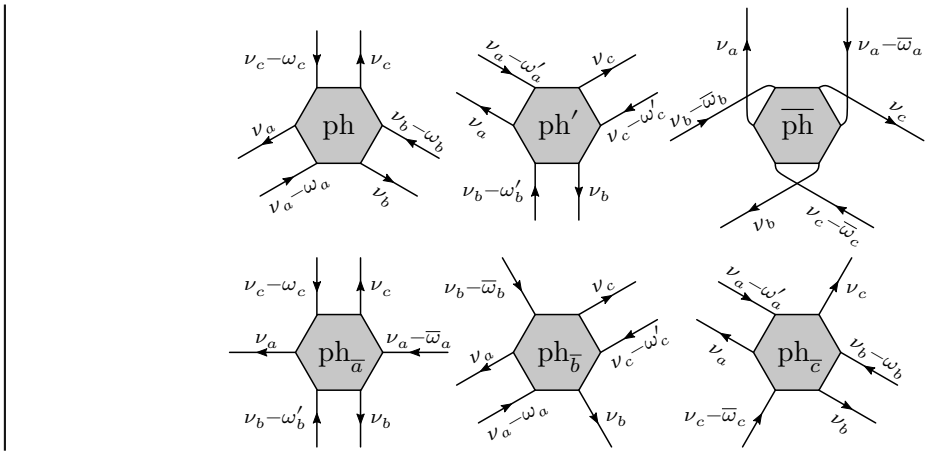

Figure 4.2.: Diagrammatic representation of the six ph frequency notations for three-particle diagrams

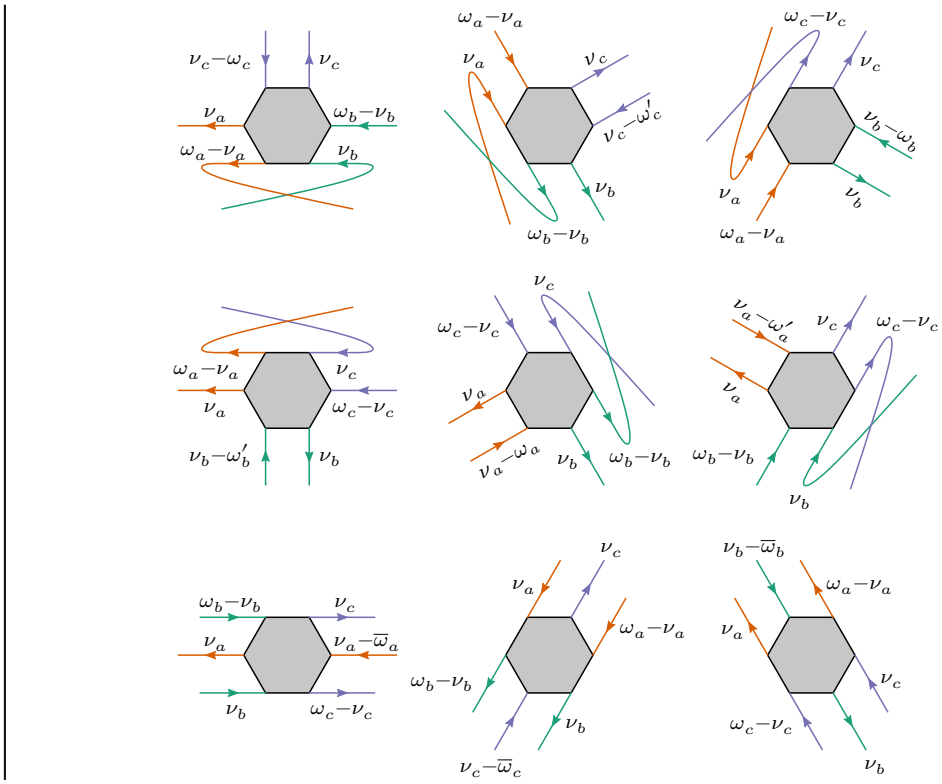

Figure 4.3.: Diagrammatic representation of the nine pp frequency notations for three-particle diagrams

Table 4.2.: The ten different three-particle frequency notations of three-particle diagrams. The channel names in the first column denote which particles and holes belong together. They all sum to a fermionic transfer frequency of $\bar{\nu}$. In the second column shorthand notations for the channel names are given. They consist of the middle numbers of the two triplets in the first column. For the pph channels (the first nine rows) they specify the particle running in the opposite direction. Diagrammatic representations for four of them are shown in fig. 4.4.

Channel		ν_1	ν_2	ν_3	ν_4	ν_5	ν_6
(345)(612)	41	$\nu+\omega$	ν	ν'	$\nu'+\omega'$	$\omega'-\bar{\nu}$	$\omega-\bar{\nu}$
(123)(456)	25	ν'	$\nu'+\omega'$	$\omega'-\bar{\nu}$	$\omega-\bar{\nu}$	$\nu+\omega$	ν
(561)(234)	63	$\omega'-\bar{\nu}$	$\omega-\bar{\nu}$	$\nu+\omega$	ν	ν'	$\nu'+\omega'$
(341)(652)	45	$\omega'-\bar{\nu}$	ν	ν'	$\nu'+\omega'$	$\nu+\omega$	$\omega-\bar{\nu}$
(361)(452)	65	$\omega'-\bar{\nu}$	ν	ν'	$\omega-\bar{\nu}$	$\nu+\omega$	$\nu'+\omega'$
(365)(412)	61	$\nu+\omega$	ν	ν'	$\omega-\bar{\nu}$	$\omega'-\bar{\nu}$	$\nu'+\omega'$
(325)(614)	21	$\nu+\omega$	$\nu'+\omega'$	ν'	ν	$\omega'-\bar{\nu}$	$\omega-\bar{\nu}$
(125)(634)	23	ν'	$\nu'+\omega'$	$\nu+\omega$	ν	$\omega'-\bar{\nu}$	$\omega-\bar{\nu}$
(145)(632)	43	ν'	ν	$\nu+\omega$	$\nu'+\omega'$	$\omega'-\bar{\nu}$	$\omega-\bar{\nu}$
(315)(642)	ppp	$\omega'-\nu'$	ν	ν'	$\omega-\nu$	$-\omega'-\bar{\nu}$	$-\omega-\bar{\nu}$

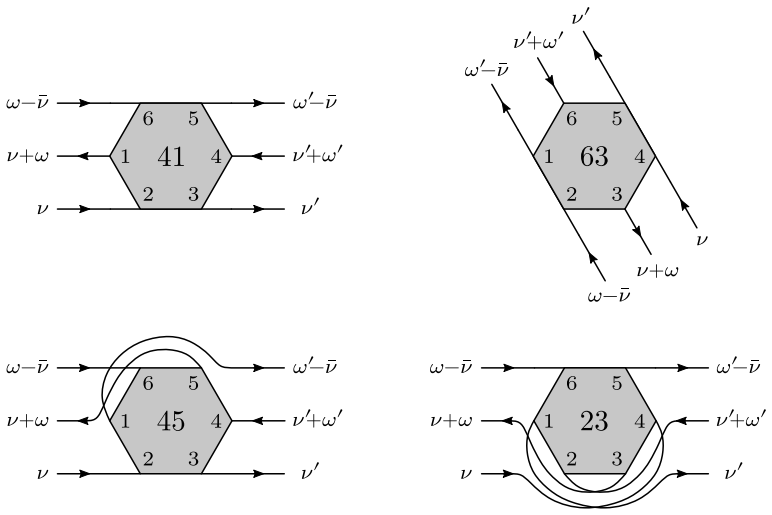

Figure 4.4.: Diagrammatic representation of four of the ten three-particle frequency notations listed in table 4.2

Vandermonde's identity, the sum can be simplified to

$$\sum_{k=0}^{n} \binom{n}{k}^2 = \binom{2n}{n}, \tag{4.7}$$

where the right side is the central binomial coefficient of n. For the three-particle Green's function this means that only $\binom{6}{3} = 20$ of the $2^6 = 64$ spin components are nonzero. They are

$$\begin{array}{ccccc} & \uparrow\uparrow\uparrow, & \uparrow\uparrow\downarrow, & \uparrow\downarrow\uparrow, & \downarrow\uparrow\uparrow, & \\ \bar{\uparrow}\uparrow\downarrow, & \uparrow\uparrow\bar{\downarrow}, & \uparrow\downarrow\bar{\uparrow}, & \bar{\uparrow}\downarrow\uparrow, & \downarrow\uparrow\bar{\uparrow}, & \bar{\downarrow}\uparrow\bar{\uparrow}, \\ \bar{\downarrow}\downarrow\bar{\uparrow}, & \downarrow\downarrow\bar{\uparrow}, & \downarrow\uparrow\bar{\downarrow}, & \bar{\downarrow}\uparrow\downarrow, & \uparrow\downarrow\bar{\downarrow}, & \bar{\uparrow}\downarrow\bar{\downarrow}, \\ & \downarrow\downarrow\downarrow, & \downarrow\downarrow\uparrow, & \downarrow\uparrow\downarrow, & \uparrow\downarrow\downarrow, & \end{array} \tag{4.8}$$

where we generalize the compact spin notation from the two-particle level [see eq. (2.35)]:

$$\begin{aligned} \sigma_1\sigma_2\sigma_3 &= \sigma_1\sigma_1\sigma_2\sigma_2\sigma_3\sigma_3, \\ \sigma_1\overline{\sigma_2\sigma_3} &= \sigma_1\sigma_1\sigma_2\sigma_3\sigma_3\sigma_2, \\ \overline{\sigma_1}\sigma_2\overline{\sigma_3} &= \sigma_1\sigma_3\sigma_2\sigma_2\sigma_3\sigma_1, \\ \overline{\sigma_1\sigma_2}\sigma_3 &= \sigma_1\sigma_2\sigma_2\sigma_1\sigma_3\sigma_3. \end{aligned} \tag{4.9}$$

These spin components are, however, not independent. There are symmetry relations between them. In particular, we have the SU(2), swapping (SW) and time reversal (TR) symmetry:

$$G^{\nu_1\omega_1\nu_2\omega_2\nu_3}_{\sigma_1\dots\sigma_6} \overset{\mathrm{SU(2)}}{=} G^{\nu_1\omega_1\nu_2\omega_2\nu_3}_{-\sigma_1\cdots-\sigma_6}, \tag{4.10}$$

$$G^{\nu_1\omega_1\nu_2\omega_2\nu_3}_{\sigma_1\dots\sigma_6} \overset{\mathrm{SW12}}{=} G^{\nu_2\omega_2\nu_1\omega_1\nu_3}_{\sigma_3\sigma_4\sigma_1\sigma_2\sigma_5\sigma_6}, \tag{4.11}$$

$$G^{\nu_1\omega_1\nu_2\omega_2\nu_3}_{\sigma_1\dots\sigma_6} \overset{\mathrm{SW13}}{=} G^{\nu_3\omega_3\nu_2\omega_2\nu_1}_{\sigma_5\sigma_6\sigma_3\sigma_4\sigma_1\sigma_2}, \tag{4.12}$$

$$G^{\nu_1\omega_1\nu_2\omega_2\nu_3}_{\sigma_1\dots\sigma_6} \overset{\mathrm{SW23}}{=} G^{\nu_1\omega_1\nu_3\omega_3\nu_2}_{\sigma_1\sigma_2\sigma_5\sigma_6\sigma_3\sigma_4}, \tag{4.13}$$

$$G^{\nu_1\omega_1\nu_2\omega_2\nu_3}_{\sigma_1\dots\sigma_6} \overset{\mathrm{TR}}{=} G^{(\nu_3-\omega_3)(-\omega_3)(\nu_2-\omega_2)(-\omega_2)(\nu_1-\omega_1)}_{\sigma_6\dots\sigma_1}, \tag{4.14}$$

where $-\uparrow=\downarrow$, $-\downarrow=\uparrow$, $\omega_3 = -\omega_1 - \omega_2$, and we use the ph notation introduced in section 4.2.

With all these symmetry relations the original 20 spin components can be mapped to only three, namely $\uparrow\uparrow\uparrow$, $\uparrow\uparrow\downarrow$, and $\uparrow\uparrow\overline{\downarrow}$. For the other seven out of the first ten spin components,

the necessary transformations read

$$G^{\nu_1\omega_1\nu_2\omega_2\nu_3}_{\uparrow\downarrow\uparrow} \overset{\text{SW}23}{=} G^{\nu_1\omega_1\nu_3\omega_3\nu_2}_{\uparrow\uparrow\downarrow}, \tag{4.15}$$

$$G^{\nu_1\omega_1\nu_2\omega_2\nu_3}_{\downarrow\uparrow\uparrow} \overset{\text{SW}13}{=} G^{\nu_3\omega_3\nu_2\omega_2\nu_1}_{\uparrow\uparrow\downarrow}, \tag{4.16}$$

$$G^{\nu_1\omega_1\nu_2\omega_2\nu_3}_{\bar{\uparrow}\uparrow\bar{\downarrow}} \overset{\text{SW}12}{=} G^{\nu_2\omega_2\nu_1\omega_1\nu_3}_{\uparrow\bar{\uparrow}\bar{\downarrow}}, \tag{4.17}$$

$$G^{\nu_1\omega_1\nu_2\omega_2\nu_3}_{\uparrow\bar{\downarrow}\uparrow} \overset{\text{SW}23}{=} G^{\nu_1\omega_1\nu_3\omega_3\nu_2}_{\uparrow\bar{\uparrow}\bar{\downarrow}}, \tag{4.18}$$

$$G^{\nu_1\omega_1\nu_2\omega_2\nu_3}_{\bar{\uparrow}\downarrow\uparrow} \overset{\text{SW}23}{=} G^{\nu_1\omega_1\nu_3\omega_3\nu_2}_{\bar{\uparrow}\uparrow\bar{\downarrow}} \overset{\text{SW}12}{=} G^{\nu_3\omega_3\nu_1\omega_1\nu_2}_{\uparrow\bar{\uparrow}\bar{\downarrow}}, \tag{4.19}$$

$$G^{\nu_1\omega_1\nu_2\omega_2\nu_3}_{\bar{\downarrow}\uparrow\uparrow} \overset{\text{SW}13}{=} G^{\nu_3\omega_3\nu_2\omega_2\nu_1}_{\uparrow\bar{\uparrow}\bar{\downarrow}}, \tag{4.20}$$

$$G^{\nu_1\omega_1\nu_2\omega_2\nu_3}_{\bar{\downarrow}\uparrow\bar{\uparrow}} \overset{\text{SW}12}{=} G^{\nu_2\omega_2\nu_1\omega_1\nu_3}_{\uparrow\bar{\downarrow}\bar{\uparrow}} \overset{\text{SW}23}{=} G^{\nu_2\omega_2\nu_3\omega_3\nu_1}_{\uparrow\bar{\uparrow}\bar{\downarrow}}. \tag{4.21}$$

Note that they are not unique. $G_{\bar{\uparrow}\downarrow\uparrow}$, e.g., can also be calculated from $G_{\uparrow\bar{\uparrow}\bar{\downarrow}}$ by applying time reversal symmetry. The second half of the 20 nonvanishing components can be mapped to the these first ten by using SU(2) symmetry.

4.4. Decomposition

It is common to decompose the two-particle Green's function into the three terms shown in eq. (2.37) and fig. 2.5. To properly generalize this to the three- or even n-particle level we need to determine the essence of what is done on the two-particle level. From the discussion in section 2.5, it is sensible to propose that the two-particle Green's function is classified into terms of different connectedness. The first two diagrams are only made of Green's function lines G, which contain all diagrams that connect two points. The third term introduces the full two-particle vertex F_2, which consists of all diagrams that fully connect four points. Continuing this to the n-particle level we expect n-particle vertices F_n containing all diagrams that connect $2n$ points, but also terms of mixed connectedness with "smaller" vertices.

This means that to compute all such terms for an n-particle Green's function, we need to decompose its expectation value into all possible sets of connected tuples of creation and annihilation operators. Denoting the connected tuples by underlined expectation values, the one-particle case is trivially written as

$$G_{12} = -\langle \mathrm{T}\, \hat{c}_1 \hat{c}_2^\dagger \rangle = -\underline{\langle \mathrm{T}\, \hat{c}_1 \hat{c}_2^\dagger \rangle}. \tag{4.22}$$

On the two-particle level we get

$$G_{1234} = \langle \mathrm{T}\, \hat{c}_1 \hat{c}_2^\dagger \hat{c}_3 \hat{c}_4^\dagger \rangle = \underline{\langle \mathrm{T}\, \hat{c}_1 \hat{c}_2^\dagger \hat{c}_3 \hat{c}_4^\dagger \rangle} + \underline{\langle \mathrm{T}\, \hat{c}_1 \hat{c}_2^\dagger \rangle} \underline{\langle \mathrm{T}\, \hat{c}_3 \hat{c}_4^\dagger \rangle} + (-1)^3 \underline{\langle \mathrm{T}\, \hat{c}_1 \hat{c}_4^\dagger \rangle} \underline{\langle \mathrm{T}\, \hat{c}_3 \hat{c}_2^\dagger \rangle}, \tag{4.23}$$

where the $(-1)^3$ comes of course from reordering the fermionic operators. Comparison with eq. (2.37) and fig. 2.5 shows that we do indeed end up with the correct signs for the

disconnected terms. Furthermore, we see that the four-point expectation value is given by

$$\langle \underline{\mathrm{T}\, \hat{c}_1 \hat{c}_2^\dagger \hat{c}_3 \hat{c}_4^\dagger} \rangle = -G_{15} G_{62} F_{5678} G_{37} G_{84}. \tag{4.24}$$

After this proof of concept, we can finally move on to the decomposition of the three-particle Green's function:

$$\begin{aligned}
G_{123456} = & -\langle \mathrm{T}\, \hat{c}_1^\dagger \hat{c}_2 \hat{c}_3^\dagger \hat{c}_4 \hat{c}_5^\dagger \hat{c}_6 \rangle \\
= & -\langle \underline{\mathrm{T}\, \hat{c}_1 \hat{c}_2^\dagger} \rangle \langle \underline{\mathrm{T}\, \hat{c}_3 \hat{c}_4^\dagger} \rangle \langle \underline{\mathrm{T}\, \hat{c}_5 \hat{c}_6^\dagger} \rangle - \langle \underline{\mathrm{T}\, \hat{c}_1 \hat{c}_6^\dagger} \rangle \langle \underline{\mathrm{T}\, \hat{c}_3 \hat{c}_2^\dagger} \rangle \langle \underline{\mathrm{T}\, \hat{c}_5 \hat{c}_4^\dagger} \rangle \\
& -\langle \underline{\mathrm{T}\, \hat{c}_1 \hat{c}_4^\dagger} \rangle \langle \underline{\mathrm{T}\, \hat{c}_3 \hat{c}_6^\dagger} \rangle \langle \underline{\mathrm{T}\, \hat{c}_5 \hat{c}_2^\dagger} \rangle + \langle \underline{\mathrm{T}\, \hat{c}_1 \hat{c}_2^\dagger} \rangle \langle \underline{\mathrm{T}\, \hat{c}_3 \hat{c}_6^\dagger} \rangle \langle \underline{\mathrm{T}\, \hat{c}_5 \hat{c}_4^\dagger} \rangle \\
& +\langle \underline{\mathrm{T}\, \hat{c}_1 \hat{c}_6^\dagger} \rangle \langle \underline{\mathrm{T}\, \hat{c}_3 \hat{c}_4^\dagger} \rangle \langle \underline{\mathrm{T}\, \hat{c}_5 \hat{c}_2^\dagger} \rangle + \langle \underline{\mathrm{T}\, \hat{c}_1 \hat{c}_4^\dagger} \rangle \langle \underline{\mathrm{T}\, \hat{c}_3 \hat{c}_2^\dagger} \rangle \langle \underline{\mathrm{T}\, \hat{c}_5 \hat{c}_6^\dagger} \rangle \\
& -\langle \underline{\mathrm{T}\, \hat{c}_1 \hat{c}_2^\dagger} \rangle \langle \underline{\mathrm{T}\, \hat{c}_3 \hat{c}_4^\dagger \hat{c}_5 \hat{c}_6^\dagger} \rangle - \langle \underline{\mathrm{T}\, \hat{c}_3 \hat{c}_4^\dagger} \rangle \langle \underline{\mathrm{T}\, \hat{c}_5 \hat{c}_6^\dagger \hat{c}_1 \hat{c}_2^\dagger} \rangle - \langle \underline{\mathrm{T}\, \hat{c}_5 \hat{c}_6^\dagger} \rangle \langle \underline{\mathrm{T}\, \hat{c}_1 \hat{c}_2^\dagger \hat{c}_3 \hat{c}_4^\dagger} \rangle \\
& +\langle \underline{\mathrm{T}\, \hat{c}_1 \hat{c}_4^\dagger} \rangle \langle \underline{\mathrm{T}\, \hat{c}_3 \hat{c}_2^\dagger \hat{c}_5 \hat{c}_6^\dagger} \rangle + \langle \underline{\mathrm{T}\, \hat{c}_3 \hat{c}_6^\dagger} \rangle \langle \underline{\mathrm{T}\, \hat{c}_5 \hat{c}_4^\dagger \hat{c}_1 \hat{c}_2^\dagger} \rangle + \langle \underline{\mathrm{T}\, \hat{c}_5 \hat{c}_2^\dagger} \rangle \langle \underline{\mathrm{T}\, \hat{c}_1 \hat{c}_6^\dagger \hat{c}_3 \hat{c}_4^\dagger} \rangle \\
& +\langle \underline{\mathrm{T}\, \hat{c}_1 \hat{c}_6^\dagger} \rangle \langle \underline{\mathrm{T}\, \hat{c}_3 \hat{c}_4^\dagger \hat{c}_5 \hat{c}_2^\dagger} \rangle + \langle \underline{\mathrm{T}\, \hat{c}_3 \hat{c}_2^\dagger} \rangle \langle \underline{\mathrm{T}\, \hat{c}_5 \hat{c}_6^\dagger \hat{c}_1 \hat{c}_4^\dagger} \rangle + \langle \underline{\mathrm{T}\, \hat{c}_5 \hat{c}_4^\dagger} \rangle \langle \underline{\mathrm{T}\, \hat{c}_1 \hat{c}_2^\dagger \hat{c}_3 \hat{c}_6^\dagger} \rangle \\
& -\langle \underline{\mathrm{T}\, \hat{c}_1 \hat{c}_2^\dagger \hat{c}_3 \hat{c}_4^\dagger \hat{c}_5 \hat{c}_6^\dagger} \rangle.
\end{aligned} \tag{4.25}$$

A diagrammatic representation of this is shown in fig. 4.5. As expected the decomposition of the three-particle Green's function is much more complex and contains many more terms than that of the two-particle one. We get six fully disconnected terms with only Green's function lines, nine terms of mixed connectedness including two-particle vertices, as well as one fully connected term, introducing the full three-particle vertex F_3. Its sign is chosen as

$$-\langle \underline{\mathrm{T}\, \hat{c}_1 \hat{c}_2^\dagger \hat{c}_3 \hat{c}_4^\dagger \hat{c}_5 \hat{c}_6^\dagger} \rangle = G_{1'1} G_{22'} G_{3'3} F_{3,1'2'3'4'5'6'} G_{44'} G_{5'5} G_{66'}. \tag{4.26}$$

Looking at fig. 4.5 it might seem like some diagrams are "obviously" missing. They are, however, just topologically equivalent to some already present ones. Examples for such equivalent diagrams are depicted in fig. 4.6.

Of course, when we consider spin, some terms of the decomposition vanish because they break spin conservation. As shown in section 4.3, only three spin components of the three-particle Green's function, namely $\uparrow\uparrow\uparrow$, $\uparrow\uparrow\downarrow$, and $\uparrow\overline{\uparrow\downarrow}$, are independent, so it is sufficient to look at only those. For the first one, with all spins up, all terms are allowed, for the other two components though, only half of the terms survive. They are depicted in figs. 4.7 and 4.8 for the spin components $\uparrow\uparrow\downarrow$ and $\uparrow\overline{\uparrow\downarrow}$ respectively.

4.5. Vertex expansion

In section 4.4 we showed the arguably most sensible generalization of the decomposition of the two-particle Green's function [eq. (2.37) and fig. 2.5] to the n-particle level. It yields

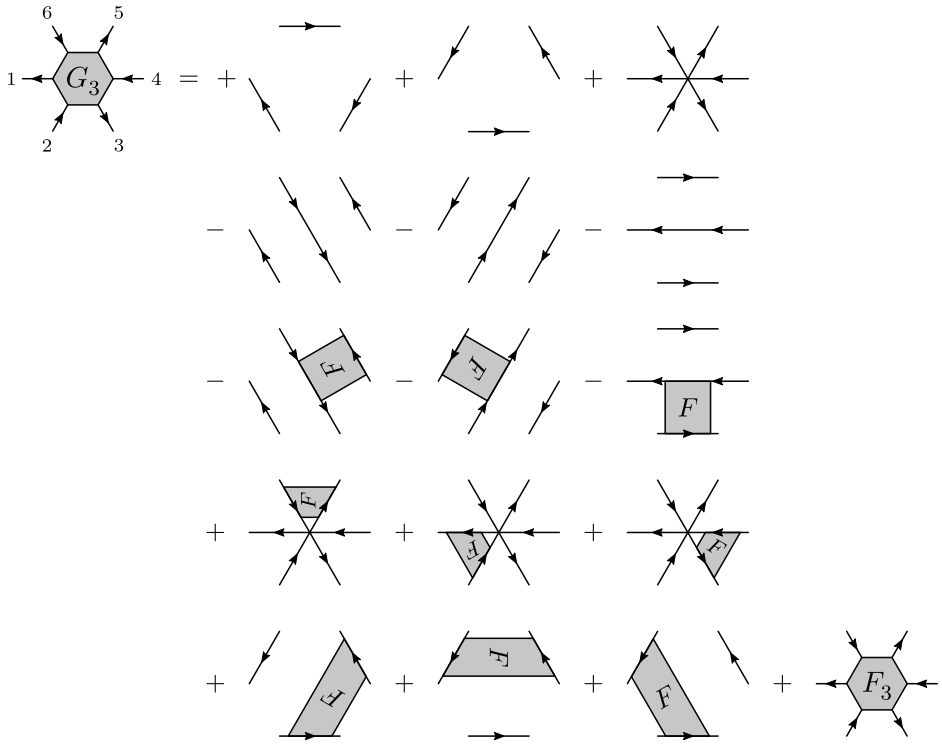

Figure 4.5.: Diagrammatic representation of eq. (4.25), the decomposition of the three-particle Green's function

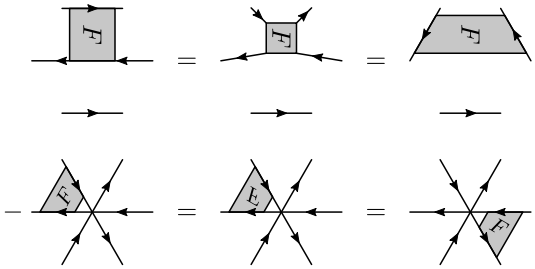

Figure 4.6.: Some topologically equivalent diagrams that appear in the decomposition of the three-particle Green's function shown in fig. 4.5. In the second line we use the crossing symmetry of F for the first identity. Otherwise, only continuous deformations are applied.

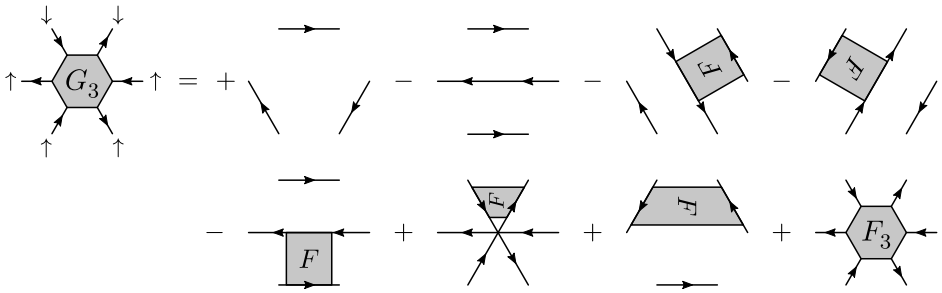

Figure 4.7.: Diagrammatic representation of the decomposition of the $\uparrow\uparrow\downarrow$ component of the three-particle Green's function

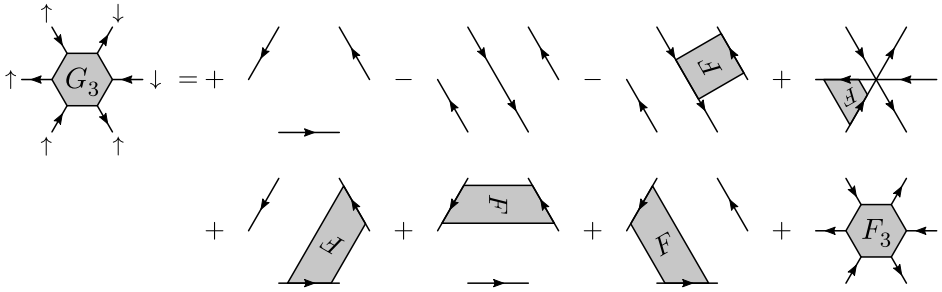

Figure 4.8.: Diagrammatic representation of the decomposition of the $\uparrow\uparrow\overline{\downarrow}$ component of the three-particle Green's function

a finite although combinatorially growing number of terms, where the last one always introduces the full n-particle vertex. There is, however, another useful generalization of the decomposition, namely what we call the n-particle vertex expansion.

This is similar to the more commonly known skeleton expansion, where bare one-particle Green's functions are replaced with full ones, while diagrams with one-particle insertions are banned. One-particle insertions are subdiagrams that connect two points and are more complicated than a single Green's function line. Those subdiagrams are not allowed because the full Green's function already contains all such corrections, so we would overcount otherwise. The n-particle vertex expansion goes a step further and also replaces bare interactions with full two- to n-particle vertices, while additionally banning two- to n-particle insertions. Similar to the one-particle case an n-particle insertion with $n \geq 2$ is a subdiagram that connects $2n$ points and is more complicated than a single n-particle vertex. The reason for banning those insertions is the same as before: avoiding overcounting since the full vertices already contain all those corrections. With the decomposition in section 4.4 using full Green's functions and vertices, and the "largest" vertex being a three-particle one, we can also call it the three-particle vertex expansion of the three-particle Green's function.

There is no requirement that the vertex expansion must go up to the "largest" possible vertex, though. We can just as well do a two-particle vertex expansion of the three-particle Green's function. Of course this expansion is no longer finite, so we have to truncate at some point and only get an approximate solution. Since the three-particle Green's function with its five degrees of freedom per spacetime dimension is expected to be very expensive to compute, such an approximation built simply from full Green's functions G and two-particle vertices F seems interesting and useful. The rest of this section is therefore dedicated to computing the two-particle vertex expansion of the three-particle Green's function up to third order.

4.5.1. Order 0

The diagrams of zeroth order contain no vertex and consist only of three Green's functions G. This means that they are given by all pairwise contractions of $\langle \mathrm{T}\, \hat{c}_1 \hat{c}_2^\dagger \hat{c}_3 \hat{c}_4^\dagger \hat{c}_5 \hat{c}_6^\dagger \rangle$. There are $3! = 6$ such diagrams because there are 3! ways to pair the creation and annihilation operators: the first creation operator can be connected to one of three annihilation operators, the next one to two, and the last one to the remaining one.

Figure 4.9 shows all six diagrams of zeroth order, which are the same as the first six diagrams of the decomposition of the three-particle Green's function in fig. 4.5. For spin component $\uparrow\uparrow\downarrow$ only the first and last diagram are allowed; for $\uparrow\overline{\uparrow\downarrow}$ only the second and forth.

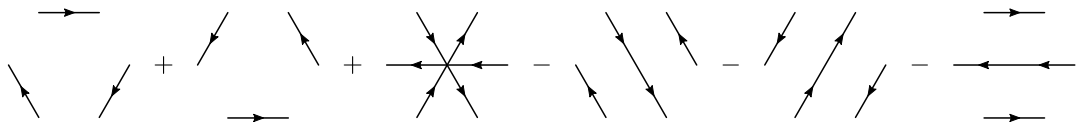

Figure 4.9.: Zeroth-order diagrams of the two-particle vertex expansion of the three-particle Green's function.

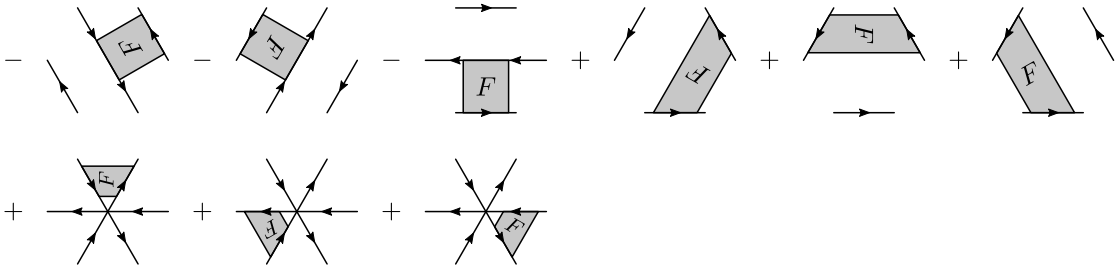

Figure 4.10.: First-order diagrams of the two-particle vertex expansion of the three-particle Green's function.

4.5.2. Order 1

The diagrams of first order contain a full two-particle vertex F with four Green's functions and one separate Green's function. Due to the crossing symmetry of the vertex, exchanging its legs does not yield new, inequivalent diagrams. Therefore, only the different ways to connect two of the external points with the separate Green's function are important for counting the number of diagrams of this order. There are $3^2 = 9$ such possibilities since one of the three creation operators must be connected to one of the three annihilation operators by a one-particle Green's function.

Figure 4.10 shows all nine diagrams of first order, which are the same as the diagrams with one vertex from the decomposition of the three-particle Greens's function in fig. 4.5. As already mentioned in section 4.4, it might seem like some "obvious" diagrams are missing, but they are just topologically equivalent to the ones already preset (see fig. 4.6). For spin component $\uparrow\uparrow\downarrow$ the fourth, sixth, eighth, and ninth diagram are forbidden due to spin conservation. For component $\uparrow\overline{\uparrow\downarrow}$, diagrams two, three, seven, and nine are not allowed for the same reason.

4.5.3. Order 2

The diagrams of second order contain two, full two-particle vertices F connected to each other with a single Green's function G. If we connected two legs of the same vertex, we would end up with a one-particle insertion, which is not allowed. Also, it doesn't matter how the two vertices are connected, or, put differently, all ways to connect them

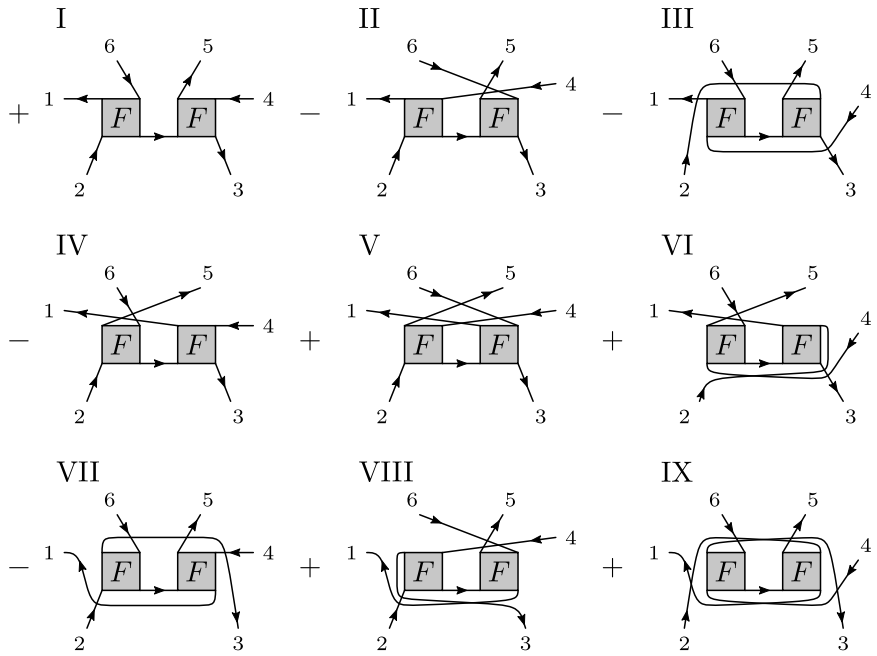

Figure 4.11.: Second-order diagrams of the two-particle vertex expansion of the three-particle Green's function.

are equivalent. The Green's function always goes from an outgoing leg of the first vertex to an ingoing leg of the second one. Choosing the other in- or outgoing leg only gives a sign, because of the crossing symmetry, and since the vertices are indistinguishable it does not matter which one is the first and which one the second.

Now that we have established that there is only a single "base diagram" (diagram I in fig. 4.11) we can generate all diagrams of second order by finding all topologically inequivalent ways to connect the six legs of this base diagram (termed internal legs) with the six external legs (numbered 1 to 6 in fig. 4.11). With three ingoing and three outgoing Green's functions we should have $(3!)^2 = 36$ such possibilities. There are, however, two in- and two outgoing Green's functions connected to one vertex each (1 and 3 as well as 4 and 6 in diagram I in fig. 4.11). This means, again, due to crossing symmetry swapping the corresponding legs of the vertices does not yield new diagrams. Therefore, there are only $(3!)^2/2^2 = 9$ topologically inequivalent second-order diagrams. They are all shown in fig. 4.11.

We can deform these diagrams and use the crossing symmetry to make things clearer. Figure 4.12, e.g., shows many diagrams that are equivalent to diagram III. Similar equations hold for diagrams II, IV, V, VII, and IX. Figure 4.13 shows five diagrams that also look very different at first glance. Upon closer inspection tough, we realize that they are in fact all topologically equivalent to diagram I. Similar equations hold for diagrams VI and VIII. With all this, the nine second-order diagrams of the two-particle vertex

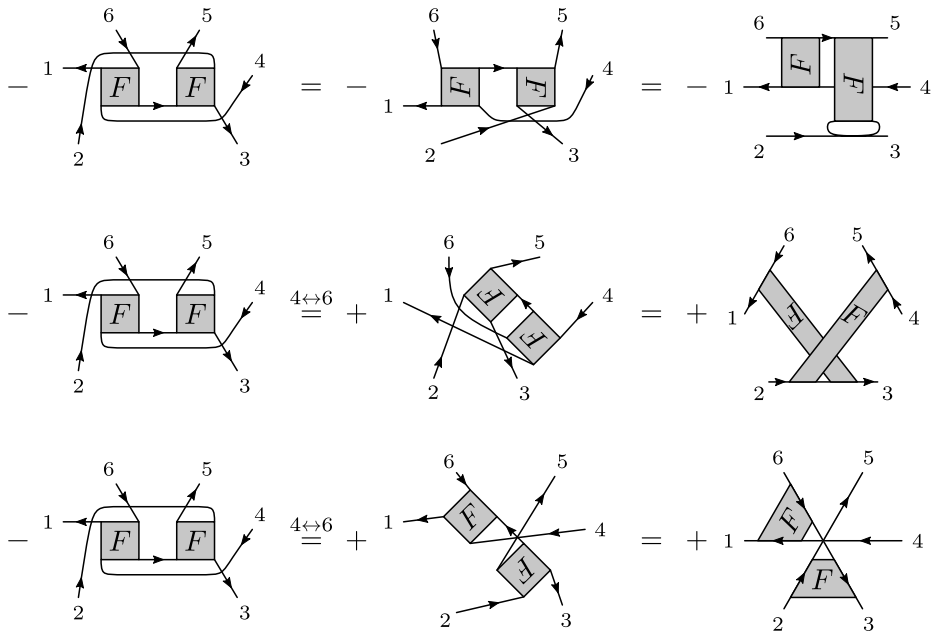

Figure 4.12.: Second-order diagrams that are topologically equivalent to diagram III in fig. 4.11

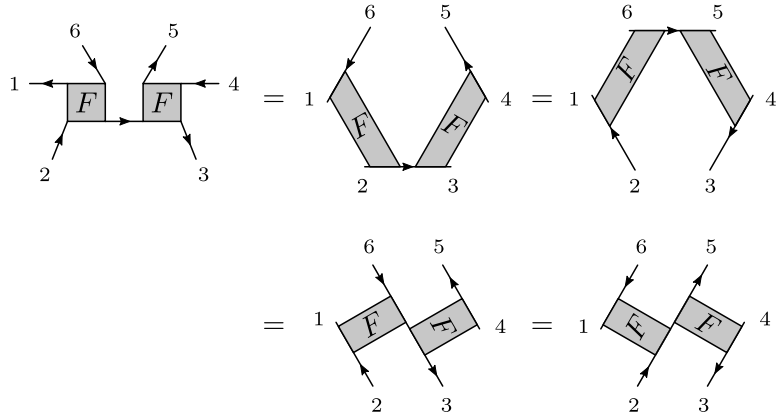

Figure 4.13.: Second-order diagrams that are topologically equivalent to diagram I in fig. 4.11

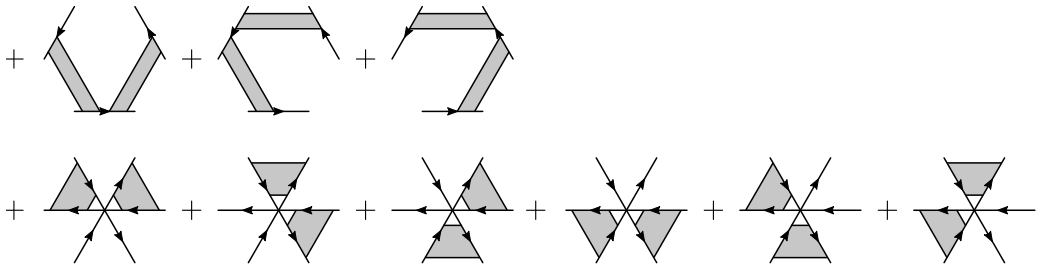

Figure 4.14.: Second-order diagrams of the two-particle vertex expansion of the three-particle Green's function. They are equivalent to fig. 4.11 but with the help of figs. 4.12 and 4.13 drawn in a more visually pleasing way.

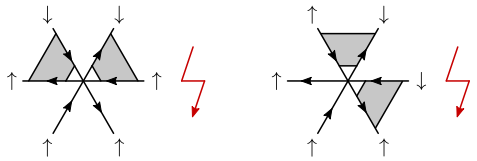

Figure 4.15.: Second-order diagrams that are forbidden for the depicted spin component. In both cases there is a two-particle vertex with two ingoing (outgoing) up spins but an outgoing (ingoing) down spin which violates spin conservation.

expansion of the three-particle Green's function can be represented in a visually more pleasing way that is shown in fig. 4.14.

If spin is considered the number of diagrams (per spin component) does not increase since both vertices are connected to three external legs, and thus the external spins uniquely determine the spin of the internal line. For spin component $\uparrow\uparrow\uparrow$, as usual all diagrams are allowed. For $\uparrow\uparrow\downarrow$ and $\uparrow\uparrow\overline{\downarrow}$, however, there is one diagram each that is forbidden due to spin conservation. The forbidden diagrams are shown in fig. 4.15.

4.5.4. Order 3

As with the diagrams of order two, we first find all inequivalent, third-order base diagrams and then determine all possible inequivalent ways to connect the six remaining legs to the six external ones. The base diagrams of third order contain three, full two-particle vertices F connected to each other with three Green's functions G. Again, connecting two legs of the same vertex, as well as connecting two different vertices with two Green's functions is forbidden because the former generates one-particle insertions, and the latter two-particle insertions. Therefore, all three vertices must be connected to each other in a chain.

Since the vertices are indistinguishable and because of the crossing symmetry, there are only two inequivalent chains. Both of them are shown in fig. 4.16 together with some

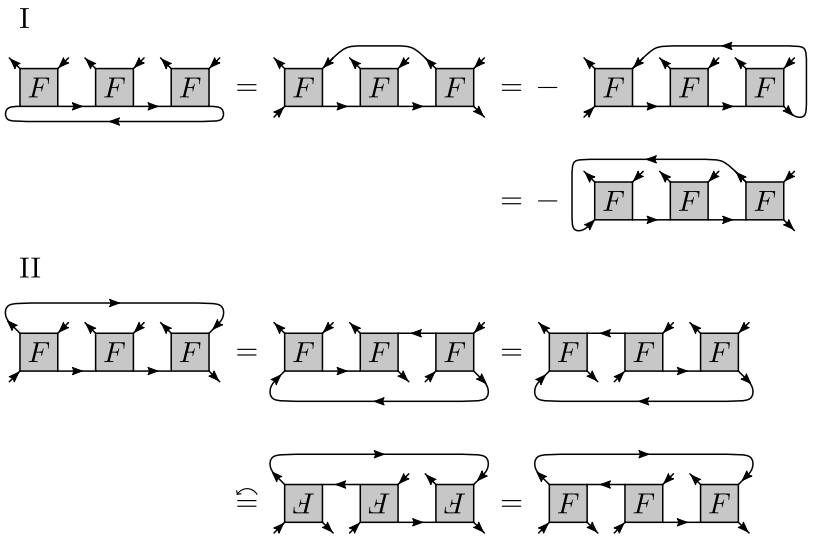

Figure 4.16.: The two base diagrams for the third order of the two-particle vertex expansion of the three-particle Green's function, together with some topologically equivalent variations. In the last identity of the last line we used both crossing symmetries of each vertex F to effectively rotate them by 180°.

topologically equivalent variations. In diagrams of type I every vertex has one remaining ingoing and one outgoing leg. Type II diagrams have one vertex with two remaining ingoing legs, one with two remaining outgoing legs, and one with one remaining ingoing and one outgoing leg.

Again, the number of ways to connect the six legs of the base diagrams with the six external legs is $(3!)^2 = 36$. The actual number of diagrams can, however, be reduced by symmetries. For diagram II we can employ the much-used crossing symmetry for the two ingoing and the two outgoing legs, ending up with $(3!)^2/2^2 = 9$ inequivalent diagrams.

For diagram I we must consider a new type of symmetry namely cyclic permutations. So far that was not necessary because, while "naked" vertices F are indistinguishable, the ones in the base diagrams differed due to their connections with the other vertices. We already described that for diagram II, but also in the second-order base diagram the vertices are easily distinguished: because of the Green's function connecting them, one "loses" an ingoing leg, the other one an outgoing leg. In diagram I, however, all three vertices have one ingoing and one outgoing leg, so they cannot be uniquely identified and since they are connected in a chain, cyclic permutations yield topologically equivalent diagrams.

With three vertices there are three possible cyclic permutations so the number of inequivalent diagrams of type I is $(3!)^2/3 = 12$. This finally brings us to the total number of inequivalent diagrams of third order which is $12 + 9 = 21$.

Drawing and studying all of them is beyond the scope of this thesis because we believe that doing so only yields little insight, especially relative to the amount of tedious work it would require. Based on experience with two-particle ladders, we also have the intuition that the three-particle ladder introduced in chapter 6 yields a better approximation for the three-particle vertex. Therefore, we study that in more detail and also provide numerical results for it.

5. Three-particle correlators and nonlinear response

Parts of this chapter marked with a vertical bar have already been published in Kappl et al. [55]. Some figures were adapted to better fit the page layout.

Equipped with all the theoretical knowledge about the three-particle Green's function from the last chapter, this chapter presents a physical application for three-particle correlations. As we already saw in section 2.8 computing response functions in imaginary time or Matsubara frequencies is tied to calculating correlation functions. In particular bosonic three-particle correlators are required for second-order response functions like Raman, Hall, or nonlinear density and magnetic responses.

We first work through a bit more theory and provide a general formalism for the three-particle correlators and second-order susceptibilities. Then we focus on charge and spin operators and compute their local nonlinear responses, mainly for the Anderson impurity model (AIM), numerically. We show that for certain ranges in the parameter space, these second-order susceptibilities are sizable. Furthermore, we find that contributions from the full three-particle vertex play a significant role in them. Approximations that just take into account the bare bubble terms or corrections based on the two-particle vertex are not sufficient and can lead to qualitatively wrong results for second-order response functions.

5.1. Introduction

Our physical understanding is very much based on one-particle and two-particle Green's functions, upon which books on quantum field theory (QFT) generally focus [12]. On the one-particle level, we understand quasiparticle renormalizations and life times, metal–insulator transitions, as well as magnetic ordering in the symmetry-broken phase. The one-particle Green's function and self-energy are also at the heart of dynamical mean-field theory (DMFT) [35–37, 56], which calculates the self-energy by (self-consistently) summing up the local contribution of all Feynman diagrams [35]. Hence, it is maybe not surprising that the success of DMFT had a focus on describing the aforementioned one-particle properties such as quasiparticle renormalizations and the Mott–Hubbard metal–insulator transition.

On the two-particle level, we have the two-particle Green's function from which we can calculate physical responses such as the magnetic or charge susceptibility. Here, the two-particle vertex plays the role of the self-energy. It describes all physics beyond a rather trivial bare bubble susceptibility which is akin to the noninteracting case, only now with renormalized one-particle Green's function lines. On this two-particle level there has been some recent progress to describe electronic correlations – brought about through diagrammatic extensions of DMFT [51–53, 57–60]; for a review, see ref. [18]. These start from a local vertex that encodes all DMFT correlations and subsequently generates nonlocal correlations through the Bethe–Salpeter equation or parquet equations. Quite naturally these extensions allow for a better description of two-particle quantities such as the (quantum) critical behavior in the vicinity of a phase transition [61–64], spin-fluctuation-induced pseudogaps [47, 65, 66], and superconducting instabilities [67, 68].

The next level, the three-particle Green's function and vertices, are hitherto by-and-large a blank spot in our understanding of strongly correlated electron systems. First results for the diagrammatic extensions of DMFT [3] show that three-particle vertices are, at least in some parameter regimes of the Hubbard model (HM), relevant. While our physical understanding and intuition is presently much more based on the one- and two-particle physics, there are also physical processes that are generically connected to three-particle correlators:

Take for example Raman scattering, with an incoming and outgoing light frequency and a transferred phonon frequency. These three bosonic frequencies are connected to three electrons (particles), each with one creation and one annihilation operator. The same applies to the Hall response, i.e., the off-diagonal conductivity in a magnetic field. The conductivity by itself is a two-particle correlator in the Kubo formalism of linear response [20]. Considering small magnetic fields, these can be treated in linear response as well, making the Hall coefficient a three-particle correlator altogether. In principle, calculating these observables requires the calculation of the full three-particle correlator. But hitherto either only a bare bubble-like diagram is taken or corrections based on the two-particle vertex are included; see, e.g., [69–71].

Another research area which is the domain of correlators with more than two particles is nonlinear response [20, 72]. These responses are in general weaker than linear responses and often the most relevant correction is thus the second-order response that is connected to a three-particle correlator. Interestingly, refs. [73, 74] found that correlation effects can enhance nonlinear responses in strongly correlated electron systems, but, again, they only took into account one-particle renormalizations; full vertex corrections were still neglected.

Three-particle correlators are also employed for calculating two-particle correlators reliably using the so-called improved estimators based on the equation of motion [75–79].

Against this background, it is the aim of the present paper to do some first steps in computing, analyzing, and understanding these three-particle correlators. Specifically, we consider correlators of three bosonic operators and thus three time arguments (or two time differences or frequencies). For the sake of simplicity, and for keeping the numerical effort manageable, we concentrate on local correlators of an AIM (including one at DMFT self-consistency for the two-dimensional HM). Since the Raman and Hall response couple to light through nonlocal fermionic operators, we focus here on the nonlinear response described by local operators only. There are just three local nonvanishing three-particle correlators (and symmetrically related ones): a second-order density susceptibility (nnn) with three density operators, a mixed density-magnetic susceptibility (nzz) describing the second-order response of the density to a magnetic field in z direction, and a chiral susceptibility (xyz). The latter corresponds to a correlator with one spin in all three directions. These are arranged like thumb, index, and middle finger of the right hand and hence chiral according to the definition introduced by Kelvin in 1884 [80] (not invariant under any mirror transformation). Such a chiral susceptibility arises in the continuity equation of the t-J model or in presence of the direct exchange interaction [81].

The outline of the paper is as follows: In section 5.2 we give a very brief introduction to response theory and define all necessary two- and three-particle quantities as well as the relationships between them and the response functions. Section 5.3 describes the models we use in our calculations and why we chose them. The numerical results are then presented and analyzed in section 5.4. Finally, in sections 5.5 and 5.6 we give a conclusion and outlook.

5.2. Theory

In general, response theory describes the relation between cause and effect. For our purposes, this boils down to quantifying how the expectation value of an arbitrary, bosonic operator $\langle \hat{A}_i \rangle$ depends on some external "force" F_j. As shown in detail in section 2.8, this can be studied by expanding $\langle \hat{A}_i \rangle$ in a functional Taylor series:

$$\begin{aligned}\langle \hat{A}_i(\tau) \rangle_{\mathbf{F}} = \langle \hat{A}_i(\tau) \rangle_{\mathbf{F}=0} \\ + \sum_j \int_0^\beta \mathrm{d}\tau' F_j(\tau') \chi^{(1)}_{ji}(\tau', \tau) \\ + \frac{1}{2} \sum_{jk} \int_0^\beta \int_0^\beta \mathrm{d}\tau' \, \mathrm{d}\tau'' F_j(\tau') F_k(\tau'') \chi^{(2)}_{jki}(\tau', \tau'', \tau) \\ + \ldots\end{aligned} \tag{5.1}$$

Here, we express everything in imaginary time τ which runs from zero to $\beta = 1/T$, the inverse temperature. We call the expansion coefficients $\chi^{(1)}$ and $\chi^{(2)}$ the first-order or linear, and second-order or nonlinear response function, respectively. They are simply

functional derivatives of $\langle \hat{A}_i \rangle$ with respect to F_j and according to eqs. (2.53) and (2.54) read

$$\begin{aligned} \chi^{(1)}_{ij}(\tau,\tau') &= \left(\frac{\delta}{\delta F_i(\tau)} \langle \hat{A}_j(\tau') \rangle \right)_{\mathbf{F}=0} \\ &= \langle \mathrm{T}\, \hat{A}_i(\tau) \hat{A}_j(\tau') \rangle - \langle \hat{A}_i \rangle \langle \hat{A}_j \rangle, \end{aligned} \tag{5.2}$$

for the first order, and

$$\chi^{(2)}_{ijk}(\tau,\tau',\tau'') = \left(\frac{\delta^2}{\delta F_i(\tau)\, \delta F_j(\tau')} \langle \hat{A}_k(\tau'') \rangle \right)_{\mathbf{F}=0} \tag{5.3}$$

$$\begin{aligned} &= \langle \mathrm{T}\, \hat{A}_i(\tau) \hat{A}_j(\tau') \hat{A}_k(\tau'') \rangle \\ &\quad - \langle \hat{A}_i \rangle \chi_{jk}(\tau',\tau'') - \langle \hat{A}_j \rangle \chi_{ik}(\tau,\tau'') - \langle \hat{A}_k \rangle \chi_{ij}(\tau,\tau') \\ &\quad - \langle \hat{A}_i \rangle \langle \hat{A}_j \rangle \langle \hat{A}_k \rangle. \end{aligned} \tag{5.4}$$

for the second order. Here, T is the time-ordering operator and $\hat{A}_i$ are the bosonic operators that the external fields F_i couple to, i.e., the Hamiltonian contains a perturbation term of the form $-\sum_i \hat{A}_i F_i$. If not indicated otherwise the expectation values are computed with respect to the unperturbed Hamiltonian. From now on we also drop the superscript denoting the order of the response function whenever the (number of) arguments allow to infer it.

In Matsubara space the linear response function reads

$$\begin{aligned} \chi^{\omega}_{ij} &= \int_0^\beta \chi_{ij}(\tau) \mathrm{e}^{\mathrm{i}\omega\tau}\, \mathrm{d}\tau \\ &= \langle \mathrm{T}\, \hat{A}_i(\tau) \hat{A}_j \rangle^{\omega} - \delta^{\omega 0} \beta \langle \hat{A}_i \rangle \langle \hat{A}_j \rangle, \end{aligned} \tag{5.5}$$

while the nonlinear response function is given by

$$\begin{aligned} \chi^{\omega_1\omega_2}_{ijk} &= \int_0^\beta \int_0^\beta \chi_{ijk}(\tau_1,\tau_2) \mathrm{e}^{\mathrm{i}(\omega_1\tau_1 + \omega_2\tau_2)}\, \mathrm{d}\tau_1\, \mathrm{d}\tau_2 \\ &= \langle \mathrm{T}\, \hat{A}_i(\tau_1) \hat{A}_j(\tau_2) \hat{A}_k \rangle^{\omega_1\omega_2} \\ &\quad - \delta^{\omega_1 0} \beta \langle \hat{A}_i \rangle \chi^{\omega_2}_{jk} - \delta^{\omega_2 0} \beta \langle \hat{A}_j \rangle \chi^{\omega_3}_{ik} - \delta^{\omega_3 0} \beta \langle \hat{A}_k \rangle \chi^{\omega_1}_{ij} \\ &\quad - \delta^{\omega_1 0} \delta^{\omega_2 0} \beta^2 \langle \hat{A}_i \rangle \langle \hat{A}_j \rangle \langle \hat{A}_k \rangle. \end{aligned} \tag{5.6}$$

Here, we use time-translation invariance to effectively get rid of one imaginary time argument, $\omega_3 = -\omega_1 - \omega_2$, and the frequency superscript for the expectation values indicates the Fourier transform of the corresponding imaginary time expressions defined in eqs. (5.2) and (5.4).

We see that the response functions are nothing but two- and three-particle correlators minus their disconnected terms.

So far everything is formulated with general, bosonic operators $\hat{A}_i$. For the rest of this paper we are, however, only interested in the cases where those are density and spin operators:

$$\hat{n} = \hat{n}_\uparrow + \hat{n}_\downarrow = \hat{c}_\uparrow^\dagger \hat{c}_\uparrow + \hat{c}_\downarrow^\dagger \hat{c}_\downarrow \tag{5.7}$$

$$\hat{\sigma}_i = \begin{pmatrix} \hat{c}_\uparrow^\dagger & \hat{c}_\downarrow^\dagger \end{pmatrix} \underline{\underline{\sigma}}_i \begin{pmatrix} \hat{c}_\uparrow \\ \hat{c}_\downarrow \end{pmatrix} \tag{5.8}$$

with fermionic creation and annihilation operators $\hat{c}^\dagger$ and $\hat{c}$ as well as Pauli matrices $\underline{\underline{\sigma}}_i$. In the Hamiltonian they couple as $\epsilon\hat{n}$, and $-\mathbf{h}\hat{\boldsymbol{\sigma}}$ to (the change of) the one-particle energy ϵ and magnetic field $\mathbf{h}$.

Let us further introduce the following compact notation for the full, bosonic, two-particle, density and spin correlators

$$X_{\sigma_1\dots\sigma_4}(\tau) = \langle \mathrm{T}\, \hat{c}_{\sigma_1}^\dagger(\tau^+)\hat{c}_{\sigma_2}(\tau)\hat{c}_{\sigma_3}^\dagger(0^+)\hat{c}_{\sigma_4}(0)\rangle, \tag{5.9}$$

$$X_{\alpha\beta} = \sum_{\sigma_1\dots\sigma_4} s_\alpha^{\sigma_1\sigma_2}\, s_\beta^{\sigma_3\sigma_4}\, X_{\sigma_1\dots\sigma_4}, \tag{5.10}$$

$$\underline{\underline{s}}_\alpha = \begin{cases} \mathbb{1}, & \alpha = n, \\ \underline{\underline{\sigma}}_\alpha, & \alpha \in \{x, y, z\}, \end{cases} \tag{5.11}$$

where $\tau^+ = \lim_{\varepsilon\to 0} \tau + \varepsilon$ and $0^+ = \lim_{\varepsilon\to 0} 0 + \varepsilon$. Analogously, on the three-particle level we define

$$X_{\sigma_1\dots\sigma_6}(\tau_1, \tau_2) = \langle \mathrm{T}\, \hat{c}_{\sigma_1}^\dagger(\tau_1^+)\hat{c}_{\sigma_2}(\tau_1)\hat{c}_{\sigma_3}^\dagger(\tau_2^+)\hat{c}_{\sigma_4}(\tau_2)\hat{c}_{\sigma_5}^\dagger(0^+)\hat{c}_{\sigma_6}(0)\rangle, \tag{5.12}$$

$$X_{\alpha\beta\gamma} = \sum_{\sigma_1\dots\sigma_6} s_\alpha^{\sigma_1\sigma_2}\, s_\beta^{\sigma_3\sigma_4}\, s_\gamma^{\sigma_5\sigma_6}\, X_{\sigma_1\dots\sigma_6}. \tag{5.13}$$

In this notation the response functions read

$$\chi_{\alpha\beta} = \mathrm{conn}\, X_{\alpha\beta}, \tag{5.14}$$

$$\chi_{\alpha\beta\gamma} = \mathrm{conn}\, X_{\alpha\beta\gamma}, \tag{5.15}$$

where conn denotes only fully connected terms.

On the two-particle level, only the response of the density to changes of the one-particle energy, χ_d, and the response of the magnetization to changes of the magnetic field in

the same direction, χ_m, do not vanish:[a]

$$\chi_d(\tau) = -\frac{\delta\langle\hat{n}\rangle}{\delta\epsilon(\tau)} = \chi_{nn}(\tau), \tag{5.16}$$

$$\chi_m(\tau) = \frac{\delta\langle\hat{\sigma}_i\rangle}{\delta h_i(\tau)} = \chi_{ii}(\tau), \text{ with } i = x, y, z. \tag{5.17}$$

Using eqs. (5.2), (5.9) and (5.10) we can derive well-known relations for the linear response functions:

$$\chi_{nn}(\tau) = X_{nn}(\tau) - \langle\hat{n}\rangle^2 = 2(\chi_{\uparrow\uparrow}(\tau) + \chi_{\uparrow\downarrow}(\tau)), \tag{5.18}$$

$$\chi_{zz}(\tau) = X_{zz}(\tau) = 2(\chi_{\uparrow\uparrow}(\tau) - \chi_{\uparrow\downarrow}(\tau)), \tag{5.19}$$

where the spin susceptibilities are $\chi_{\sigma\sigma'} = -\delta\langle\hat{n}_{\sigma'}\rangle/\delta\epsilon_\sigma$ with ϵ_σ denoting the (change of) the one-particle energy for spin σ only, and we assume SU(2) symmetry.

On the three-particle level, only the following response functions do not vanish:[b]

$$\chi_{nnn}(\tau_1, \tau_2) = \frac{\delta}{\delta\epsilon(\tau_1)}\frac{\delta\langle\hat{n}\rangle}{\delta\epsilon(\tau_2)} = \frac{\delta\chi_d(\tau_2)}{\delta\epsilon(\tau_1)}, \tag{5.20}$$

$$\begin{aligned}\chi_{nzz}(\tau_1, \tau_2) &= \chi_{nxx}(\tau_1, \tau_2) = \chi_{nyy}(\tau_1, \tau_2) \\ &= -\frac{\delta}{\delta\epsilon(\tau_1)}\frac{\delta\langle\hat{\sigma}_i\rangle}{\delta h_i(\tau_2)} = -\frac{\delta\chi_m(\tau_2)}{\delta\epsilon(\tau_1)},\end{aligned} \tag{5.21}$$

$$\chi_{xyz}(\tau_1, \tau_2) = \frac{\delta}{\delta h_x(\tau_1)}\frac{\delta\langle\hat{\sigma}_z\rangle}{\delta h_y(\tau_2)}. \tag{5.22}$$

We call them the second-order density, density-magnetic, and chiral response functions, respectively. In appendix A.1 we derive relations similar to eqs. (5.18) and (5.19) for them. They show, e.g., that X_{xyz} contains no disconnected terms that need to be subtracted – just like X_{zz} on the two-particle level. Furthermore, in the special case of half-filling, i.e., $n_\sigma = 1/2 = 1 - n_\sigma$, we show that χ_{nnn} and χ_{nzz} vanish.

Remembering the usual definition of an n-particle Green's function,

$$G^n_{\sigma_1\sigma_2\ldots\sigma_{2n}}(\tau_1, \tau_2, \ldots, \tau_{2n}) = (-1)^n\langle \mathrm{T}\, \hat{c}_{\sigma_1}(\tau_1)\hat{c}^\dagger_{\sigma_2}(\tau_2)\ldots\hat{c}^\dagger_{\sigma_{2n}}(\tau_{2n})\rangle, \tag{5.23}$$

and looking at eqs. (5.9) to (5.15) we see that the response functions are basically given by the connected parts of equal time Green's functions. We only have to take care of the different order of creation and annihilation operators

[a] The extra minus in eq. (5.16) is necessary because the density couples with $+\epsilon\hat{n}$, and a derivative with respect to ϵ brings down $-\hat{n}$ [see section 2.8], but according to eq. (5.14) we want $\chi_d = \chi_{nn} = +\mathrm{conn}\langle \mathrm{T}\,\hat{n}\hat{n}\rangle$.

[b] The extra minus in eq. (5.21) is there for the same reason as in eq. (5.16)

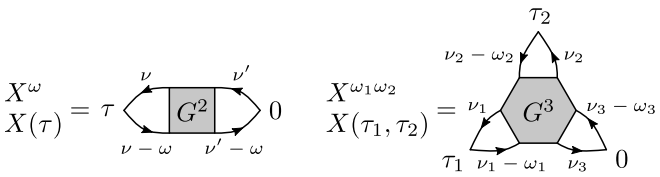

Figure 5.1.: Diagrammatic representation of the full two- and three-particle correlators. For brevity the time and frequency labels are given in the same diagrams.

$$X_{\sigma_1\dots\sigma_4}(\tau) = G^2_{\sigma_2\sigma_1\sigma_4\sigma_3}(\tau, \tau^+, 0, 0^+), \tag{5.24}$$

$$X_{\sigma_1\dots\sigma_6}(\tau_1, \tau_2) = G^3_{\sigma_2\sigma_1\sigma_6\sigma_5\sigma_4\sigma_3}(\tau_1, \tau_1^+, 0, 0^+, \tau_2, \tau_2^+). \tag{5.25}$$

Let us finally also define the Fourier transform,

$$X^{\omega_1\omega_2}_{\sigma_1\dots\sigma_6} = \int_0^\beta \int_0^\beta X_{\sigma_1\dots\sigma_6}(\tau_1, \tau_2) \mathrm{e}^{\mathrm{i}\omega_1\tau_1 + \mathrm{i}\omega_2\tau_2} \,\mathrm{d}\tau_1 \,\mathrm{d}\tau_2, \tag{5.26}$$

where ω_1 and ω_2 are bosonic Matsubara frequencies.

With this we can give a diagrammatic representation of the correlators and response functions. Figure 5.1 shows the diagrams for the full two- and three-particle correlators with time and frequency labels. A particle–hole notation is chosen for the latter. (See section 4.2 for a detailed look at all 15 frequency notations of the three-particle Green's function.)

To get a diagrammatic representation of the response functions we do a decomposition of the full correlators and therefore Green's functions. For the three-particle case details on this are found in section 4.4. The diagrammatic results are shown in fig. 5.2. Here we see that the terms in eqs. (5.2) and (5.4) to (5.6), which we already called disconnected, are in fact represented by disjoint diagrams. Figure 5.2 further decomposes the connected diagrams of $\chi^{(1)}$ and $\chi^{(2)}$ and introduces the bare or bubble terms χ_0, which only contain Green's functions, the first-order terms $\chi_1^{(2)}$, which are three-particle diagrams with a single two-particle vertex F, and χ_{vertex}, which contains corrections from the "largest" possible vertex. When studying the results in section 5.4 we are especially interested in $\chi^{(2)}_{\text{vertex}}$ since it contains diagrams where all three particles interact with each other.

5.3. Models

For simplicity, we mainly employ the AIM, but some results for the HM as well as for the atomic limit, which is the same for both, are also shown. The results for these three cases are presented in the corresponding subsections of section 5.4.

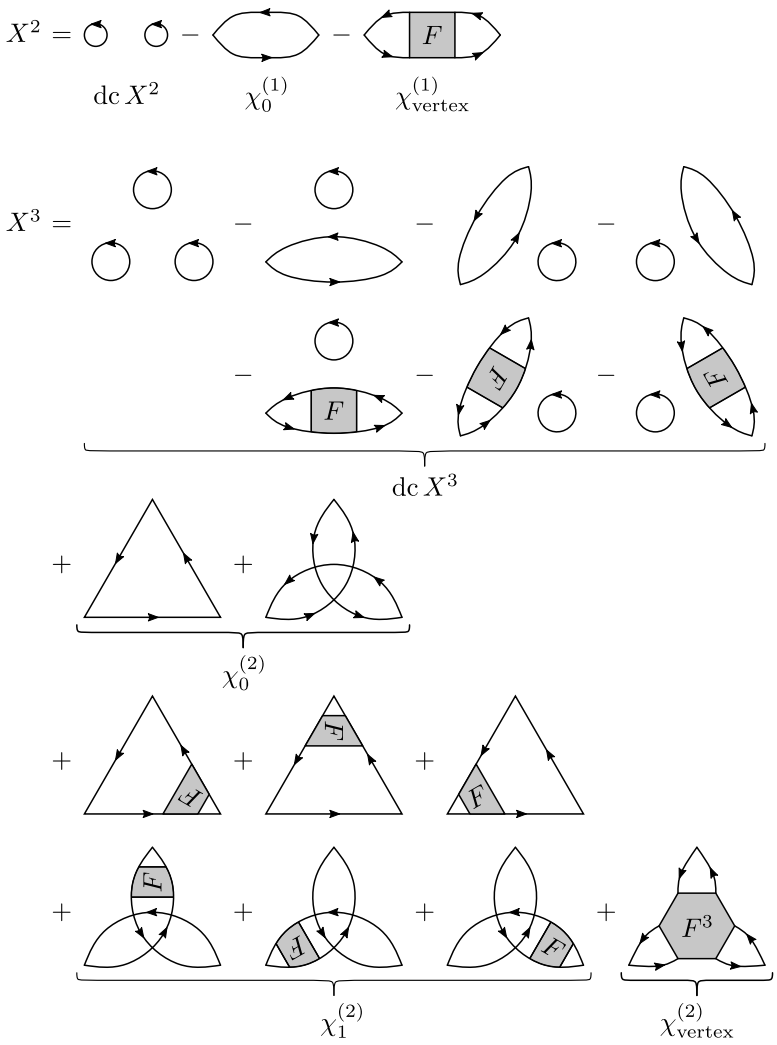

Figure 5.2.: Diagrammatic representation of the decomposition of the full, two- and three-particle correlators X into disconnected terms $\mathrm{dc}\, X$, bare or bubble terms χ_0, first-order terms χ_1 and full vertex terms χ_{vertex}. Time and frequency labels are omitted to avoid clutter. They can easily be inferred from fig. 5.1.

5.3.1. Atomic limit

As a simple toy model, we consider the atomic limit with Hamiltonian $\hat{H}_{\mathrm{AL}} = \epsilon(\hat{n}_\uparrow + \hat{n}_\downarrow) - h(\hat{n}_\uparrow - \hat{n}_\downarrow) + U\hat{n}_\uparrow\hat{n}_\downarrow$ where $\epsilon = -U/2$ and h is a magnetic field. This model can be solved exactly using the Lehmann representation.

5.3.2. Anderson impurity model

Section 3.1 already briefly introduces the Anderson impurity model (AIM). Its Hamiltonian is given in eq. (3.1). In this chapter we use (i) a single bath site with energy $\epsilon_{k=1} = \epsilon_1$ and (ii) a constant density of states (DOS).

The former is chosen because it can easily be solved with exact diagonalization (ED) and therefore serves as a test for the implementation of the three-particle calculations. The latter is used for most other results because, while still relatively simple and therefore fast to solve on modern computers, it already shows effects of strong electronic correlation. The low computational complexity of the model is important because of two things: First, we expect that the search for regions where three-particle effects are relevant involves sampling a potentially large amount of points in the phase diagram. Second, we solve the AIM by means of a quantum Monte Carlo (QMC) solver. Once the interesting points are found, getting accurate, low-noise results for $\chi^{(2)}$ can require a lot of QMC samples since the disconnected parts that have to be subtracted first (see section 5.2) potentially make up most of the correlation function.

5.3.3. Hubbard model

The Hubbard model (HM) is already briefly introduced in section 3.2 and its Hamiltonian given in eq. (3.3).

Since, the HM cannot be solved on a square lattice, also not numerically, except for very small clusters, we employ DMFT [35–37, 56] for an approximate solution. DMFT actually maps the HM onto a self-consistent solution of the AIM. The susceptibilities that we calculate here are local impurity susceptibilities only. This means that these susceptibilities are actually also obtained from the AIM, but now at DMFT self-consistency. They differ from the lattice susceptibilities, also the local ones, since the applied fields can also affect the DMFT bath of the auxiliary AIM. This effect is not taken into account here.

5.4. Results

The numerical results in this section are obtained with w2dynamics [82], a continuous-time QMC solver using the hybridization expansion [45]. Only for the AIM with

one bath site we also employ ED. Furthermore, let us mention that numerical renormalization group has been successfully employed recently for calculating multipoint correlators of the AIM [83]. Post-processing of the QMC results is done with the Python package w2diag [84] written to, among other things, implement the equations in section 5.2 and compute the first- and second-order susceptibilities $\chi^{(1)}$ and $\chi^{(2)}$, involving two- and three-particle correlators, respectively.

The results for the atomic limit are computed analytically through the Lehmann representation.

A dataset containing all numerical data and plot scripts used to generate the figures in this section is publicly available on the TU Wien Research Data repository [85]. The dataset also contains auxiliary data files, parameter files and submission scripts for better reproducibility.

5.4.1. Atomic limit

In the atomic limit we only have four states: empty site, single occupation with spin σ $\uparrow$ or $\downarrow$, and double occupation with energies zero, $\epsilon \mp h$, and $2\epsilon + U$, respectively. We calculate the three-particle correlators of the atomic limit, as defined in eqs. (5.12), (5.13) and (5.26), employing the Lehmann representation in appendix A.2. As shown in section 4.3, with SU(2) symmetry and swapping relations we only obtain three independent flavor combinations, $\alpha\beta\gamma = nnn, nzz, xyz$, for the second-order (three-operator) susceptibility. Moreover, the first two flavor combinations correspond, in the atomic limit, to conserved and mutually commuting operators. As a result, these three-particle correlators are purely thermal: $X^{\omega_1\omega_2}_{nnn} = X_{nnn}\delta^{\omega_1 0}\delta^{\omega_2 0}$, $X^{\omega_1\omega_2}_{nzz} = X_{nzz}\delta^{\omega_1 0}\delta^{\omega_2 0}$. Only $X^{\omega_1\omega_2}_{xyz}$ has a frequency structure.

Let us first consider the noninteracting case ($U = 0$) at half-filling ($\epsilon = 0$), without a magnetic field ($h = 0$). We evaluate the three-particle correlator using Wick's theorem:

$$\begin{aligned} X^{\omega_1\omega_2}_{\sigma_1\cdots\sigma_6} = {} & \beta^2\langle\hat{n}_{\sigma_1}\rangle\langle\hat{n}_{\sigma_2}\rangle\langle\hat{n}_{\sigma_3}\rangle\,\delta_{\sigma_1\sigma_1'}\delta_{\sigma_2\sigma_2'}\delta_{\sigma_3\sigma_3'}\delta^{\omega_1 0}\delta^{\omega_2 0} \\ & - \beta\langle\hat{n}_{\sigma_1}\rangle\frac{1}{\beta}\sum_\nu G^\nu_{\sigma_2}G^{\nu+\omega}_{\sigma_3}\delta_{\sigma_1\sigma_1'}\delta_{\sigma_2\sigma_3'}\delta_{\sigma_3\sigma_2'}\delta^{\omega_1 0} \\ & - \beta\langle\hat{n}_{\sigma_2}\rangle\frac{1}{\beta}\sum_\nu G^\nu_{\sigma_1}G^{\nu+\omega}_{\sigma_3}\delta_{\sigma_1\sigma_3'}\delta_{\sigma_2\sigma_2'}\delta_{\sigma_3\sigma_1'}\delta^{\omega_2 0} \\ & - \beta\langle\hat{n}_{\sigma_3}\rangle\frac{1}{\beta}\sum_\nu G^\nu_{\sigma_1}G^{\nu+\omega}_{\sigma_2}\delta_{\sigma_1\sigma_2'}\delta_{\sigma_2\sigma_1'}\delta_{\sigma_3\sigma_3'}\delta^{\omega_1,-\omega_2} \\ & + \frac{1}{\beta}\sum_\nu G^\nu_{\sigma_1}G^{\nu+\omega_1}_{\sigma_2}G^{\nu+\omega_1+\omega_2}_{\sigma_3} \\ & + \frac{1}{\beta}\sum_\nu G^\nu_{\sigma_2}G^{\nu+\omega_2}_{\sigma_1}G^{\nu+\omega_1+\omega_2}_{\sigma_3}. \end{aligned} \tag{5.27}$$

The first term with three densities n corresponds to the fully disconnected, first diagram for X^3 in fig. 5.2. The terms two to four have one density and a bare bubble susceptibility [for $U = 0$: $\chi_d = \chi_m = -\frac{1}{\beta}\sum_\nu G^\nu G^{\nu+\omega}$], as the next three diagrams for X^3 in fig. 5.2. All of these terms are disconnected and do not contribute to the second-order, three-particle susceptibility.

The last two terms in eq. (5.27) are the bare bubble second-order susceptibility $\chi_0^{(2)}$, represented diagrammatically in the second line of diagrams for X^3 in fig. 5.2 [cf. eqs. (5.20) to (5.22)]. This connected part contains the essential three-particle information. While for $U = 0$ it is given through the (two) bare bubble diagrams, vertex corrections become important for $U \neq 0$. Namely, there are corrections with the two-particle vertex F connecting two Green's function lines as well as more complicated three-particle vertex corrections with F^3. The latter connects all three Green's function lines of the bubble through interactions.

As a technical note: In eq. (5.27) the connected part appears next to the disconnected term of order β^2. Therefore, a stochastic measurement of the three-particle susceptibility has a less favorable signal-to-noise ratio at low temperatures than the two-particle one, whose disconnected term is only of order β.

The upper panel of fig. 5.3 shows the density $\langle\hat{n}\rangle$ of the noninteracting system as a function of the energy ϵ ($\beta = 5$), together with its first and second derivatives with respect to ϵ. The latter is computed from eq. (5.6), but with partial instead of functional derivatives and therefore static correlators, yielding

$$\frac{\partial^2\langle\hat{n}\rangle}{\partial\epsilon^2} = X^{00}_{nnn} + 3\beta\langle\hat{n}\rangle\frac{\partial\langle\hat{n}\rangle}{\partial\epsilon} - \beta^2\langle\hat{n}\rangle\langle\hat{n}\rangle\langle\hat{n}\rangle, \tag{5.28}$$

where $\partial\langle\hat{n}\rangle/\partial\epsilon = -X^0_{nn} + \beta\langle\hat{n}\rangle\langle\hat{n}\rangle$ [cf. eq. (5.16)] and $\langle\hat{n}\rangle$ are computed in the usual way, see, e.g., ref. [43]. We verified that eq. (5.28) coincides with the analytical and numerical second derivative of $\langle\hat{n}\rangle$. Also drawn is the three-particle bubble (dashed), which coincides exactly with the second derivative, as expected ($U = 0$). For negative (positive) ϵ, double occupations (empty sites) are favorable. Hence, the density $\langle\hat{n}\rangle$ shows a crossover of width $1/\beta$, and the other quantities follow as derivatives.

Next, we turn on the interaction ($U = 1$), which lifts the degeneracy of the empty, singly, and doubly occupied states at $\epsilon = 0$. As a result, the derivatives of $\langle\hat{n}\rangle$ in the lower panel of fig. 5.3 acquire additional minima and maxima. It is interesting to compare $\partial^2\langle\hat{n}\rangle/\partial\epsilon^2$ to the three-particle bubble, which lacks vertex corrections. For large dopings the two curves coincide, which can be considered as a perturbative regime where interaction effects are small. However, in the correlated regime, near half-filling the three-particle bubble fails qualitatively. In particular, it is unable to describe the curvature of $\langle\hat{n}\rangle$ for ϵ in between the Hubbard bands.

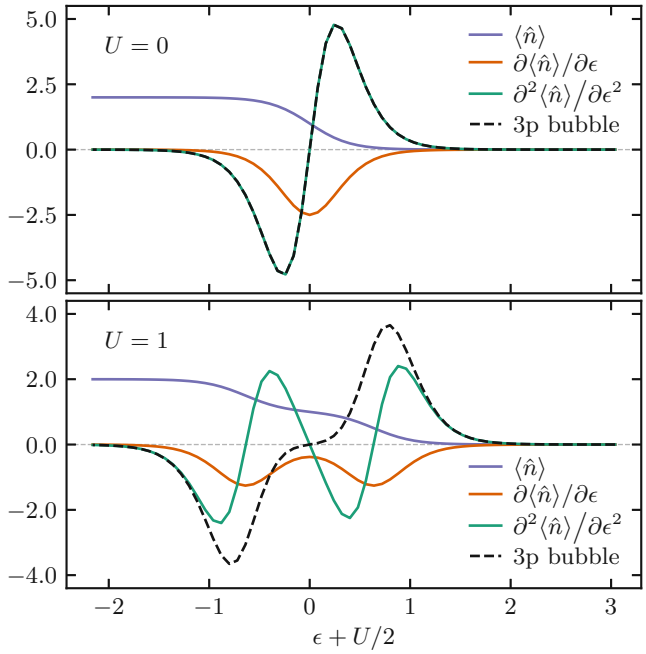

Figure 5.3.: Density $\langle\hat{n}\rangle$ as a function of the energy ϵ (purple) in the atomic limit ($\beta = 5$, $h = 0$). Orange and green curves show the first and second derivative, respectively; a black dashed line the three-particle bubble. Top panel: Noninteracting limit. Bottom panel: $U = 1$.

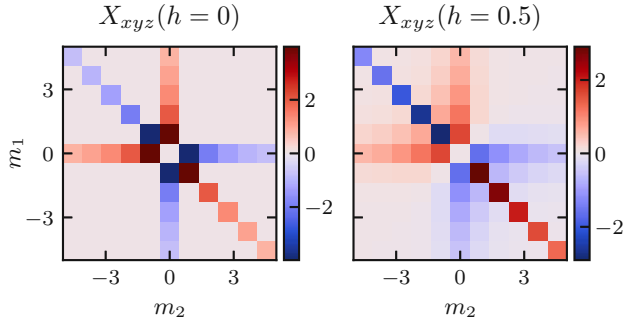

Figure 5.4.: Full three-particle correlator with flavors x, y, z drawn as a function of the two indices $m_{i=1,2}$ of the bosonic Matsubara frequencies $\omega_i = m_i 2\pi T$; $U = \epsilon = 0, \beta = 5$. In the atomic limit only this flavor combination retains a frequency structure due to noncommutativity of the spin operators. Left: no magnetic field. Right: magnetic field in z-direction, $h = 0.5$.

Finally, we consider the only three-particle correlation function that retains a nontrivial frequency structure in the atomic limit: the chiral susceptibility $X_{xyz}^{\omega_1\omega_2} = \chi_{xyz}^{\omega_1\omega_2}$. The left panel of fig. 5.4 shows this function for $U = 0$, $\epsilon = 0$, $h = 0$, $\beta = 5$. This picture does not change qualitatively when U is turned on (not shown), which underlines that the frequency structure of X_{xyz} is a result of the noncommutativity of the spin operators among each other, rather than due to a specific interaction regime. Notice also that the function is singular, that is, it vanishes exactly away from the cross and diagonal structures, since each component of the spin operator is conserved. This property does not persist for a finite magnetic field $h = 0.5$ in the z direction (right panel), which softens the cross structure, since it does not commute with the x and y components of the spin operator.

5.4.2. AIM with one bath site

To test the correctness of the implementation of the second-order response functions in w2diag the results are compared against solutions of an AIM with a single bath site obtained via ED. More precisely the density n and the linear, magnetic response function χ_m are computed with ED and then numerically differentiated. This yields the right-hand side of the following two formulas

$$\chi_{nnn}^{00} = \frac{\partial^2}{\partial\epsilon^2}\langle\hat{n}\rangle, \tag{5.29}$$

$$\chi_{nzz}^{00} = -\frac{\partial}{\partial\epsilon}\chi_m, \tag{5.30}$$

which are basically eqs. (5.20) and (5.21) but with partial instead of functional derivatives for denoting static response functions χ_{nnn}^{00} and χ_{nzz}^{00}. The left-hand side, is computed with w2diag from QMC results obtained with w2dynamcis.

The results for $U = 1$, $\beta = 20$, $V = 0.2$ and $\epsilon_1 = 0.25$ are shown as a function of ϵ in fig. 5.5; those for $V = 0.05$ and $\epsilon_1 = 0$ with the same U and β are plotted in fig. 5.6. We see that the agreement between stochastic and exact results is very good except for χ_{nnn} in fig. 5.5 where the large noise prevents precise statements.

This trend of higher noise in the data for χ_{nnn} is something we observe in almost every computation, and can be explained as follows: First, we measure the full three-particle correlators with similar relative noise, but since at least the static component X^{00} is usually larger in the nnn channel than in the nzz channel, the absolute error is also larger there. Second, and more importantly, when looking at eq. (5.6) we see that for χ_{nnn} we have to subtract all four disconnected terms from X_{nnn}, while for χ_{nzz} three of the four terms vanish because $\langle\hat{\sigma}_z\rangle = 0$. Therefore, the magnitude of χ_{nnn}^{00} is often smaller than that of χ_{nzz}^{00}. Together this explains why the results for χ_{nnn}^{00} can have significantly higher relative noise than those for χ_{nzz}^{00}. Figure 5.7 in the next subsection shows this most dramatically.

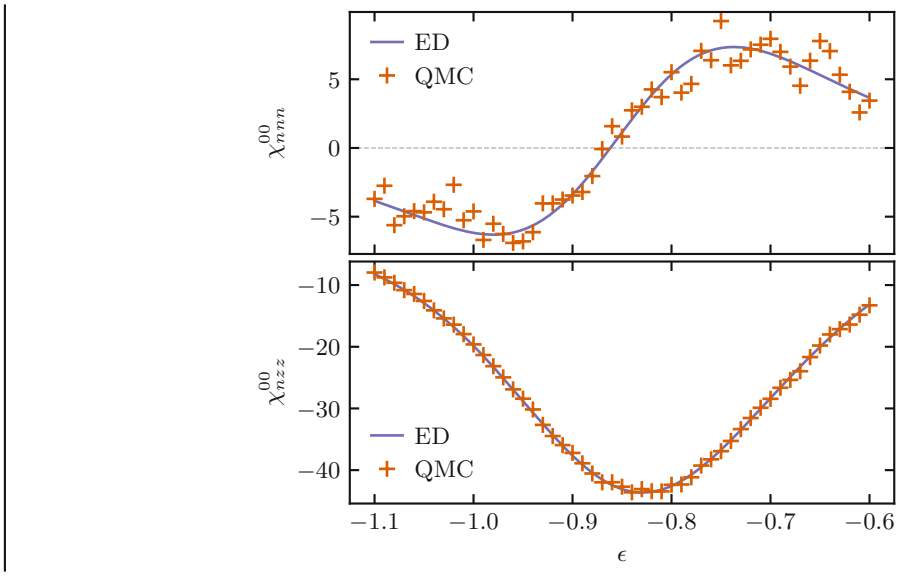

Figure 5.5.: Comparison of exact (ED) and stochastic (QMC) results for the AIM at $U = 1$, $\beta = 20$, hybridizing with $V = 0.2$ to a single bath site with energy $\epsilon_1 = 0.25$. The top plot shows the static, second-order, density response function χ^{00}_{nnn}, while the bottom one shows the static, second-order, density-magnetic response function χ^{00}_{nzz}.

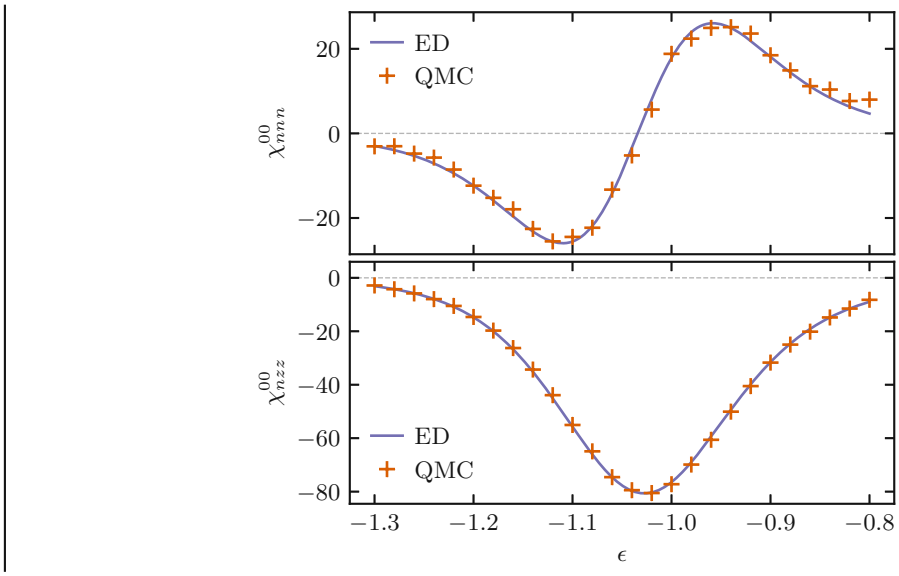

Figure 5.6.: Comparison of exact (ED) and stochastic (QMC) results for the AIM with a single bath site. Same as fig. 5.5, but now at $U = 1$, $\beta = 20$, $V = 0.05$ and $\epsilon_1 = 0$.

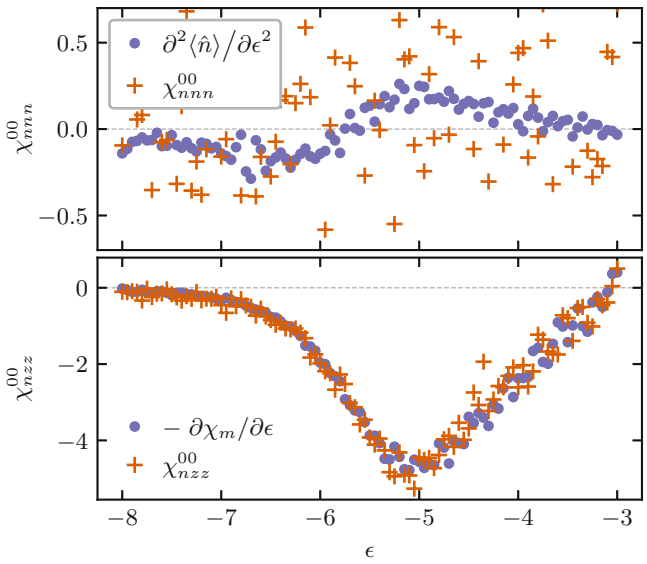

Figure 5.7.: Scan of $\partial^2\langle\hat{n}\rangle/\partial\epsilon^2$, $-\partial\chi_m/\partial\epsilon$, χ_{nnn} and χ_{nzz} vs. ϵ for an AIM with constant DOS at $D = 10$, $U = 6$, $V = 2$ and $\beta = 18$. The noise of χ_{nnn} is even larger than depicted. Its data points are actually outside the plotted region and between -1.5 and 1.5. However, with that range on the y-axis the extrema of $\partial^2\langle\hat{n}\rangle/\partial\epsilon^2$ would hardly be noticeable.

5.4.3. AIM with constant DOS

To find an area with potentially large, second-order effects we do calculations at two to five times the Kondo temperature and make an ϵ-scan starting from $-U/2$ going to smaller values. The idea behind this is to find larger nonlinear dynamics; and, going away from particle-hole symmetry $\epsilon = -U/2$ reduces the Kondo temperature so that the derivative with respect to ϵ should be sizable.

The chosen parameters are $D = 10$, $U = 6$, $V = 2$ and $\beta = 18$. They satisfy $D > U \gtrsim V$ so according to [25, p. 165ff] we can estimate the Kondo temperature to be $1/T_K = \beta_K \approx 64$ which means that $\beta/\beta_K \approx 3.6$.

Figure 5.7 shows the second derivative of the density $\partial^2\langle\hat{n}\rangle/\partial\epsilon^2$, the first derivative of the linear, magnetic response function $\partial\chi_m/\partial\epsilon$ as well as the static, second-order, density and density-magnetic response functions χ^{00}_{nnn} and χ^{00}_{nzz} plotted over ϵ. This time χ^{00}_{nnn} is so noisy that no useful information can be extracted (see the discussion at the end of section 5.4.2 for an explanation). Nevertheless, we clearly observe the largest, second-order effects around $\epsilon = -5$ and also $\epsilon = -6.6$, so we choose those points for closer, frequency-resolved investigation.

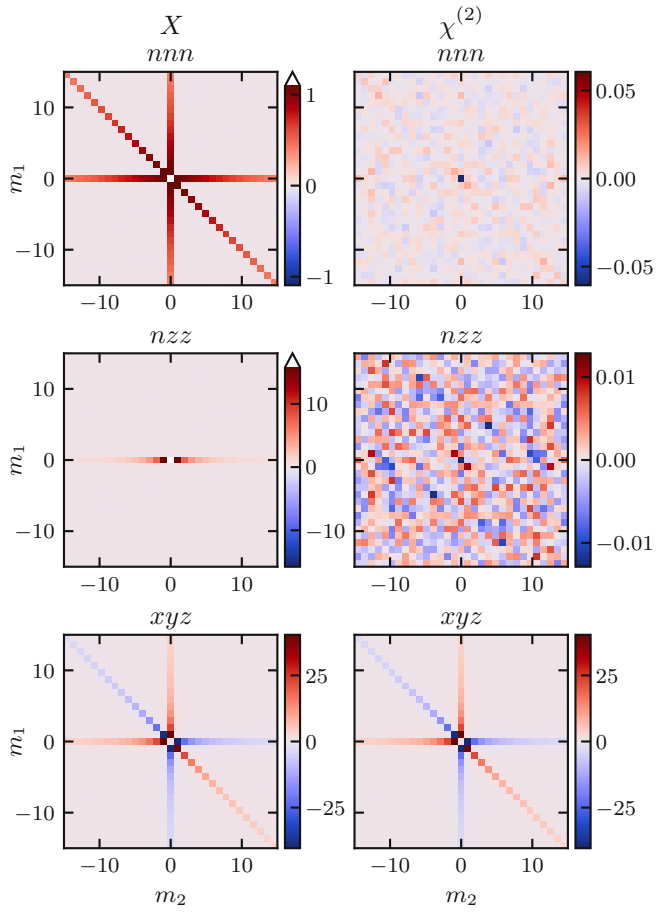

Figure 5.8.: Full correlation functions X (left column) and second-order response functions $\chi^{(2)}$ (right column) vs. the two indices $m_{i=1,2}$ of the bosonic Matsubara frequencies $\omega_i = m_i 2\pi T$ in the density (nnn; top row), density-magnetic (nzz; center row), and chiral (xyz; bottom row) channel for an AIM with constant DOS at $D = 10$, $U = 6$, $V = 2$, $\beta = 18$ and half-filling, i.e., $\epsilon = -3$ and $n = 1$. The color bars for X_{nnn} and X_{nzz} exclude the largest value at the center because it would dominate the plots. These values are $X^{00}_{nnn} \approx 327$ and $X^{00}_{nzz} \approx 171$.

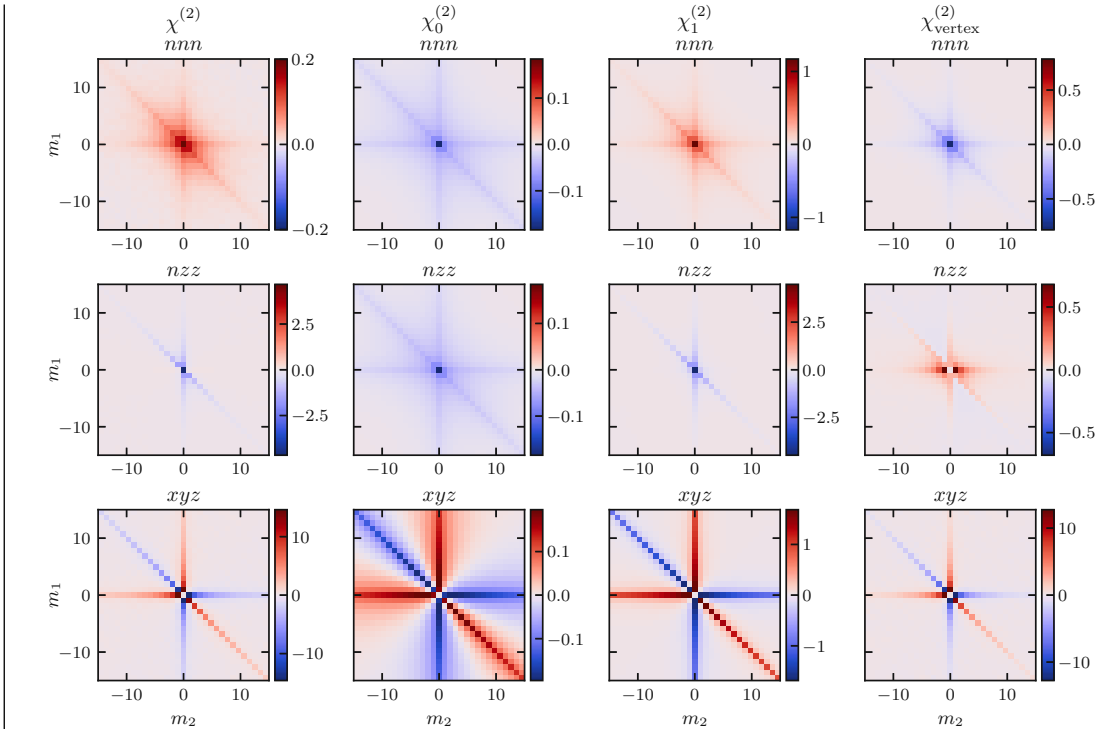

Figure 5.9.: Second-order response functions $\chi^{(2)}$ and their decomposition into the bubble terms $\chi^{(2)}_0$, first-order terms $\chi^{(2)}_1$ and vertex terms $\chi^{(2)}_{\text{vertex}}$ in the density (nnn), density-magnetic (nzz), and chiral (xyz) channel for an AIM with constant DOS at $D = 10$, $U = 6$, $V = 2$, $\beta = 18$ and $\epsilon = -5$ corresponding to $n \approx 1.22$.

First, however, we take a look at half-filling, i.e., $\epsilon = -U/2 = -3$ and $n = 1$. Figure 5.8 shows the full correlation functions $X^{\omega_1\omega_2}$ (left column) and the second-order response functions $\chi^{\omega_1\omega_2}$ (right column) in the density, density-magnetic, and chiral channel. The color bars for X_{nnn} and X_{nzz} exclude the largest value at the center because it would dominate the plots with values of $X^{00}_{nnn} \approx 327$ and $X^{00}_{nzz} \approx 171$. As expected from the discussion at the end of section 5.2 we see that, in this case, χ_{nnn} and χ_{nzz} vanish (the higher absolute noise at the center of χ_{nnn} comes from the large value of X^{00}_{nnn}). There is also no difference between the full correlator and the connected parts in the chiral channel. X_{nnn} and X_{nzz} clearly show the structure of the disconnected parts with their $\delta^{\omega_i 0}$ terms [see eqs. (A.8) to (A.11)]. The latter are also responsible for the large values at $\omega_1 = \omega_2 = 0$ that are clipped from the color bar. Although there are no disconnected terms for X_{xyz}, it shows similar "cross"-like but antisymmetric structures. Additionally, note that in fig. 5.8 we see the following order when comparing the magnitudes of the nonstatic parts: $X_{xyz} > X_{nzz} > X_{nnn}$. For the static components this order is exactly reversed.

As discussed above, the results for the largest, second-order effects in the density and density-magnetic channel are found approximately at $\epsilon = -5$ in Figure 5.7, corresponding to $n \approx 1.22$. They are shown in fig. 5.9 where we plot the full, second-order response function $\chi^{(2)}$, as well as its decomposition into the bubble terms $\chi_0^{(2)}$, first-order terms $\chi_1^{(2)}$, and vertex terms $\chi_{\text{vertex}}^{(2)}$ in all three channels. For the density-like response functions, i.e., χ_{nnn} and χ_{nzz}, even after subtracting the disconnected terms we still see the maximum at the center point and "cross"-like structures along the $\omega_i = 0$ lines. Those features are, however, much less pronounced and more washed out when compared to those of X in fig. 5.8. Since there are generally no disconnected terms in the chiral channel ($\chi_{xyz} = X_{xyz}$), the plot of χ_{xyz} looks almost exactly the same as before. Compared to fig. 5.8, only the magnitude is reduced because of the different doping. When looking at the decomposition, the density-like channels all look rather similar and soft while the features in the chiral channel are much more pronounced and long-ranged. Regardless of that, the bubble terms $\chi_0^{(2)}$ are of similar magnitude for all channels but never a good approximation for the whole second-order response functions. They are too small and in the density channel the bubble even has the wrong sign. The first-order terms $\chi_1^{(2)}$ are larger (sometimes too large) and always have the right sign, but that is still not enough. Across all three channels the corrections from the three-particle vertex $\chi_{\text{vertex}}^{(2)}$ have sizable contributions that cannot be neglected. Especially χ_{xyz} is dominated by these terms. When comparing maximum magnitudes of the second-order response functions, we see the same ordering as for the nonstatic parts of X in the half-filled case: $\chi_{xyz} > \chi_{nzz} > \chi_{nnn}$.

Figure 5.10 shows the same plots as fig. 5.9 but for $\epsilon = -6.6$, corresponding to $n \approx 1.68$, where the second-largest, second-order effects in the density channel are found. We see in all plots that the features are much less pronounced. Especially the plots of the chiral channel are more washed out and, since the magnitude of χ_{xyz} is much lower than when closer to half-filling, noise becomes a problem, particularly for the three-particle vertex corrections. The sign change of χ_{nnn} is expected when looking at fig. 5.7, and means that the bubble now has the correct sign across all channels. In general, we see that at this higher doping the bubble becomes a better approximation while $\chi_1^{(2)}$ and $\chi_{\text{vertex}}^{(2)}$ become smaller.

Finally, we take a look at the asymptotic behavior of the second-order response functions in the limit of large Matsubara frequencies ω. More precisely we look at 1d cuts along $\omega_1 = 0$ and $\omega_2 = \omega$. From the detailed derivation in appendix A.3 we get

$$\chi_{nnn}^{0\omega} \approx -\frac{1}{\omega^2}\frac{\partial\langle H_V\rangle}{\partial\epsilon}, \tag{5.31}$$

$$\chi_{nzz}^{0\omega} \approx -\frac{1}{\omega^2}\frac{\partial\langle H_V\rangle}{\partial\epsilon}, \tag{5.32}$$

$$\chi_{xyz}^{0\omega} \approx -\frac{2}{\omega}\chi_m^0, \tag{5.33}$$

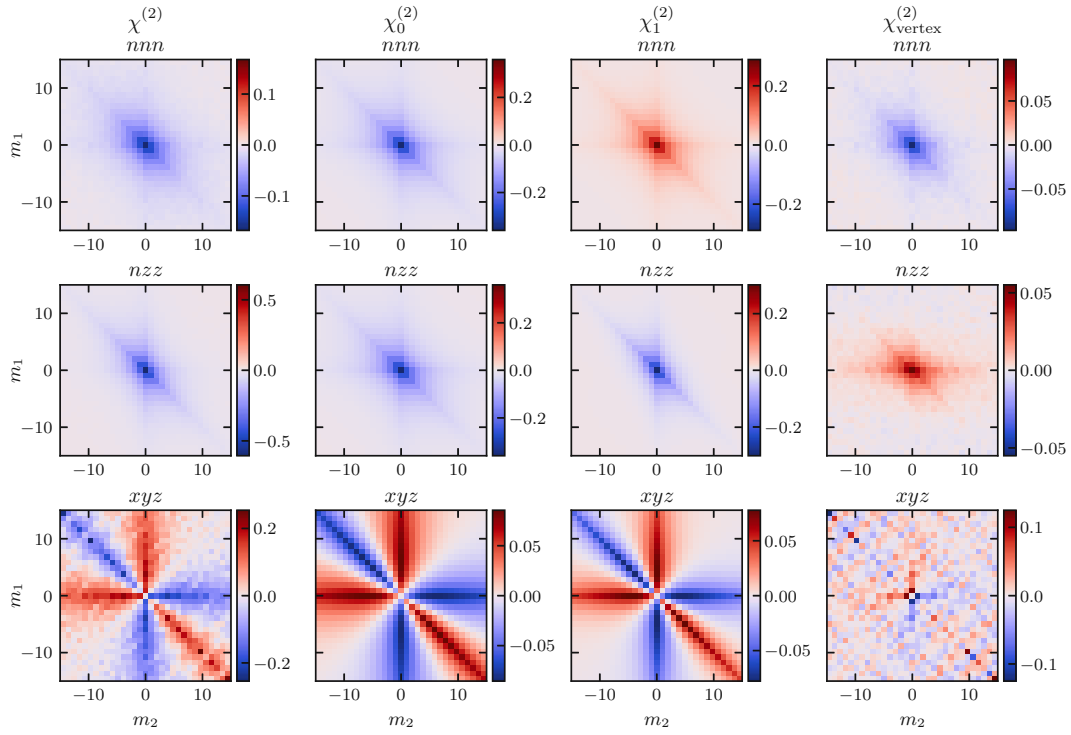

Figure 5.10.: Same as fig. 5.9 except now $\epsilon = -6.6$ corresponding to $n \approx 1.68$.

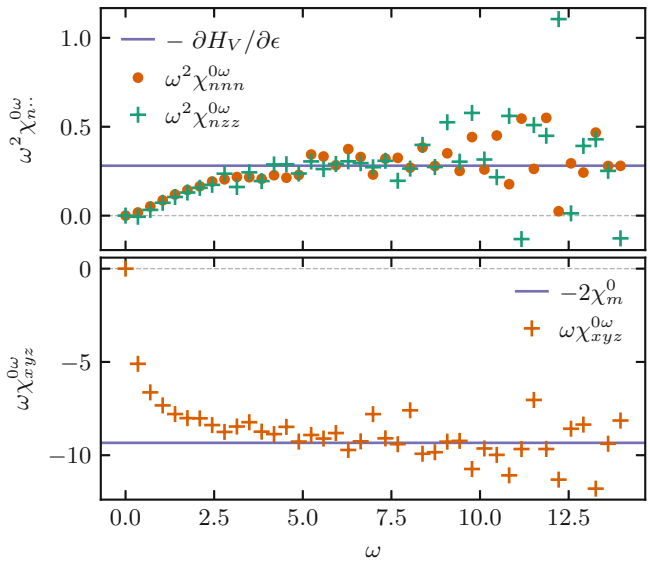

Figure 5.11.: Analysis of the asymptotic behavior of the second-order response functions at $\omega_1 = 0$, $\omega_2 = \omega$. The top plot shows the density and density-magnetic channel multiplied by ω^2, while in the bottom one the chiral channel is multiplied by ω. The dots and pluses represent the numerical data computed for an AIM with constant DOS at $D = 10$, $U = 6$, $V = 2$, $\beta = 18$ and $\epsilon = -5$. These are the same parameters as in fig. 5.9. The solid lines are the analytically calculated asymptotic behavior taken from eqs. (5.31) to (5.33).

where χ^0_m is the static, linear magnetic response function and H_V is the hybridization term in the Hamiltonian of the AIM [last term in eq. (3.1)]. Its derivative reads

$$-\frac{\partial}{\partial\epsilon}\langle H_V\rangle = \frac{4}{\beta}\sum_\nu \Delta^\nu_\uparrow\left(P3^{\nu 0}_{\uparrow\uparrow} + P3^{\nu 0}_{\uparrow\downarrow} + \beta(2-\langle\hat{n}\rangle)G^\nu_\uparrow\right), \tag{5.34}$$

where Δ is the hybridization function, $P3$ is the partially contracted two-particle Green's function $P3^{\nu'\omega} = \frac{1}{\beta}\sum_\nu G^{\nu\nu'\omega}$, G^ν is the one-particle Green's function, and we use SU(2) symmetry. Note that the $1/\omega$ terms for the density and density-magnetic channel vanish because they are proportional to $[\hat{n},\hat{n}]$ and $[\hat{\sigma}_z,\hat{\sigma}_z]$, respectively.

Figure 5.11 compares the analytical results of eqs. (5.31) to (5.33) with the numerical data for $\chi^{0\omega}$ at $\epsilon = -5$. The equations are multiplied with ω^2 and ω, respectively, because the tails drop so fast that a good comparison at medium to high frequencies would hardly be possible otherwise. This, however, also amplifies the noise of the numerical results. Nevertheless, we see a good agreement starting at frequencies as low as $\omega \approx 4$.

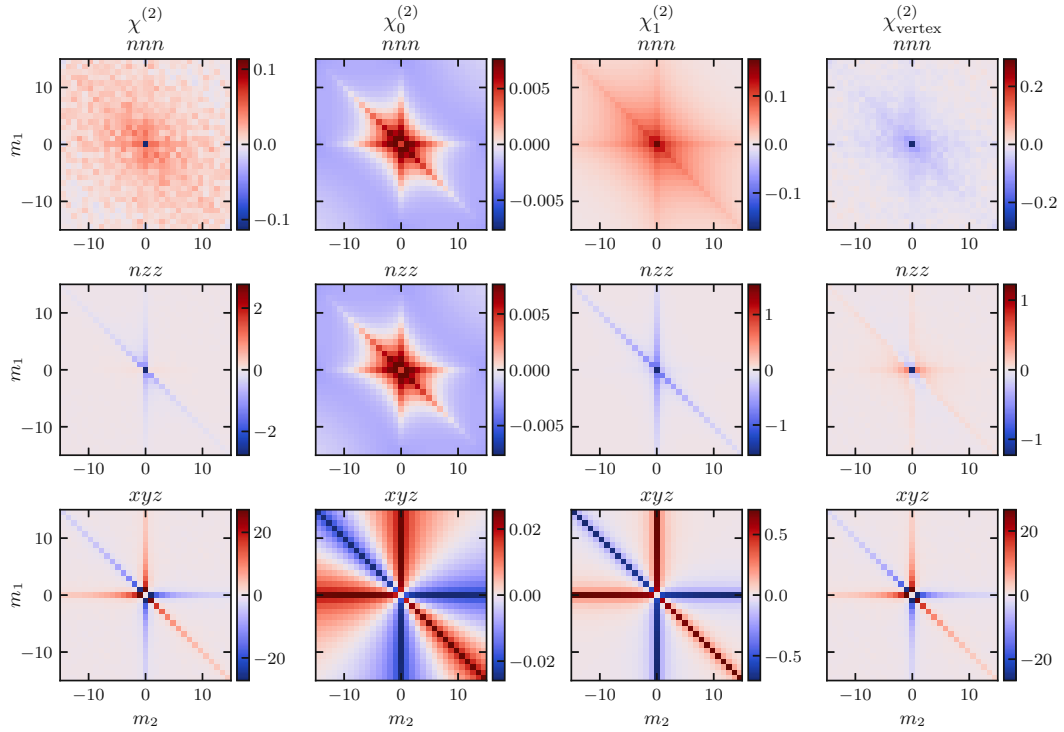

Figure 5.12.: Second-order response functions $\chi^{(2)}$ and their decomposition into the bubble terms $\chi^{(2)}_0$, first-order terms $\chi^{(2)}_1$ and vertex terms $\chi^{(2)}_{\text{vertex}}$ in the density (nnn), density-magnetic (nzz), and chiral (xyz) channel for a single-band, square-lattice HM at $n = 1.1$, $U = 12$ and $\beta = 20$.

5.4.4. Hubbard model

Figure 5.12 shows the same plots as figs. 5.9 and 5.10 namely the full, second-order response function $\chi^{(2)}$, the bubble terms $\chi^{(2)}_0$, the first-order terms $\chi^{(2)}_1$ and the vertex terms $\chi^{(2)}_{\text{vertex}}$ in the density, density-magnetic, and chiral channel. This time, however, computed for the two-dimensional HM on a square lattice with $n = 1.1$, $t = 1$ (i.e. $D = 4$), $U = 12$ and $\beta = 20$.[a] We see that for the most part the results look similar to those for the AIM with constant DOS at $\epsilon = -5$ (fig. 5.9). χ_{nnn} seems even more washed out, but the biggest differences show the bubble terms of the density and density-magnetic channel which are qualitatively different and no longer completely negative. They have a rather steep positive hill centered around $\omega_1 = \omega_2 = 0$ and a slowly decaying negative background at higher frequencies. The main takeaway that $\chi^{(2)}_0$ and $\chi^{(2)}_1$ are bad approximations is, however, still valid.

[a] Note that in this case $\chi^{(2)}$ is only the local, second-order response as discussed above. The total one would have to include the change in the hybridization function as well.

5.5. Conclusion

We have derived the equations for the frequency-resolved, nonlinear response from three-particle correlators. These are made up from three bosonic operators with three time arguments (or two time differences or frequencies). We here focused on the local correlator, the three-particle Green's function and susceptibility ($\chi^{(2)}$) on an impurity site. However, the equations derived can be straight-forwardly extended to nonlocal correlators adding a site index for each time index. We further showed how the three-particle quantities are decomposed: This involves disconnected diagrams that do not contribute to $\chi^{(2)}$ as well as two bubble diagrams $\chi_0^{(2)}$ without vertex corrections, very similar as for the two-particle correlators. Then there are diagrams $\chi_1^{(2)}$ consisting of a single particle propagator and two propagators connected by a two-particle vertex as well as genuine three-particle vertex diagrams $\chi_{\text{vertex}}^{(2)}$ that connect all incoming and outgoing lines (cf. fig. 5.2). The asymptotic behavior of the correlators is given by a $1/\omega^2$ or $1/\omega$ term, depending on whether the bosonic operators commute or not.

We have computed the correlators numerically using continuous-time QMC for the atomic limit as well as for the AIM with a single-site, a flat DOS and at DMFT self-consistency for the two-dimensional HM. We find a sizable nonlinear density and density-magnetic response functions at high doping. At half-filling, these two nonlinear responses vanish by symmetry. The pure density (nnn) response function suffers from the fact that there are large contributions from disconnected terms that need to be subtracted. This leads to a rather high level of numerical noise for the actual response function. The chiral (xyz) response function is also sizable. It contributes at half-filling and decreases with doping. It has the largest three-particle vertex contributions. For all three nonvanishing local response functions (nnn, nzz, and xyz), the three-particle vertex cannot be neglected for relevant ranges of the local one-particle potential ϵ.

5.6. Outlook

Physically the nnn and nzz response functions can, in the case of a static third bosonic n operator, be related to the change of the charge susceptibility and magnetic susceptibility with respect to a change of the local one-particle potential. If the third bosonic operator becomes time- or frequency-dependent, we have the corresponding changes against a dynamic one-particle potential. The nnn susceptibility also describes the nonlinear charge response, and nzz the nonlinear charge response to an applied magnetic field.

The chiral xyz susceptibility is arguably the most exotic response as there is no correspondence on the two-particle level; the xy, xz, and yz susceptibilities all vanish in the paramagnetic phase with SU(2) symmetry. The chiral xyz susceptibility describes a nonlinear response of the spin in x-direction if (time-dependent) magnetic fields in both y- and z-direction are applied. If one of the magnetic fields, say the one in

z-direction, is large and static, it is akin to a nuclear magnetic resonance experiment. However, here we are in second-order response, i.e., we only have a weak field in z-direction. Nonetheless, there are ideas and efforts to actually measure this response function [86].

We have seen that the contribution of the three-particle vertex F^3 to the second-order susceptibility $\chi^{(2)}$ is in general not small, but comparable to (or even larger than) the bare bubble contribution $\chi_0^{(2)}$ and contributions $\chi_1^{(2)}$ from two-particle vertices plus a disconnected propagator. This means that previous approaches to calculate nonlinear responses, such as the Hall and Raman response which only included $\chi_0^{(2)}$ or at most $\chi_1^{(2)}$, need to be reassessed for strongly correlated electron systems. Numerical approaches, as we have employed here for the local susceptibilities, become prohibitively expensive for the full lattice. This calls for developing approaches such as a three-particle Bethe–Salpeter equation for calculating the three-particle vertex F^3 also in the nonlocal case.

6. Three-particle ladder

It's complicated

John Rambo

The full three-particle vertex F_3, introduced in section 4.4, is the sum of all Feynman diagrams that fully connects three in- and three outgoing particles. Using all available symmetries we can reduce it to five degrees of freedom per spacetime dimension and, as shown in section 4.3, three independent spin components. What remains is still a complex object, which is expected to be expensive to compute and even storing it becomes difficult if we do not restrict ourselves to its local part. Fortunately we can build it completely from simpler two-particle vertices since the only interaction term we consider is a two-particle interaction. In section 4.5 we already saw one possible way to do this by constructing the three-particle vertex F_3 from full two-particle vertices F_2. However, this method involves manually figuring out the diagrams at each order which quickly becomes tedious.

In this chapter we propose a different approach where we approximate the full three-particle vertex as a geometric series of irreducible two-particle vertices. Our motivation for this are the ladder diagrams generated by the Bethe–Salpeter equations on the two-particle level. Therefore, we start by deriving a three-particle equivalent of the Bethe–Salpeter equations. We then introduce an approximation that allows us to formulate the desired geometric series. To test the approximation we compute the contribution of the three-particle vertex to second-order response functions, once from exact diagonalization (ED) results and once from the approximate ladder. First numerical calculations show that a single ladder is not enough and, for symmetry reasons, ladders in all nine three-particle channels must be considered. Even then the approximation only yields qualitatively good results for small interactions.

6.1. Three-particle Bethe–Salpeter-like equations

Considerations for the three-particle equivalent of the Bethe–Salpeter equations were already made in Ribic [2]. However, the derivation below was derived independently, and is a good starting point and motivation for the main topic of this chapter: the approximate three-particle ladder.

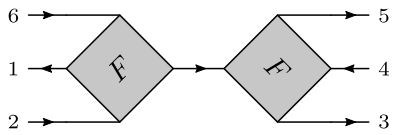

Figure 6.1.: The only diagram 1PR in the channel that separates (612) from (345). Looking at table 4.2 this is the same as the three-particle channel 41.

Let us start by writing down the two-particle Bethe–Salpeter equations that we introduced in eq. (2.43) in a very simplified form,

$$F = \Gamma_r + \Gamma_r \cdot F, \tag{6.1}$$

where F is the full vertex, Γ_r are the vertices irreducible in a single channel r, and $\cdot$ denotes the proper connection of two vertex diagrams with Green's function lines in the correct channel. Generalizing this from the two-particle to the three-particle level seems straightforward. A diagram is three-particle reducible (3PR) if it can be separated into two disconnected parts by cutting three Green's function lines, and three-particle irreducible (3PI) otherwise. In section 4.2 we already identified the ten three-particle channels, so we just need to define $\Gamma_{3,r}$ as the vertex that is 3PI in one of them, use three instead of two Green's functions to connect everything, and we are done.

As it turns out, it is not that easy. The two-particle level has the very nice advantage that all diagrams are inherently one-particle irreducible (1PI) (see section 2.6). This is not true for the three-particle level. With a four-point interaction we can easily draw a diagram that goes from three lines down to a single one and then back to three again. Such a diagram is shown in fig. 6.1. Cutting the single Green's function line in the middle separates the diagram into two connected parts: (612) and (345). This is the same separation that happens when cutting the three Green's function lines of a diagram 3PR in the $41 = (345)(612)$ channel (see table 4.2). We can do this for all other channels too. This shows that the channels where we encounter one-particle reducibility are the very same as the nine pph channels for three-particle reducibility.[1]

If we were to connect two diagrams that are 1PR in the same channel we would have built a one-particle insertion. Since we are drawing our diagrams with full Green's functions this would lead to double counting and is therefore not allowed. To avoid this we do not build a three-particle Bethe–Salpeter-like equation with F_3 and $\Gamma_{3,r}$, but subtract diagrams 1PR in r first. We denote the three-particle vertex that is 1PI in channel r with $\Gamma_{1,r}$, and the one the is 1PI and 3PI in r with $\Gamma_{1,3,r}$.

However, even with those quantities there is still one remaining problem: some 3PR diagrams cannot be uniquely cut into 3PI parts. A simple example of this is shown in fig. 6.2, where there are two possible ways to cut the diagram and each one results in different 3PI parts. The underlying issue is that 3PI diagrams can be two-particle

[1] The ppp channel has no one-particle equivalent since this would require a two-particle vertex with at least three ingoing lines which violates particle conservation.

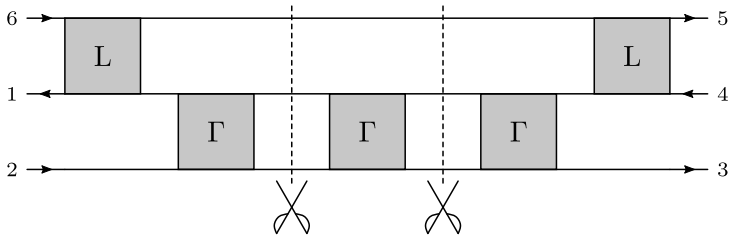

Figure 6.2.: A simple example diagram that illustrates the ambiguity that arises when cutting 3PR diagrams into 3PI parts. In the notation from chapter 4, it is reducible in the (345)(612) or 41 channel. Note that cutting after the leftmost or before the rightmost vertex is not allowed since then we would end up with disconnected parts that are not three-particle vertices anymore. Also, the upper vertices are upside down because of how we defined them in fig. 2.4.

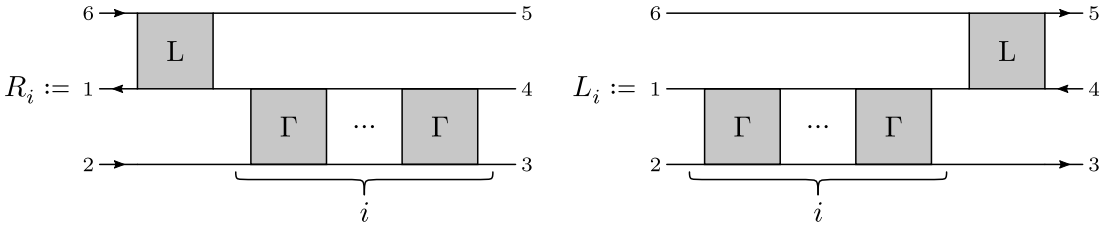

Figure 6.3.: Definition of R_i and L_i. Again, the upper vertices are upside down because of how we defined them in fig. 2.4.

reducible (2PR) in related channels. This means that two-particle vertices can be added or cut off from those diagrams without changing their three-particle reducibility. If we use the notation defined in fig. 6.3, where R_i has i two-particle vertices on the right and L_i has i vertices on the left, we see that

$$R_i \cdot L_j = R_n \cdot L_m, \quad \forall\ i + j = n + m. \tag{6.2}$$

Since both R_i and L_i are elements of $\Gamma_{1,3,r}$ and $\Gamma_{1,r}$ we would again invoke double counting.

One way to prevent this and make cutting off 3PI parts unique is to require that we always cut off the "leftmost" part. This is equivalent to requiring that the vertices 1PI and 3PI in a channel r must also be two-particle irreducible (2PI) in the three related two-particle channels "on the right". Denoting this quantity with $\Gamma_{1,\vec{2},3,r}$, we can finally write down the three-particle equivalent of the Bethe–Salpeter equation:

$$\Gamma_{1,r} = \Gamma_{1,\vec{2},3,r} + \Gamma_{1,\vec{2},3,r} \cdot \Gamma_{1,r}. \tag{6.3}$$

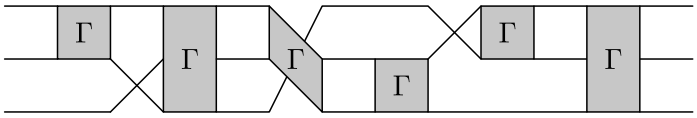

Figure 6.4.: Example diagram for an approximate three-particle ladder built only from two-particle vertices. Only Green's function lines touching the corners of a vertex are really connected to it. The middle line on the right side, e.g., is not connected to the right-most vertex but runs through "behind" it.

To recover the full vertex F_3 we need to add the diagrams 1PR in channel r. As it turns out there is only a single one for each channel. They are all of the same form: two full two-particle vertices F_2 connected with a single Green's function line G. One of them is depicted in fig. 6.1. With this we have

$$F_3 = \Gamma_{1,r} + (F_2 G F_2)_r. \tag{6.4}$$

6.2. Approximate three-particle ladder

In the last section we saw that the exact three-particle ladders generated by the Bethe–Salpeter-like equations are built from three-particle vertices that are 1PI and 3PI in a certain channel and 2PI in the three related channels "on the right". The problem is that, we have no easy way to compute them. We can construct them order by order from two-particle vertices, but that is equally tedious and unfeasible as the vertex expansion from section 4.5, so there would be no improvement in that regard. Instead, we propose approximating the exact three-particle ladder with a ladder of two-particle vertices.

The general idea is to find all possible ways to connect a two-particle vertex to three lines on the left and three lines on the right, and then build a ladder from that. Figure 6.4 shows an example diagram for such a ladder. Formally, we can write this as

$$\tilde{L} = \sum_{n=1}^{\infty} P(MP)^n, \tag{6.5}$$

where $\tilde{L}$ is the approximate ladder, P consists of all permutations of the three lines of the ladder and M contains a two-particle vertex. Since the ladder can have multiple vertices right next to each other, using the full two-particle vertex in M would lead to double counting. To avoid this issue we use Γ_r, the two-particle vertex irreducible only in channel r. Which channel we need depends on which kind of three-particle ladder we build: either one with three particles (ppp) or one with two particles and a hole (pph).[2] In the ppp case we only need Γ_{pp}, in the pph case we need to add Γ_{ph} as well.

[2]The two cases with three holes or two holes and one particle can easily be obtained from the other two via a particle–hole transformation.

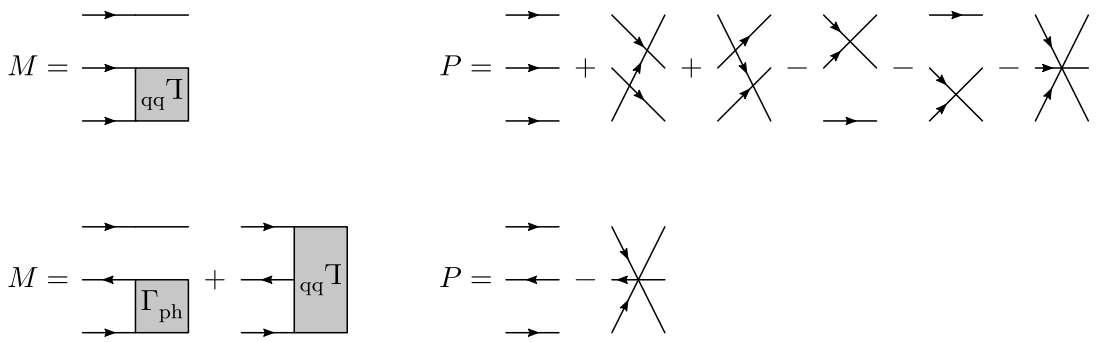

Figure 6.5.: Diagrammatic representation of M and P for ppp ladders (top) and pph ladders (bottom). The pp vertex is mirrored because of how we defined it in fig. 2.4.

The permutation matrix P is also different in the two cases because we are not allowed to swap particles with holes and vice versa. Thus, for a pph ladder the permutation matrix only consists of two instead of $3! = 6$ terms. Figure 6.5 shows a diagrammatic representation of M and P for both cases.

From now on we only focus on the pph ladder since it directly matches with our definition of the three-particle Green's function shown in fig. 4.1. Because of that it is also easier to compute the vertex corrections to the second-order response functions $\chi^{(2)}_{\text{vertex}}$ from it, which is convenient for our comparison tests. It is, however, straightforward to apply the ideas, concepts, issues, and solutions presented in the rest of this section to the ppp case.

Let us continue by introducing some notation. We label the lines of the ladder with the numbers 1 to 3 starting from the top. Since in the first term of M shown in fig. 6.5 (bottom left) the ph vertex sits between lines 2 and 3 we call it M_{23}. The second term with the pp vertex is then called M_{13}, and we can write

$$M = M_{23} + M_{13}. \tag{6.6}$$

In combination with the permutation matrix P the crossing symmetry of M_{13}, inherited from Γ_{pp}, causes the following double counting issue:

$$PM_{13} = M_{13}P = 2M_{13}. \tag{6.7}$$

This can easily be corrected with an additional factor of $1/2$.

Equation (6.7) also shows that M_{13} commutes with P. If this were true for the whole M we could simplify eq. (6.5), by pulling all permutation matrices to one side, disentangling the ladder. M_{23} prevents this because swapping the two particle lines folds the ph vertex up, creating a new diagram, let us call it M_{12}, that is not in M. However, swapping the particle lines of M_{12} brings us back to M_{23}, so the two diagrams turn into each other

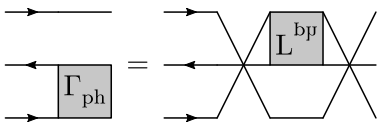

Figure 6.6.: Diagrammatic representation of eq. (6.8), the relation between M_{12} and M_{23}

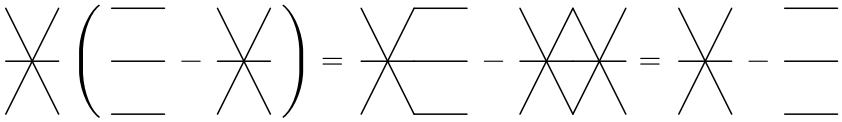

Figure 6.7.: Diagrammatic representation of eq. (6.9)

under the considered permutation. This means that in order to make M commute with P all we need to do is to symmetrize its ph part and write it as the sum of the two diagrams. Denoting the permutation matrix that exchanges the two particle lines with P_{13}, we can write M_{23} in terms of M_{12}:

$$M_{23} = P_{13} M_{12} P_{13}. \tag{6.8}$$

Figure 6.6 shows a diagrammatic representation of this. Applying P_{13} to the whole permutation matrix P only gives a sign:

$$P_{13}P = PP_{13} = P_{13} - P_{13}P_{13} = P_{13} - \mathbb{1} = -P, \tag{6.9}$$

where $\mathbb{1}$ is the identity permutation. The diagrams for this equation can be found in fig. 6.7. Putting everything together we can compute the desired symmetrization,

$$PM_{23}P = \frac{1}{2}P(M_{23} + P_{13}M_{12}P_{13})P = \frac{1}{2}P(M_{23} + M_{12})P. \tag{6.10}$$

For later convenience we pull out the factors of $1/2$ from eq. (6.10) and the double counting issue in eq. (6.7) when redefining M:

$$M = M_{12} + M_{23} + M_{13}. \tag{6.11}$$

This new M commutes with P:

$$PM = M - P_{13}M_{12} - P_{13}M_{23} - P_{13}M_{13} = M - M_{23}P_{13} - M_{12}P_{13} - M_{13}P_{13} = MP. \tag{6.12}$$

With the previously pulled out factor of $1/2$, we get

$$\tilde{L} = \sum_{n=1}^{\infty} P\left(\frac{1}{2}MP\right)^n = \sum_{n=1}^{\infty} M^n P\left(\frac{1}{2}P\right)^n \tag{6.13}$$

for the approximate ladder. One can easily check that $P/2$ is idempotent, and we can thus further simplify the ladder equation:

$$\tilde{L} = \sum_{n=1}^{\infty} M^n P\left(\frac{1}{2}P\right)^n = \sum_{n=1}^{\infty} M^n P\frac{1}{2}P = \sum_{n=1}^{\infty} M^n P. \tag{6.14}$$

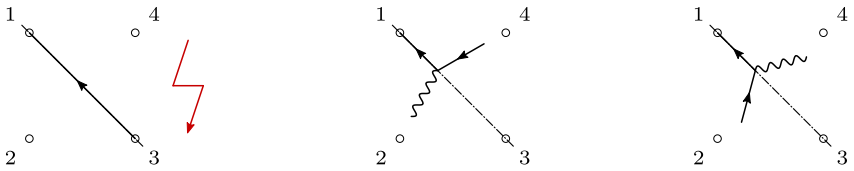

Figure 6.8.: Visual proof that a diagram with a two-particle interaction cannot be symmetric along a diagonal. The first diagram is not allowed since in our convention an annihilation operator sits at both coordinates [see eq. (2.29)]. The second and third diagram illustrate that it is impossible to add an interaction term and keep the diagram symmetric along the diagonal. Therefore, a single diagram cannot be crossing symmetric on its own.

The ladder is now disentangled, with only a single permutation matrix at one end. This ensures that the ladder is crossing symmetric with respect to the two particle lines: it has two crossing symmetries. The full three-particle vertex, however, is crossing symmetric with respect to all particle and hole lines: it has six crossing symmetries. This difference in symmetries is an important issue that we will come back to later.

The simpler form of eq. (6.14) also reveals that we generate a lot of disconnected terms. They are the ones where we do not mix the different components of M and therefore build a two-particle ladder with a disconnected Green's function running next to it. There is one such disconnected term for each ladder. Subtracting them leaves us with

$$L = \sum_{n=1}^{\infty} (M^n - M_{12}^n - M_{23}^n - M_{13}^n) P. \tag{6.15}$$

Now let us focus on the last double counting issue. Again, it comes from the irreducible pp vertex in M_{13}, but this time it has nothing to do with the permutation matrix. Γ_{pp} is the sole perpetrator and this issue already appears on the two-particle level. There it mandates the factor of $1/2$ in the Bethe–Salpeter equation of the pp channel [see eq. (2.43)]. To see how this generalizes to the three-particle ladder we need to take a closer look at how crossing symmetry works and what happens if we connect two crossing symmetric vertices with two particle lines.

Let us hence start by looking at the crossing symmetry for a two-particle vertex diagram. With a two-particle interaction term it is not possible that any given diagram contributing to the vertex is crossing symmetric on its own. The reason is that with our established conventions such a diagram would have to be symmetric along one of the two diagonals (1–3 or 2–4) and that is impossible as illustrated in fig. 6.8. Without any interaction terms we would have to draw a Green's function line from 1 to 3, which is not allowed because in our convention an annihilation operator sits at both coordinates [see eq. (2.29)]. If we add an interaction term, that effectively splits the Green's function line into an interaction line and another Green's function line. No matter at what angle or on what

side we draw that this will never be symmetric along the 1–3 diagonal because they are two different types of lines.

Objects like the two-particle Green's function, full vertex, or irreducible pp vertex are crossing symmetric because they consist of a sum of terms and this sum contains pairs of diagrams that turn into each other under crossing exchange. The reason for the diagrams to come in pairs and not in larger groups is that crossing is an involution, i.e., applying it twice yields the identity. Probably the simplest example for such a pair of diagrams are the disconnected parts of the two-particle Green's function G_2 shown in fig. 2.5. Swapping $1 \leftrightarrow 3$ or $2 \leftrightarrow 4$ turns the first diagram into the second and vice versa. For a general discussion let $\gamma_1, \gamma_2 \in \Gamma_{\text{pp}}$ be a crossing-related pair of diagrams, i.e.,

$$\begin{aligned} \gamma_1 &= C\gamma_2 = \gamma_2 C \\ \gamma_2 &= C\gamma_1 = \gamma_1 C \end{aligned} \tag{6.16}$$

where C denotes the crossing operation. If two irreducible pp vertices are connected with two particle lines both terms $\gamma_1\gamma_2$ and $\gamma_2\gamma_1$ appear. However, since crossing is its own inverse we can write

$$\gamma_1\gamma_2 = \gamma_1 CC\gamma_2 = \gamma_2\gamma_1. \tag{6.17}$$

Therefore, we count all diagrams twice and need the factor of $1/2$ in the Bethe–Salpeter equation for the pp channel.

For the three-particle ladder the case is similar. The main difference is that we can have diagrams from ph vertices in between the pp ones, so we need to consider that in our argument. Let m be a general combination of ph diagrams that can appear in the ladder, i.e., $m \in (M_{12} + M_{23})^n$. Its crossing-related counterpart $\bar{m} = P_{13}mP_{13}$ is the same diagram but with the M_{12} and M_{23} parts swapped [remember eq. (6.8)], so it is also generated by the ladder. If we pick an arbitrary pair of crossing-related diagrams $\gamma_1, \gamma_2 \in M_{13}$, the ladder generates both $\gamma_1 m \gamma_2$ and $\gamma_2 \bar{m} \gamma_1$. Using the same trick as before we can write

$$\gamma_1 m \gamma_2 = \gamma_1 P_{13}P_{13} m P_{13}P_{13} \gamma_2 = \gamma_2 \bar{m} \gamma_1, \tag{6.18}$$

and show that we count all such diagrams twice. Therefore, we must add a factor of $1/2$ in front of Γ_{pp}, as well.

With the last topological issue resolved we can finally work out the full equations for the three-particle ladder and its components with all prefactors, indices, and arguments. So far we always drew horizontal ladders in the 41 channel, so we choose the matching frequency notation. Both the channel and its frequency notation are defined in table 4.2. A diagrammatic representation with all spin and frequency indices is shown in fig. 6.9. Ladders in different pph channels can easily be obtained by rotation or swapping of external legs. An example of this is illustrated in fig. 6.10. Due to implementation details the frequency notations for the irreducible two-particle vertices are not the ones introduced in table 2.1 and fig. 2.4. Instead, all frequencies are shifted by ω as shown in

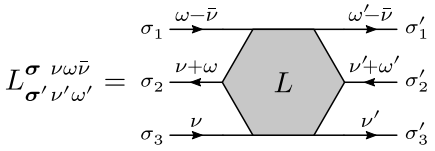

Figure 6.9.: Frequency and spin notation for the three-particle ladder

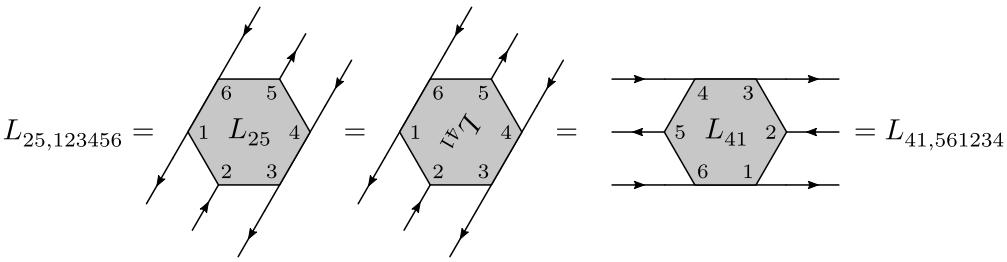

Figure 6.10.: The pph ladder in the 25 channel, obtained by rotating the one in the 41 channel

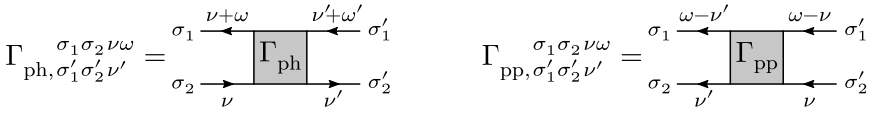

Figure 6.11.: Frequency and spin notations for the two-particle vertices used in the three-particle ladder

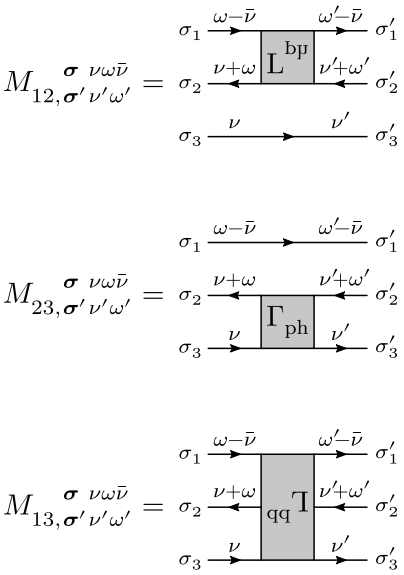

Figure 6.12.: Diagrammatic representation of eqs. (6.19) to (6.21), the definitions of the three components of M

fig. 6.11. We also denote frequency and spin indices on the right side of the diagrams as subscripts to save horizontal space.

To connect the two-particle vertices in the ladder we need Green's functions. We choose to add two on the right of each vertex in the M's and then three on the very left of the entire ladder. This means that the ladder is not an approximation for a "naked" three-particle vertex but has Green's functions attached to every external point. This is convenient since we need them anyway for computing the vertex contribution to second-order response functions $\chi^{(2)}_{\mathrm{vertex}}$. Putting everything together yields

$$M_{12,\boldsymbol{\sigma}'\nu'\omega'}^{\boldsymbol{\sigma}\,\nu\omega\bar{\nu}} := \frac{1}{\beta}\delta_{\sigma_3'}^{\sigma_3}\delta_{\nu'}^{\nu}\Gamma_{\mathrm{ph},\sigma_2'\sigma_1'(\omega'-\bar{\nu})}^{\sigma_2\sigma_1(\omega-\bar{\nu})(\nu+\bar{\nu})} G^{\omega'-\bar{\nu}} G^{\omega'+\nu'}, \tag{6.19}$$

$$M_{23,\boldsymbol{\sigma}'\nu'\omega'}^{\boldsymbol{\sigma}\,\nu\omega\bar{\nu}} := \frac{1}{\beta}\delta_{\sigma_1'}^{\sigma_1}\delta_{\omega'}^{\omega}\Gamma_{\mathrm{ph},\sigma_2'\sigma_3'\nu'}^{\sigma_2\sigma_3\nu\omega} G^{\nu'} G^{\omega'+\nu'}, \tag{6.20}$$

$$M_{13,\boldsymbol{\sigma}'\nu'\omega'}^{\boldsymbol{\sigma}\,\nu\omega\bar{\nu}} := \frac{1}{2\beta}\delta_{\sigma_2'}^{\sigma_2}\delta_{\nu'+\omega'}^{\nu+\omega}\Gamma_{\mathrm{pp},\sigma_1\sigma_3\nu'}^{\sigma_1'\sigma_3'\nu(\omega+\nu-\bar{\nu})} G^{\omega'-\bar{\nu}} G^{\nu'}, \tag{6.21}$$

for the components of M, where $\boldsymbol{\sigma} = (\sigma_1, \sigma_2, \sigma_3)$ and similarly for $\boldsymbol{\sigma}'$. The factors $1/\beta$ ensure that M is dimensionless, which is necessary because we sum over different powers of them in the ladder. A diagrammatic representation of the M's is shown in fig. 6.12. The permutation matrix is simply given by a combination of Kronecker deltas

$$P_{\boldsymbol{\sigma}'\nu'\omega'}^{\boldsymbol{\sigma}\,\nu\omega\bar{\nu}} = \delta_{\sigma_1'}^{\sigma_1}\delta_{\sigma_2'}^{\sigma_2}\delta_{\sigma_3'}^{\sigma_3}\delta_{\omega'}^{\omega}\delta_{\nu'}^{\nu} - \delta_{\sigma_3'}^{\sigma_1}\delta_{\sigma_2'}^{\sigma_2}\delta_{\sigma_1'}^{\sigma_3}\delta_{\nu'}^{\omega-\bar{\nu}}\delta_{\nu'+\omega'}^{\nu+\omega}. \tag{6.22}$$

Finally the full equation for the approximate three-particle ladder reads

$$L^{\boldsymbol{\sigma}\ \nu\omega\bar{\nu}}_{\boldsymbol{\sigma}'\ \nu'\omega'} = -\beta^2 G^{\omega-\bar{\nu}} G^{\nu+\omega} G^{\nu} \sum_{\sigma_1,\nu_1,\omega_1} \left(\sum_{n=0}^{\infty} (M^n - M^n_{12} - M^n_{23} - M^n_{13}) + 2 \right)^{\boldsymbol{\sigma}\ \nu\omega\bar{\nu}}_{\boldsymbol{\sigma}_1\ \nu_1\omega_1} P^{\boldsymbol{\sigma}_1\nu_1\omega_1\bar{\nu}}_{\boldsymbol{\sigma}'\ \nu'\omega'}, \tag{6.23}$$

where the prefactor of β^2 ensures a dimension of $[\tau]^5$, as it should be for a quantity depending on five Matsubara frequencies. The addition of 2 is necessary because the sum now starts at $n = 0$ to turn it into a proper geometric series. The notation also shows that the equation is diagonal in $\bar{\nu}$ and the terms can be viewed as simple matrices when condensing $(\boldsymbol{\sigma}, \nu, \omega)$ into a single compound index. This makes it easy to employ the closed-form formula for the geometric series.

Substituting the 1PI vertex, Γ_1, in eq. (6.4), with the approximate three-particle ladder, L, turns out to yield even qualitatively bad results. The reason for that lies in the crossing symmetries. As mentioned before, the approximate ladder only satisfies two of the six crossing symmetries of the full three-particle vertex F_3. The 1PR diagram $(F_2GF_2)_r$ in eq. (6.4) is in the same channel r as $\Gamma_{1,r}$ or in this case the ladder, and therefore has the same problem. To solve this we compute the average of the approximate ladder and the 1PR diagram $(F_2GF_2)_r$ over all nine pph channels defined in table 4.2. The full three-particle vertex (with legs) in this approximation is thus given by

$$GGGF_3GGG \approx \frac{1}{9} \sum_r L_r + GGG(F_2GF_2)_r GGG, \tag{6.24}$$

where r runs over the nine pph channels.

It is really important to average because summing would invoke overcounting. We can see this when looking at the nine second-order diagrams of the two-particle vertex expansion of G_3 in fig. 4.14. It turns out that in every pph channel the ladder generates eight of those nine diagrams and the 1PR diagram added separately is the ninth. This means that a single channel already contains all diagrams up to second order in F_2 and not averaging would lead to overcounting them by a factor of nine.

Note that we do not need to come up with nine versions of eq. (6.23) to compute the ladders in all pph channels. Instead, it is much easier to convert the ladder in the 41 channel to the other ones by rotation or swapping of legs as exemplified in fig. 6.10.

The last step in our computations is using the approximate three-particle vertex and calculating its contribution to the second-order response function $\chi^{(2)}_{\text{vertex}}$. Since our approximation already comes attached with six Green's functions, this is, at least in theory, easily done by summing over the fermionic frequencies:

$$\chi^{\omega\omega'}_{\text{vertex}} = \sum_{\nu\nu'\bar{\nu}} (GGGF_3GGG)^{\nu\omega\bar{\nu}}_{\nu'\omega'}. \tag{6.25}$$

In numerical calculations these infinite sums are of course limited by the grid size. As it turns out it is important how exactly the sums are implemented because some terms

need to cancel. The reason for that is that the imaginary part of $\chi_{\text{vertex},\uparrow\uparrow\uparrow}$ and $\chi_{\text{vertex},\uparrow\uparrow\downarrow}$ must vanish. This can easily be shown when remembering that complex conjugation inverts the order of spins and fermionic frequencies while also negating the latter [8]:[3]

$$\left(F^{\nu_1\cdots\nu_6}_{123456}\right)^* = F^{-\nu_6\cdots-\nu_1}_{654321}. \tag{6.26}$$

If we now use, e.g., the first ph notation from table 4.1,

$$\begin{aligned}\omega_a &= \nu_1 - \nu_2,\\ \omega_b &= \nu_3 - \nu_4,\\ \omega_c &= \nu_5 - \nu_6,\end{aligned} \tag{6.27}$$

we see that the bosonic frequencies also change their order but keep their signs after complex conjugation:

$$\begin{aligned}\omega_a &\to -\nu_6 + \nu_5 = \omega_c,\\ \omega_b &\to -\nu_4 + \nu_3 = \omega_b,\\ \omega_c &\to -\nu_2 + \nu_1 = \omega_a.\end{aligned} \tag{6.28}$$

For the second-order response functions we therefore have

$$\left(\chi^{\omega_a\omega_b\omega_c}_{\text{vertex},\,123456}\right)^* = \chi^{\omega_c\omega_b\omega_a}_{\text{vertex},\,654321}. \tag{6.29}$$

Using the swapping symmetries introduced in eqs. (4.11) to (4.13) we see that the $\uparrow\uparrow\uparrow$ and $\uparrow\uparrow\downarrow$ components of $\chi^{(2)}_{\text{vertex}}$ are indeed purely real:

$$\left(\chi^{\omega_a\omega_b\omega_c}_{\text{vertex},\uparrow\uparrow\uparrow}\right)^* = \chi^{\omega_c\omega_b\omega_a}_{\text{vertex},\uparrow\uparrow\uparrow} = \chi^{\omega_a\omega_b\omega_c}_{\text{vertex},\uparrow\uparrow\uparrow}, \tag{6.30}$$

$$\left(\chi^{\omega_a\omega_b\omega_c}_{\text{vertex},\uparrow\uparrow\downarrow}\right)^* = \chi^{\omega_c\omega_b\omega_a}_{\text{vertex},\downarrow\uparrow\uparrow} = \chi^{\omega_a\omega_b\omega_c}_{\text{vertex},\uparrow\uparrow\downarrow}. \tag{6.31}$$

The problem for the approximate ladder is that it does not have those swapping symmetries.[4] Fortunately, they are not required, if we do the complex conjugation of the ladder properly and choose the right ph notation. To show what we mean with the first part, let us do an explicit complex conjugation for a term that appears in the ladder. A simple example is

$$\left(\Gamma^{\nu_1\nu_2\nu_3\nu}\, G^{\nu}\, \Gamma^{\nu\nu_6\nu_5\nu_4}\right)^* = \Gamma^{\nu-\nu_3-\nu_2-\nu_1}\, G^{-\nu}\, \Gamma^{-\nu_4-\nu_5-\nu_6-\nu}. \tag{6.32}$$

The corresponding Feynman diagrams are found in fig. 6.13 and show that the positions of the vertices and frequencies get mirrored along the vertical axis with the frequencies also being negated. This holds in general for all ladder terms as can be seen when

[3] The cited reference only shows that G_3 behaves like that under complex conjugation. With a straightforward although tedious calculation one can show, however, that the six, fully disconnected parts of G_3 and the nine partially connected parts follow the same equations. Therefore, the full vertex F_3 must follow them as well.

[4] The swapping symmetries are just a combination of two crossing symmetries, and we already pointed out that the ladder is missing most of the latter.

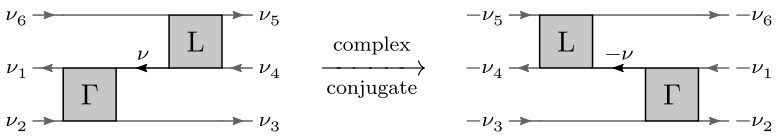

Figure 6.13.: Diagrammatic representation of eq. (6.32). The complex conjugation mirrors the positions of the vertices and frequencies along the vertical axis. The frequencies are also negated.

computing a few more simple diagrams and then using induction. Since the ladder generates all possible arrangements of two-particle vertices it also contains all mirrored terms. Therefore, the correct way to complex conjugate a ladder is

$$\left(L^{\nu_1\dots\nu_6}_{123456}\right)^* = L^{-\nu_4-\nu_3-\nu_2-\nu_1-\nu_6-\nu_5}_{432165}. \tag{6.33}$$

This does not contradict eq. (6.26) since the full three-particle vertex has all crossing and swapping symmetries, and we can write

$$\left(F^{\nu_1\dots\nu_6}_{123456}\right)^* = F^{-\nu_6\cdots-\nu_1}_{654321} = F^{-\nu_4-\nu_3-\nu_2-\nu_1-\nu_6-\nu_5}_{432165}. \tag{6.34}$$

To ensure that the $\uparrow\uparrow\uparrow$ and $\uparrow\uparrow\downarrow$ components of $\chi^{(2)}_{\text{vertex}}$ are real, we have to find a ph notation where the imaginary parts of the ladder cancel when summing over the fermionic frequencies. This means that the complex conjugate of a frequency component of L must map to the same bosonic frequencies. The $\text{ph}_{\overline{a}}$ notation from table 4.1 achieves exactly that:

$$\begin{aligned}
\overline{\omega}_a &= \nu_1 - \nu_4 \;\rightarrow\; -\nu_4 + \nu_1 = \overline{\omega}_a, \\
\omega'_b &= \nu_3 - \nu_2 \;\rightarrow\; -\nu_2 + \nu_3 = \omega'_b, \\
\omega_c &= \nu_5 - \nu_6 \;\rightarrow\; -\nu_6 + \nu_5 = \omega_c,
\end{aligned} \tag{6.35}$$

and therefore

$$\left(L^{\nu_a\overline{\omega}_a\nu_b\omega'_b\nu_c}_{123456}\right)^* = L^{-\nu_a\overline{\omega}_a-\nu_b\omega'_b-\nu_c}_{432165}. \tag{6.36}$$

In the numerical implementation we only have to make sure that we sum over a symmetric interval of fermionic frequencies to ensure the cancellation.

So far we only considered the approximate three-particle ladder in the 41 channel. However, in eq. (6.24) we average over ladders in all nine pph channels. Fortunately, this does not cause additional issues with the cancellation of imaginary parts: When converting the ladder in the 41 channel to some other channel we have to swap one or two pairs of legs. Channels 23 and 65 are the ones requiring two pairs. Their Feynman diagrams turn out to be symmetric along the vertical axis, so the same considerations as for the 41 channel hold, and the imaginary parts cancel. The remaining six channels are not symmetric on their own, but they form mirror pairs: 25 and 63, 45 and 61, as well

as 21 and 43. When summing over those pairs they cancel each other's imaginary parts for the ↑↑↑ and ↑↑↓ component as well.

Putting everything together we end up with the following approximation for the vertex contribution to the second-order response function:

$$\chi^{\overline{\omega}_a\omega'_b}_{\text{vertex}} \approx \sum_{\nu_a\nu_b\nu_c} \frac{1}{9} \sum_r L_r^{\nu_a\overline{\omega}_a\nu_b\omega'_b\nu_c} + (GGG(F_2GF_2)_rGGG)^{\nu_a\overline{\omega}_a\nu_b\omega'_b\nu_c}, \tag{6.37}$$

where the ladder L and the 1PR diagram F_2GF_2 are in $\text{ph}_{\overline{a}}$ notation, and r runs over the nine pph channels.

6.3. Numerical results

All numerical results presented in this section are computed for a single-band, square lattice Hubbard model (HM) with nearest neighbor hopping $t = 1$, total density $n = 1.1$, inverse temperature $\beta = 10$, and local Coulomb interaction $U \in \{0.5, 1, 2, 3, 4\}$. The dynamical mean-field theory (DMFT) solution is obtained with w2dynamcis [82], a continuous-time quantum Monte Carlo (QMC) solver, which also allows calculating the local two-particle Green's function and then, by employing the parquet and Bethe–Salpeter equations, all local two-particle vertices. The hybridization expansion used by w2dynamcis is, however, not well suited in the limit of small U since the hybridization becomes relatively large compared to the interaction. This means that while the one-particle Green's function can still be obtained with high enough accuracy and precision, the irreducible vertices are too noisy to be used in the three-particle ladder. Therefore, we employ different methods for computing Γ. For the smallest interactions, $U \in \{0.5, 1, 2\}$, we use a parquet solver [87, 88] to compute the irreducible vertices in the parquet approximation $\Lambda \approx U$, which yields noise free results.[5] For $U \in \{3, 4\}$ we use the same parquet solver, but take the fully irreducible vertex Λ from the QMC calculation as a starting point because it turns out that the resulting Γ has less noise than the Γ computed directly from the QMC results.

6.3.1. Eigenvalues of M's

Before we compute any three-particle ladders we need to make sure that the geometric series in eq. (6.23) actually converges. To this end we compute the eigenvalues of the M's (i.e, M, M_{12}, M_{23}, and M_{13}) and check if their absolute values are less than one. More precisely, when looking at eqs. (6.19) to (6.21) (the definitions of the M's) we condense (ν, ω, σ) and (ν', ω', σ') into two compound indices. For every $\bar{\nu}$ we then have

[5] If the exact fully irreducible vertex Λ is known, the irreducible vertices Γ obtained with the parquet solver are also exact.

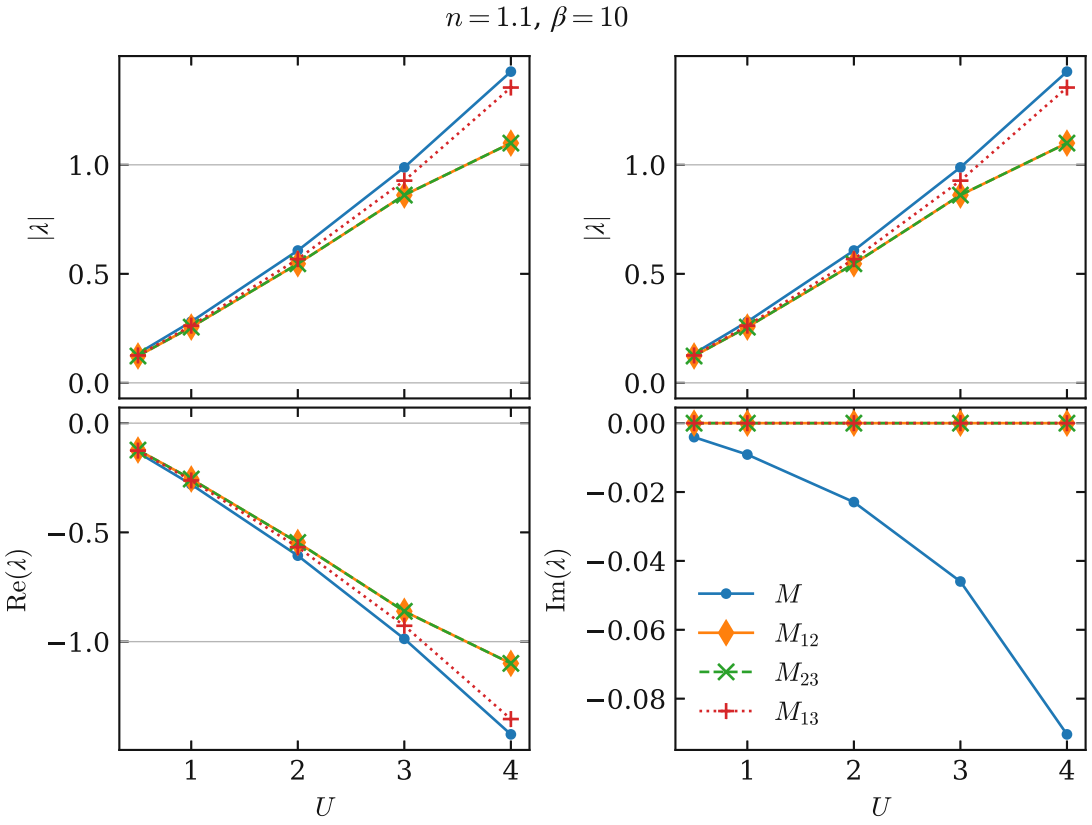

Figure 6.14.: Largest absolute eigenvalues of M's plotted over U.

a square matrix for which the eigenvalues are calculated. Since the M matrices are large ($\approx 30\,000 \times 30\,000$) and sparse we use an iterative sparse solver.

The absolute largest eigenvalues λ over all values of $\bar{\nu}$ are shown in fig. 6.14 for different interaction strengths U. We see that the eigenvalues of M are larger than those of its components, and the difference grows with U. At $U = 3$ the magnitude of the largest eigenvalue of M is just below one, so the ladder converges only up to about this point. Despite that we do not expect the ladder to blow up numerically because we compute the ladder using the closed-form solution for the geometric series, $1/(1-q)$, and the eigenvalues are close to -1 and not $+1$. We also see that M_{12} and M_{23} yield identical results which is not surprising since they both contain Γ_{ph} and are mirror versions of each other. Furthermore, M_{13} and therefore Γ_{pp} seem to give the dominant contribution to the largest eigenvalue of M and therefore the three-particle ladder as a whole. The last thing to mention is that only M seems to have eigenvalues with an imaginary part. However, when looking at more than just the largest eigenvalue we find that the components of M, especially M_{13}, have eigenvalues with similar imaginary parts as well (not shown), so this is actually not an exceptional result.

Table 6.1.: Static values ($\omega_1 = \omega_2 = 0$) of $\chi^{(2)}_{\text{vertex}}$ cut off from the color bars of fig. 6.15

	$\chi^{(2)\,00}_{\text{vertex},\uparrow\uparrow\uparrow}$		$\chi^{(2)\,00}_{\text{vertex},\uparrow\uparrow\downarrow}$	
U	ED	ladder	ED	ladder
0.5	5.6×10^{-5}	1.5×10^{-5}	-6.3×10^{-4}	-3.4×10^{-4}
1.0	4.0×10^{-4}	4.8×10^{-5}	-2.3×10^{-3}	-1.1×10^{-3}
2.0	2.4×10^{-3}	-9.1×10^{-4}	-7.1×10^{-3}	-2.2×10^{-3}
3.0	5.5×10^{-3}	-8.9×10^{-3}	-1.2×10^{-2}	9.5×10^{-4}
4.0	7.5×10^{-3}	-1.5×10^{-2}	-1.6×10^{-2}	5.7×10^{-3}

6.3.2. $\chi^{(2)}_{\text{vertex}}$: exact diagonalization vs approximate ladder

All ED calculations in this section are performed with six bath sites, obtained from the DMFT solution via pole fitting [89]. The three-particle vertex contributions to the second-order response functions are computed similarly as in chapter 5: First one-, two-, and three-particle correlators are computed with an ED code [90]. Then the disconnected parts are subtracted to obtain the full second-order response functions $\chi^{(2)}$. Next the bubble terms $\chi^{(2)}_0$ and first-order terms $\chi^{(2)}_1$ are computed from one- and two-particle quantities (see fig. 4.5). Finally, $\chi^{(2)}_0$ and $\chi^{(2)}_1$ are subtracted from the full second-order response function yielding the vertex term $\chi^{(2)}_{\text{vertex}}$. The difference to chapter 5 is that instead of the "physical" response functions χ_{nnn}, χ_{nzz}, and χ_{xyz} we compute and compare the three spin components $\chi_{\uparrow\uparrow\uparrow}$, $\chi_{\uparrow\uparrow\downarrow}$, and $\chi_{\uparrow\uparrow\overline{\downarrow}}$. The reason for that is that these spin components are what we can actually compute directly from the approximate ladder. As shown in appendix A.1 the physical response functions are a linear combination of the spin components, and we do not want that linear combination to hide or disguise potential differences between the ED results and the ladder.

As explained at the end of section 6.2, the contribution to $\chi^{(2)}_{\text{vertex}}$ from the approximate ladder is computed in $\text{ph}_{\overline{a}}$ notation. However, for better consistency and comparability all results shown in this section use the same frequency notation as in chapter 5 (see fig. 5.1).

Figure 6.15 compares the ED and ladder results of spin components $\uparrow\uparrow\uparrow$ and $\uparrow\uparrow\downarrow$ of $\chi^{(2)\,\omega_1\omega_2}_{\text{vertex}}$ for different values of the on-site Coulomb interaction U. We only plot the real parts since, as expected from the discussion at the end of section 6.2, the imaginary parts are at least seven orders of magnitude smaller than the real parts and therefore practically zero. The static values of the second-order response functions, i.e. those at $\omega_1 = \omega_2 = 0$, are much larger (by magnitude) than the other frequency components and would dominate the plot. Therefore, they are cut off from the color bars and instead shown in table 6.1.

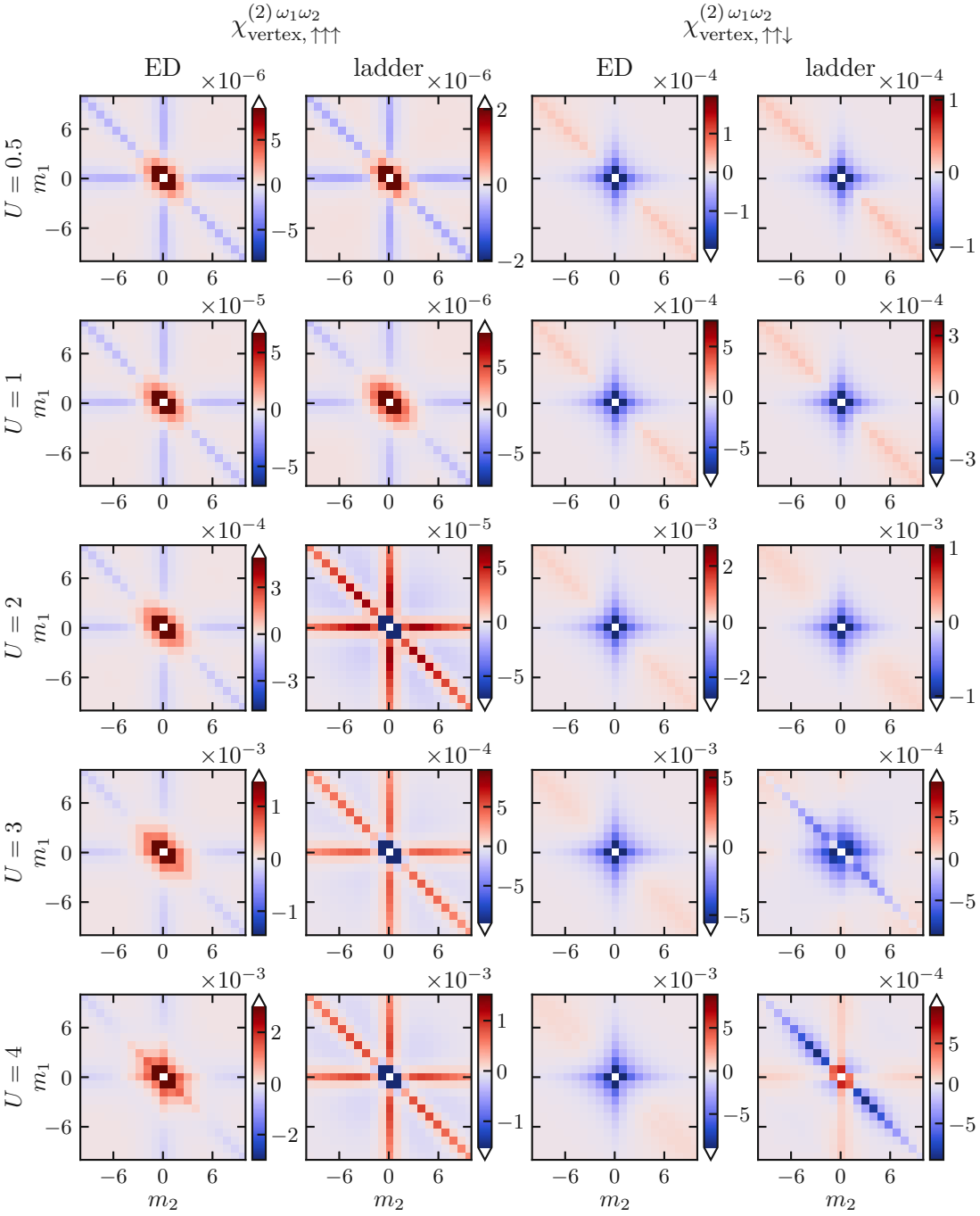

Figure 6.15.: Comparison of spin component $\uparrow\uparrow\uparrow$ and $\uparrow\uparrow\downarrow$ of $\chi^{(2)\,\omega_1\omega_2}_{\text{vertex}}$ between ED and the approximate ladder for different values of the interaction U. The labels m_i are the indices of the bosonic frequencies $\omega_i = 2\pi m_i/\beta$. The static values ($\omega_1 = \omega_2 = 0$) are much larger than the other frequency components, so they are cut off from the color bars and instead shown in table 6.1.

Table 6.2.: Static values ($\omega_1 = \omega_2 = 0$) of $\chi^{(2)}_{L,r,\uparrow\uparrow\uparrow}$ cut off from the color bars of fig. 6.17

	$\chi^{00}_{L,r,\uparrow\uparrow\uparrow}$					
U	$r = 41$	$r = 23$	$r = 65$	$r = 25$	$r = 45$	$r = 21$
1.0	-3.3×10^{-4}	-3.3×10^{-4}	-3.3×10^{-4}	2.6×10^{-4}	2.6×10^{-4}	2.6×10^{-4}
2.0	-4.4×10^{-3}	-4.4×10^{-3}	-4.4×10^{-3}	1.2×10^{-3}	1.2×10^{-3}	1.2×10^{-3}

The first thing we see when looking at fig. 6.15 is that the approximate ladder yields qualitatively good results only for small values of the interaction. For the $\uparrow\uparrow\uparrow$ component this is until $U = 1$; for the $\uparrow\uparrow\downarrow$ component it is until $U = 3$. Even then, however, the results are off by a factor of two to ten, so quantitatively the approximate ladder is rather bad.

Figure 6.16 compares the real and imaginary parts of the ED and ladder results of spin component $\uparrow\overline{\uparrow\downarrow}$ of $\chi^{(2)\omega_1\omega_2}_{\text{vertex}}$ for different values of the interaction U. Similar to spin component $\uparrow\uparrow\uparrow$ the approximate ladder only yields qualitatively good results until $U = 1$ – at least for the real parts. The imaginary parts look fine for all values of U. However, looking at the color bars reveals that quantitatively the ladder results for spin component $\uparrow\overline{\uparrow\downarrow}$ are just as bad as those for the others.

The fact that for all spin components, the qualitatively good-looking results are consistently too small is no surprise. After all, we average over all nine pph channels instead of summing. Of course, as we have shown at the end of section 6.2, summing would overcount diagrams with few vertices, but we conjecture that ladder terms of high enough order, i.e., number of vertices, are exclusive to a channel. Averaging therefore cuts down higher order contributions by a factor of nine.

6.3.3. The approximate ladder in different channels

In this section we take a closer look at the contributions of the different pph channels r to the second-order response function computed only from the approximate ladder L, i.e.,

$$\chi^{\omega_1\omega_2}_{L,r} = \sum_{\nu_1\nu_2\nu_3} L_r^{\nu_1\omega_1\nu_2\omega_2\nu_3}. \tag{6.38}$$

We already pointed out at the end of section 6.2 that six of the nine channels form mirror pairs. These pairs have the same real part but opposing imaginary parts, which all cancel eventually. Therefore, only six channels are of interest. Figure 6.17 compares the spin component $\uparrow\uparrow\uparrow$ of the real parts of $\chi^{\omega_1\omega_2}_{L,r}$ in six such channels at interaction strengths $U = 1$ and $U = 2$. As in fig. 6.15 the static frequency components ($\omega_1 = \omega_2 = 0$) would dominate the plot and are therefore cut off and presented separately in table 6.2.

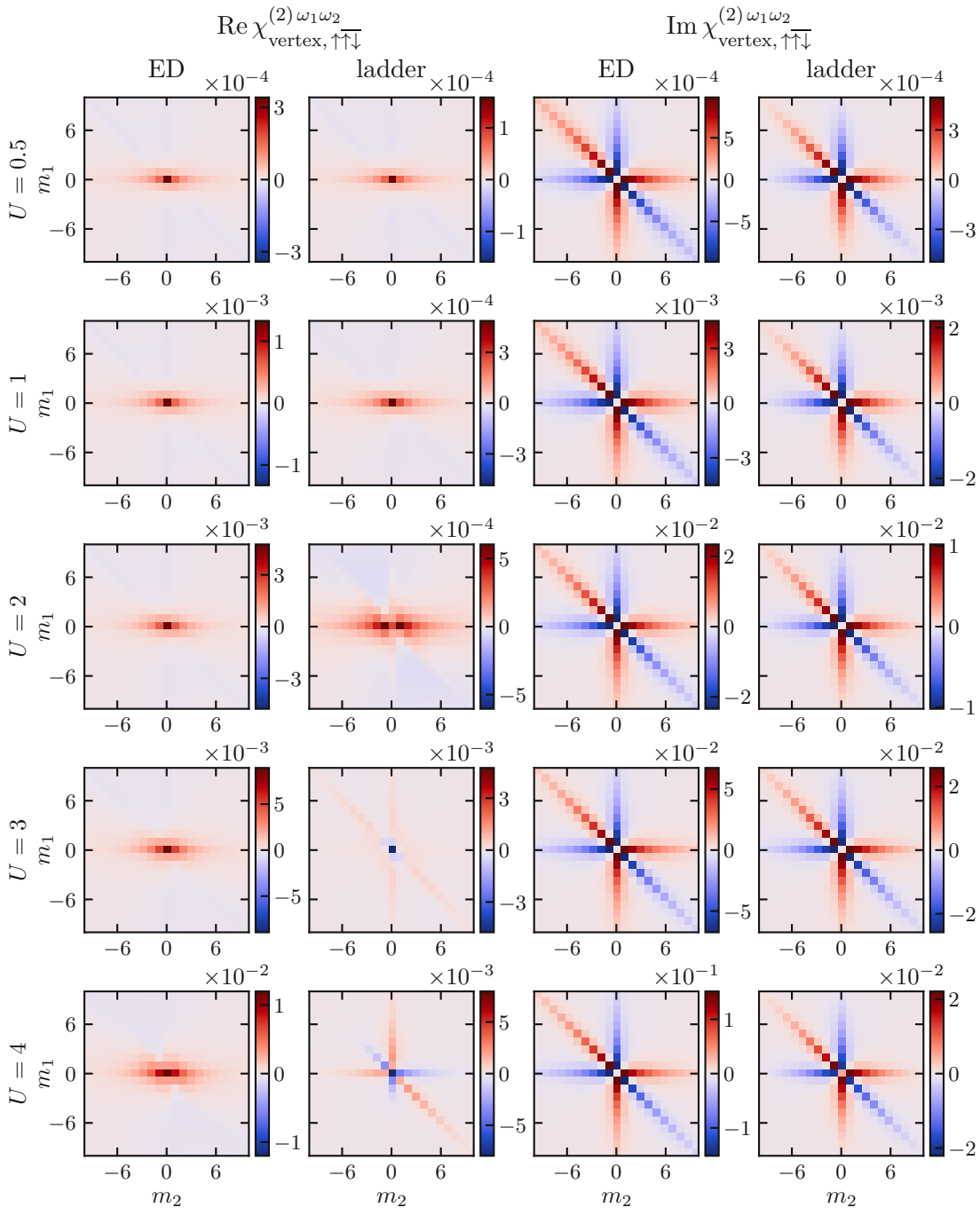

Figure 6.16.: Comparison of the real and imaginary parts of spin component $\uparrow\uparrow\downarrow$ of $\chi^{(2)\,\omega_1\omega_2}_{\text{vertex}}$ between ED and the approximate ladder for different values of the on-site Coulomb interaction U. The axis labels m_i are the indices of the bosonic frequencies $\omega_i = 2\pi m_i/\beta$.

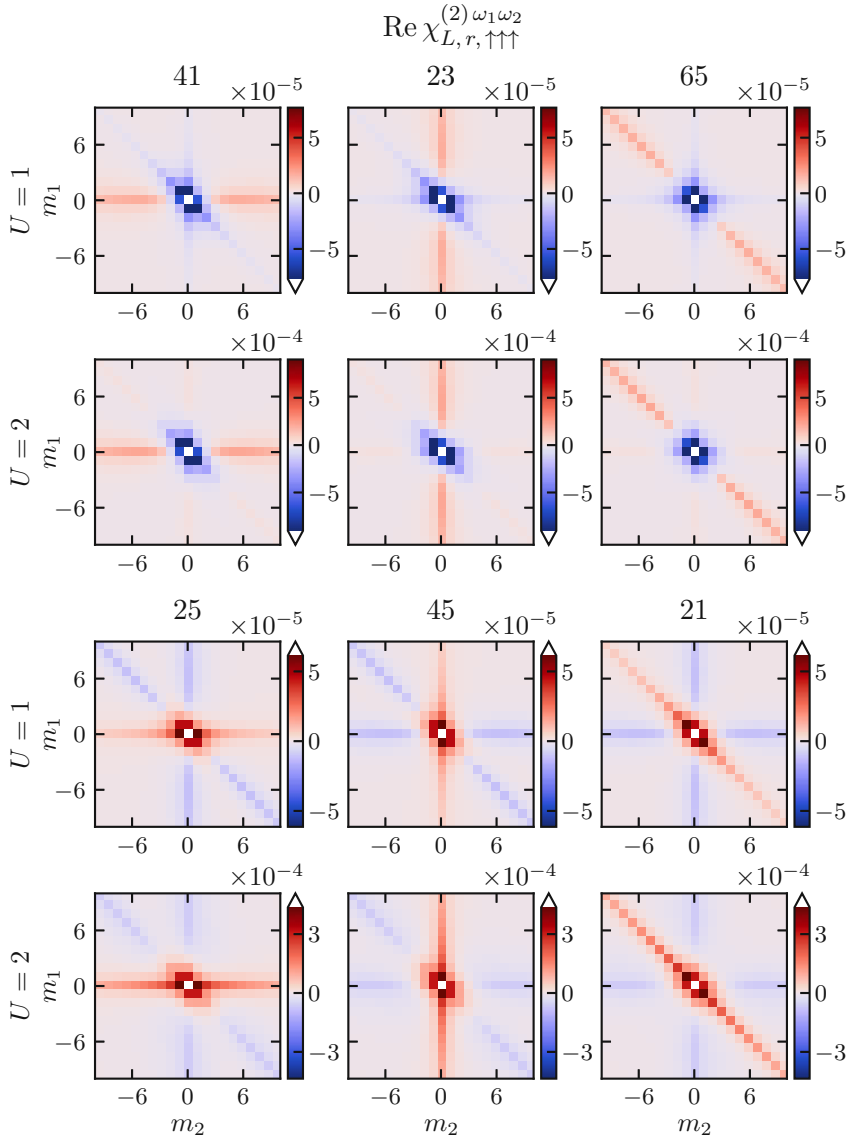

Figure 6.17.: Comparison of the contributions of the approximate ladder L in six pph channels $r \in \{41, 23, 65, 25, 45, 21\}$ to the $\uparrow\uparrow\uparrow$ component of the second-order response function $\chi^{(2)\,\omega_1\omega_2}_{L,r}$ for Coulomb interactions $U = \{1, 2\}$. The labels m_i are the indices of the bosonic frequencies $\omega_i = 2\pi m_i/\beta$. As in fig. 6.15, the static components ($\omega_1 = \omega_2 = 0$) are cut off and shown in table 6.2 instead.

When looking at fig. 6.17 we see that all results share two features: First, the main contributions are around the center; second, one of the three lines $\omega_i = 0$, $i \in \{1, 2, 3\}$, is more pronounced than the others. The latter is not surprising, since the Feynman diagrams for a single ladder have a distinguished direction. This also highlights once more why averaging over the approximate ladders in all channels is important if we want the get the right structure of the three-particle vertex.

We also see that the contributions from the upper and lower three channels in fig. 6.17 have opposite signs. For $U = 1$ they even have a very similar magnitude. However, since for each of the lower three channels there is a second one with the same real part, those contributions outweigh the upper three channels. The final result for $\chi^{(2)}_{\text{vertex},\uparrow\uparrow\uparrow}$ at $U = 1$ shown in fig. 6.15 has therefore positive values around the center.

When comparing the results between $U = 1$ and $U = 2$ in fig. 6.17 we notice that while the plots still look qualitatively similar, the balance in magnitude shifts. The static frequency components in table 6.2 show this best. While the values for the first three channels rise by a factor of more than ten, those of the last three channels only rise by a factor of less than five. In absolute terms, the channels 41, 23, and 65 now outweigh the other channels by a factor of more than three. Therefore, the sign of the total result for $\chi^{(2)}_{\text{vertex},\uparrow\uparrow\uparrow}$ shown in fig. 6.15 changes at $U = 2$.

6.4. Conclusion and outlook

We have generalized the Bethe–Salpeter equations from two to three particles. However, due to the increased complexity of three-particle diagrams when it comes to the property of reducibility, the resulting equations are much more involved than on the two-particle level. Also, the building blocks of the exact three-particle ladder are more complicated, and we do not yet have a feasible way of computing them. For this reason we have derived an approximate ladder, built simply from irreducible two-particle vertices Γ and full Green's functions. Admittedly, even this approximation turned out to be more complex than initially expected, but it finally yields a viable way for (approximately) computing the full three-particle vertex F_3.

The numerical computations show that the approximate ladder only yields qualitatively good results for very small values of the local Coulomb interaction U – at least at the investigated parameters. There might be parameter regimes where the approximation is generally better, or where we do not have to average over ladders in all nine channels because the physics happens predominantly in one "direction". One could in general look more closely at the averaging over the pph channels. Maybe there is a better way to avoid the overcounting issues that arise from the summation. As mentioned in section 6.3.2 overcounting might only be a problem up to a certain order, i.e., number of two-particle vertices in the ladder term.

In the end, computing three-particle vertices is still in its very early stages of development. So while the current results fall short of expectations, they are still useful and a good first step that can be built upon.

7. Statistical error estimation with jackknife

Parts of this chapter marked with a vertical bar have already been published in Kappl et al. [91]. Minor modifications of the notation were made to better match the rest of the thesis.

We employ the jackknife algorithm to analyze the propagation of the statistical quantum Monte Carlo (QMC) error through the Bethe–Salpeter equation. This allows us to estimate the error of dynamical mean-field theory (DMFT) calculations of the susceptibility and of dynamical vertex approximation (DΓA) calculations of the self-energy. We find that the different frequency components of the susceptibility are uncorrelated, whereas those of the self-energy are correlated. For improving the quality of the correlation matrix taking sufficiently many jackknife bins is key, while for reducing the standard error of the mean sufficiently many Monte Carlo measurements are necessary. We furthermore show that even in the case of the self-energy, the finite covariance does not have a sizable influence on the analytic continuation.

7.1. Introduction

Developing reliable theories for strong electronic correlation has proved a Herculean task. Three decades after its invention[35, 56, 92], DMFT has become state-of-the-art to calculate strongly correlated models[37] and materials[34, 39, 93–95]. Notwithstanding, one of the core scientific tasks, namely providing a proper error estimate for such calculations, is still in its infancy. Error estimates which directly follow from the QMC simulation of the (self-consistently determined) DMFT impurity problem, e.g. for the magnetization or compressibility, have been provided already from the beginning of DMFT, see, e.g., refs. [56, 96, 97]. But as the focus of such calculations is nowadays more on the one-particle spectral function or two-particle susceptibility, error estimates are by and large missing.

This is because such an error estimate is nontrivial. First, calculating the spectrum or susceptibility requires complex, nonlinear post-processing routines such as a maximum entropy analytic continuation or the Bethe–Salpeter equation, respectively. Besides proper error propagation through these post-processing procedures, there is, secondly, the iteration error, i.e., the difference between the numerical solution and the exact

(true) DMFT fixed point. Third, DMFT is an approximation to the correlation problem itself, introducing a systematic error for finite dimensional systems.

The latter, i.e., the error of DMFT as an approximation, can be systematically improved upon by either cluster[98] or diagrammatic extensions[18]. Cluster extensions replace the single impurity site with a small cluster, thus interpolating between DMFT and the full lattice problem. Given proper finite size scaling, enlarging the cluster then yields an error estimate. The huge numerical effort essentially restricts such cluster extensions however to small clusters on one- and two-dimensional lattices.

Diagrammatic extensions, on the other hand, augment DMFT with a specific set of nonlocal Feynman diagrams. The DΓA [47, 53], a prominent diagrammatic extension, generalizes the concept of a local one-particle vertex (self-energy) in DMFT systematically to the two-, three-, n-particle vertex. For $n \to \infty$ one recovers the full problem. The corrections on the two-particle vertex level provide an error estimate for the DMFT approximation, and similarly those of the three-particle level as an error estimate for the DΓA results on the two-particle vertex level. One can proceed in a similar fashion of approximating the error[3] in the dual Fermion approach[51]. Since both the size of the vertices and the effort of the associated diagrammatic equations grow strongly in n, one is restricted to small n.

In this paper, we focus on the error propagation through the post-processing procedure, specifically, the Bethe–Salpeter equation. This does not only involve the DMFT calculation of the susceptibility but also the DΓA calculation of the self-energy which employs the same Bethe–Salpeter equation, and on top of that the Schwinger–Dyson equation. Input for both equations is the local two-particle Green's function and the properly converged DMFT one-particle Green's function. For multi-orbital systems or at low temperatures the two-particle Green's function is only accessible using QMC techniques, but requires quite some effort to calculate and hence has a substantial statistical QMC error. We employ the jackknife method [99, 100] to analyze the propagation of the QMC error through the Bethe–Salpeter equation and to estimate the error of the final DMFT susceptibility and DΓA self-energy. Finally, we perform maximum entropy analytic continuations of the DΓA self-energy, using the jackknife estimates for error and covariance.

The remainder of the paper is organized as follows: section 7.2 describes the methods employed: DMFT, continuous-time quantum Monte Carlo, AbinitioDΓA, and jackknife resampling. The input to our calculations, the two-particle Green's function, is analyzed in section 7.3. The main results for the DΓA self-energy and the DMFT susceptibilities are presented in sections 7.4 and 7.5 respectively, while an analytical continuation of the DΓA self-energy is done in section 7.6. A discussion and conclusion can be found in section 7.7.

7.2. Methods

In the following, we briefly recapitulate the essential steps for calculating the DMFT susceptibility and DΓA self-energy, starting from the QMC calculation of the one- and two-particle Green's function. We restrict ourselves to the essential equations without discussing technical details such as reformulations of the equations or numerical efficiency. For these details we refer the reader to ref. [82] as regards the QMC calculation with the w2dynamics package [82] and to ref. [101] for a general review, to refs. [19, 102] as regards the calculation of the DMFT susceptibility and DΓA self-energy with the ab initio dynamical vertex approximation (ADGA) package, and to ref. [18] for a review. Further, we discuss the essential idea of the jackknife algorithm, again referring the reader to the review ref. [100] for a more detailed presentation.

7.2.1. Dynamical mean-field theory

In DMFT, we map the lattice model

$$H_{\text{lattice}} = U \sum_i \hat{c}^\dagger_{i\uparrow}\hat{c}^\dagger_{i\downarrow}\hat{c}_{i\downarrow}\hat{c}_{i\uparrow} + \sum_{\sigma,i,j} t_{ij}\hat{c}^\dagger_{i\sigma}\hat{c}_{j\sigma}, \tag{7.1}$$

where $\hat{c}_{i\sigma}$ annihilates a fermion of spin σ on site i, U is the on-site interaction, and t_{ij} is the hopping matrix, onto an Anderson impurity model (AIM)[56, 92]:

$$H_{\text{AIM}} = U\hat{c}^\dagger_\uparrow\hat{c}^\dagger_\downarrow\hat{c}_\downarrow\hat{c}_\uparrow + \sum_\sigma \tilde{\epsilon}_\sigma \hat{c}^\dagger_\sigma\hat{c}_\sigma + \underbrace{\sum_{\sigma,p}(V_p\hat{c}^\dagger_\sigma\hat{f}_{\sigma p} + V_p^*\hat{f}^\dagger_{\sigma p}\hat{c}_\sigma)}_{H_{\text{hyb}}} + \sum_p \epsilon_p \hat{f}^\dagger_{\sigma p}\hat{f}_{\sigma p}. \tag{7.2}$$

Here U is the impurity interaction which is the same as that of the original lattice problem; V_p denotes the hybridization between the impurity (denoted by $\hat{c}^\dagger_\sigma$ and $\hat{c}_\sigma$ creation and annihilation operators for spin $\sigma \in \{\uparrow,\downarrow\}$) and bath site p (denoted by corresponding $\hat{f}^\dagger_{\sigma p}$ and $\hat{f}_{\sigma p}$ operators) at energy ϵ_p. In essence, DMFT determines an AIM that gives the same local one-particle physics as the lattice model where the corresponding parameters V_p and ϵ_p (or the hybridization function Δ) have to be determined self-consistently[56, 92]. In what follows we assume that this DMFT self-consistency has been achieved to high accuracy. For the sake of simplicity, we have restricted the equations to the one-orbital problem, but the generalization to multi-orbital models is straightforward.

7.2.2. Continuous-time quantum Monte Carlo

In order to obtain the one- and two-particle Green's function for the AIM (7.2), we use continuous-time quantum Monte Carlo in the hybridization expansion (CT-HYB)[46, 101] with worm sampling[103] as implemented in the w2dynamics package[82, 104]. CT-HYB with worm sampling proceeds in a three-step fashion: First, one splits the Hamiltonian H into an interacting part, taken to be $H_I = H_{\text{hyb}}$, and the rest, H_0. Second, one expands both the partition function and the expectation value of some

observable ("worm" $\mathcal{W}$) into a Dyson series with respect to H_I and uses Wick's theorem to group diagrams into determinants. For the partition functions, this yields:

$$\mathcal{Z} = \sum_{n=0}^{\infty} \frac{(-1)^n}{n!} \sum_{\sigma_1,\sigma_1'} \cdots \sum_{\sigma_n,\sigma_n'} \int_0^\beta \mathrm{d}^n\tau \mathrm{d}^n\tau' \, \mathrm{Tr}\left[\mathrm{T}\, \mathrm{e}^{-\beta H_{\mathrm{loc}}} \prod_{i=1}^{n} \hat{c}^\dagger_{\sigma_i}(\tau_i)\, \hat{c}_{\sigma_i'}(\tau_i') \right] \det \underline{\underline{\Delta}}, \quad (7.3)$$

where T denotes time ordering. The elements of the hybridization matrix $\underline{\underline{\Delta}}$ are given by $\underline{\underline{\Delta}}_{ij} = \Delta_{\sigma_i\sigma_j'}(\tau_i - \tau_j')$ with the hybridization function $\Delta_{\sigma\sigma'}(\tau) = \delta_{\sigma\sigma'} \sum_p V_p (\partial_\tau - \epsilon_p)^{-1} V_p^*$.

Similarly, we write down the hybridization expansion for the *worm* operator $\mathcal{W}(\{\tilde{\tau}\})$. It can consist of several creation and annihilation operators with various number of time arguments. Most important examples are the one- and two-particle Green's function, where $\mathcal{W}(\{\tilde{\tau}\})$ stands for $\mathrm{T}\, \hat{c}_\sigma(\tau)\hat{c}^\dagger_\sigma(\tau')$ and $\mathrm{T}\, \hat{c}_\sigma(\tau_1)\hat{c}^\dagger_\sigma(\tau_2)\hat{c}_\sigma(\tau_3)\hat{c}^\dagger_\sigma(\tau_4)$, respectively. Other worm operators have been introduced in refs. [77, 79, 105]. For the sampling space of $\mathcal{W}(\{\tilde{\tau}\})$, we thus get:

$$\mathcal{Z}_{\mathcal{W}} = \sum_{n=0}^{\infty} \frac{(-1)^n}{n!} \sum_{\sigma_1,\sigma_1'} \cdots \sum_{\sigma_n,\sigma_n'} \int_0^\beta \mathrm{d}^n\tau \mathrm{d}^n\tau' \, \mathrm{d}\{\tilde{\tau}\} \times \mathrm{Tr}\left[\mathrm{T}\, \mathrm{e}^{-\beta H_{\mathrm{loc}}} \mathcal{W}(\{\tilde{\tau}\}) \prod_{i=1}^{n} \hat{c}^\dagger_{\sigma_i}(\tau_i)\, \hat{c}_{\sigma_i'}(\tau_i') \right] \det \mathbf{\Delta}. \quad (7.4)$$

Third, we combine both sampling spaces by taking the abstract sum $\mathcal{Z} + \eta\mathcal{Z}_{\mathcal{W}}$, where η is a balancing parameter. The resulting space is sampled using Markov chain Monte Carlo.

An estimator for the worm operator $\mathcal{W}(\{\tilde{\tau}\})$ is then simply given by:

$$\langle \mathcal{W}(\{\tilde{\tau}\}) \rangle = \frac{\mathcal{Z}_{\mathcal{W}}}{\mathcal{Z}} \langle \sigma(\{\tilde{\tau}\}) \rangle \,, \quad (7.5)$$

where $\sigma(\{\tau_i\})$ is the indicator function of a configuration in $\mathcal{Z}_{\mathcal{W}}$ with the matching times, $\mathcal{Z}_{\mathcal{W}}/\mathcal{Z}$ is the ratio of volumes between the two spaces. Let us note that in the case of the one- or two-particle Green's function one worm measurement is computationally cheaper than one measurement of the removal estimator in Z-sampling, but it also yields less information.

7.2.3. DMFT susceptibility

In the following, we will make the transition from imaginary time to Matsubara frequencies, where the one-particle Green's function is

$$G_\sigma^\nu = \int_0^\beta \mathrm{d}\tau \mathrm{e}^{\mathrm{i}\nu(\tau)} \langle \mathrm{T}\, \hat{c}_\sigma(\tau) \hat{c}_\sigma^\dagger(0) \rangle \tag{7.6}$$

and the two-particle Green's function is

$$G_{2,\sigma\sigma'}^{\nu\nu'\omega} = \frac{1}{\beta} \int_0^\beta \mathrm{d}\tau_1 \, \mathrm{d}\tau_2 \, \mathrm{d}\tau_3 \, \mathrm{e}^{\mathrm{i}[\nu\tau_1 - (\nu+\omega)\tau_2 + (\nu'+\omega)\tau_3]} \langle \mathrm{T}\, \hat{c}_\sigma(\tau_1) \hat{c}_\sigma^\dagger(\tau_2) \hat{c}_{\sigma'}(\tau_3) \hat{c}_{\sigma'}^\dagger(0) \rangle . \tag{7.7}$$

Note that here and in the following we use the notation of the w2dynamics code [82] which has the extra $1/\beta$ factor in the definition of the two-particle Green's function (7.7) compared to ref. [18]. From these Green's functions, we can calculate the generalized local susceptibility

$$\chi_{\sigma\sigma'}^{\nu\nu'\omega} = \beta G_{2,\sigma\sigma'}^{\nu\nu'\omega} - \beta G_\nu G_{\nu'} \delta_{\omega 0}. \tag{7.8}$$

Diagrammatically, the above equation means that we remove one disconnected contribution from G_2. In the presence of SU(2) symmetry, i.e., in the paramagnetic phase, one can further restrict oneself to the following two spin combinations, also referred to as density (d) and magnetic (m) channel.

$$\chi_{d/m,}^{\nu\nu'\omega} = \chi_{\uparrow\uparrow}^{\nu\nu'\omega} \pm \chi_{\uparrow\downarrow}^{\nu\nu'\omega} \, . \tag{7.9}$$

From the local susceptibility $\chi_r^{\nu\nu'\omega}$ with $r \in \{d, m\}$ and the local bare bubble susceptibility $\chi_0^{\nu\nu'\omega} = -\beta G_\nu G_{(\nu+\omega)} \delta_{\nu\nu'}$, we can determine the local irreducible vertex through an inversion of the local Bethe–Salpeter equation

$$\Gamma_r = \chi_r^{-1} - \chi_0^{-1} \, . \tag{7.10}$$

This equation is diagonal with respect to each bosonic frequency ω while the inversion itself is performed in the implicit matrix notation ν and ν'. From Γ and the local particle-hole bubble $\chi_{0,\mathbf{k}\mathbf{k}'\mathbf{q}}^{\nu\nu'\omega} = -\beta G_{\mathbf{k}\nu} G_{(\mathbf{k}+\mathbf{q})(\nu+\omega)} \delta_{\nu\nu'} \delta_{\mathbf{k}\mathbf{k}'}$ the lattice Bethe–Salpeter equation now allows us to calculate the generalized DMFT lattice susceptibility

$$\chi_{r,\mathbf{k}\mathbf{k}'\mathbf{q}}^{\nu\nu'\omega} = \chi_{0,\mathbf{k}\mathbf{k}'\mathbf{q}}^{\nu\nu'\omega} - \sum_{\substack{\nu_1\nu_2 \\ \mathbf{k_1}\mathbf{k_2}}} \chi_{0,\mathbf{k}\mathbf{k_1}\mathbf{q}}^{\nu\nu_1\omega} \Gamma_r^{\nu_1\nu_2\omega} \chi_{r,\mathbf{k_2}\mathbf{k}'\mathbf{q}}^{\nu_2\nu'\omega}. \tag{7.11}$$

Here and in the following, we distinguish lattice and local quantities through the additional momentum indices $\mathbf{k}$, $\mathbf{k}'$, $\mathbf{q}$; and implicitly assume a factor $1/\beta$ for each Matsubara frequency sum, as in ref. [18]. That is, $\sum_{\nu_1}$ actually means $\frac{1}{\beta}\sum_{\nu_1}$. From these, physical susceptibilities at frequency ω and momentum $\mathbf{q}$ can be calculated through summing over ν, ν', $\mathbf{k}$, $\mathbf{k}'$.

7.2.4. AbinitioDΓA self-energy

Similar to eq. (7.11), we can also calculate the full vertex F through the Bethe–Salpeter equation

$$F^{\nu\nu'\omega}_{r,\mathbf{k}\mathbf{k}'\mathbf{q}} = \Gamma^{\nu\nu'\omega}_{r} + \sum_{\substack{\nu_1\nu_2\\ \mathbf{k_1}\mathbf{k_2}}} \Gamma^{\nu\nu_1\omega}_{r} \chi^{\nu_1\nu_2\omega}_{0,\mathbf{k_1}\mathbf{k_2}\mathbf{q}} F^{\nu_2\nu'\omega}_{r,\mathbf{k_2}\mathbf{k}'\mathbf{q}}. \tag{7.12}$$

However, in the ladder approximation the resulting F from Equation (7.12) simplifies further and does not have an explicit dependence on $\mathbf{k}$ and $\mathbf{k}'$:

$$F^{\nu\nu'\omega}_{r,\mathbf{q}} = \Gamma^{\nu\nu'\omega}_{r} + \sum_{\nu_1\nu_2} \Gamma^{\nu\nu_1\omega}_{r} \chi^{\nu_1\nu_2\omega}_{0,\mathbf{q}} F^{\nu_2\nu'\omega}_{r,\mathbf{q}}. \tag{7.13}$$

Here we defined $\chi^{\nu\nu'\omega}_{0,\mathbf{q}} = \sum_{\mathbf{k},\mathbf{k}'} \chi^{\nu\nu'\omega}_{0,\mathbf{k}\mathbf{k}'\mathbf{q}}$. Please note that the generated nonlocal full vertices F in Equation (7.13) are no longer crossing symmetric. By taking into account the corresponding diagrams in the transversal particle–hole channel we get for the density component

$$F^{\nu\nu'\omega}_{d,\mathbf{k}\mathbf{k}'\mathbf{q}} = F^{\nu\nu'\omega}_{d,\mathbf{q}} + \frac{1}{2} F^{\mathrm{nl}\ (\nu'-\nu)(\nu'-\omega)\nu'}_{d,\mathbf{k}'-\mathbf{k}} + \frac{3}{2} F^{\mathrm{nl}\ (\nu'-\nu)(\nu'-\omega)\nu'}_{m,\mathbf{k}'-\mathbf{k}} \tag{7.14}$$

where we defined $F^{\mathrm{nl}\,\nu\nu'\omega}_{r,\mathbf{q}} = F^{\nu\nu'\omega}_{r,\mathbf{q}} - F^{\nu\nu'\omega}_{r}$. From this vertex we can calculate the DΓA self-energy

$$\Sigma_{\mathbf{k}\nu} = \frac{Un}{2} - U \sum_{\substack{\nu'\omega\\ \mathbf{k}'\mathbf{q}}} F^{\nu\nu'\omega}_{d,\mathbf{k}\mathbf{k}'\mathbf{q}} G_{\mathbf{k}'\nu'} G_{(\mathbf{k}'+\mathbf{q})(\nu'+\omega)} G_{(\mathbf{k}+\mathbf{q})(\nu+\omega)}, \tag{7.15}$$

where n is the electron density entering in the Hartree term. The actual calculations for both the DMFT susceptibility and the DΓA self-energy are done using the ADGA program package which together with further computational details is discussed in refs. [19, 102].

7.2.5. Jackknife

The jackknife is a resampling method, used for bias reduction and error estimation. It is a versatile method for a range of problems, hence the name [99, 100].

Before we describe the jackknife in detail, let us recapitulate some statistical terms that we will need later on. Let θ be the true, yet unknown, value of some quantity. To access θ we construct an estimator, $\hat{\theta}$, which is a function of n random variables, $X_1, \ldots, X_n$. In our case X_i are just Monte Carlo measurements. The bias of the estimator $\hat{\theta}$ is then given by the difference between its expectation value $\mathrm{E}[\hat{\theta}]$ and the true value θ,

$$\mathrm{bias}[\hat{\theta}] := \mathrm{E}[\hat{\theta}] - \theta. \tag{7.16}$$

For $\hat{\theta}$ to be useful, its bias must be systematically improvable by increasing the sample size n. More specifically, a sequence of estimators $\{\hat{\theta}_n(X_1, \dots, X_n)\}$ is called *consistent* with θ if and only if the probability of deviating from θ goes to zero with n, i.e.,

$$\lim_{n\to\infty} \Pr(|\hat{\theta}_n(X_1, \dots, X_n) - \theta| > \epsilon) = 0, \quad \forall \epsilon > 0. \tag{7.17}$$

Now let us explain jackknife resampling based on the following general problem. Assume we want to calculate some quantity $y = f(x)$, where f is some arbitrary, known function. If we knew the true value of x the task would be trivial. In our case, however, x is a random variable, and we only have access to a sample $\{x_i\}$ of size n. Therefore, we need to find a good estimator $\hat{y}$ and be able to quantify its error. In sections 7.4 and 7.5 the input samples x_i are the two-particle Green's functions from QMC calculations, y is either the DΓA self-energy or the DMFT susceptibility, f is given by the Bethe–Salpeter equation and in case of the self-energy also by the Schwinger–Dyson equation.

For simplicity, we only propagate the error in the two-particle Green's function. This is justified, because the one-particle Green's function is calculated by symmetric improved estimators and thus its error is smaller by several orders of magnitude[79].

The general strategy of resampling techniques is to generate subsamples from the initial one which are preferably independent and identically distributed. With this, one can then estimate certain statistics of the sample like its mean or variance. In case of the jackknife a bias estimation and reduction is also possible. To show this, let $\hat{y}_n$ be a consistent estimator function for y. A common choice that we used for all calculations in this paper is

$$\hat{y}_n(x_1, \dots, x_n) = f(\bar{x}), \tag{7.18}$$

where f is the function from the original problem and $\bar{x}$ is the input sample mean. The latter is an unbiased, consistent estimator for x. If f is a continuous function, it is easy to see that $f(\bar{x})$ is a consistent estimator for y. We note that if f is linear, then $f(\bar{x})$ is already unbiased.

After choosing $\hat{y}_n$ we generate n leave-one-out samples

$$y_{-i} = \hat{y}_{n-1}(x_1, \dots, x_{i-1}, x_{i+1}, \dots, x_n). \tag{7.19}$$

Note that this simple choice of resampling implies that the leave-one-out samples are also consistent estimators for y and carry a different but similar bias. The reason why this is important for obtaining a bias-corrected estimator will become clearer in the following. Consistency requires the bias to vanish in the limit of $n \to \infty$. Thus, if f is

not only continuous but also analytic around the true value x, we can expand the bias of $\hat{y}_n$ in powers of $1/n$ and write

$$\text{bias}[\hat{y}_n] = \frac{a}{n} + \frac{b}{n^2} + O(n^{-3}), \tag{7.20}$$

$$\text{bias}[y_{-i}] = \text{bias}[\hat{y}_{n-1}] = \frac{a}{n-1} + \frac{b}{(n-1)^2} + O(n^{-3}), \tag{7.21}$$

with some a and b. The expectation value as well as the bias are linear operators [see eq. (7.16)]. It is therefore easy to construct new samples y_i' in such a way that we get rid of the leading $O(1/n)$ term in the bias

$$y_i' = n\hat{y}_n - (n-1)y_{-i}, \tag{7.22}$$

$$\begin{aligned} \text{bias}[y_i'] &= n\,\text{bias}[\hat{y}_n] - (n-1)\,\text{bias}[y_{-i}] \\ &= \left(a + \frac{b}{n}\right) - \left(a + \frac{b}{n-1}\right) + O(n^{-3}) \\ &= -\frac{b}{n(n-1)} + O(n^{-3}) = O(n^{-2}). \end{aligned} \tag{7.23}$$

By calculating the sample mean of the y_i' we finally arrive at the bias-corrected jackknife estimator

$$\hat{y}_{\text{JK}} = \bar{y}' = \frac{1}{n}\sum_{i=1}^{n} y_i'. \tag{7.24}$$

Its expectation value is given by

$$\begin{aligned} \text{E}[\hat{y}_{\text{JK}}] &= \frac{1}{n}\sum_{i=1}^{n}\Big(\text{E}[y_i']\Big) = \frac{1}{n}\sum_{i=1}^{n}\Big(n\,\text{E}[\hat{y}_n] - (n-1)\,\text{E}[y_{-i}]\Big) \\ &= \frac{1}{n}\sum_{i=1}^{n}\Big(n(y + \text{bias}[\hat{y}_n]) - (n-1)(y + \text{bias}[y_{-i}])\Big) \\ &= \frac{1}{n}\sum_{i=1}^{n}\Big(y + \text{bias}[y_i']\Big) = y + O(n^{-2}), \end{aligned} \tag{7.25}$$

where eq. (7.23) was used in the last step. This shows that $\hat{y}_{\text{JK}}$ is a consistent estimator for y with a reduced bias of $O(1/n^2)$.

Without proof, consistent estimators for the variance, standard deviation, covariance, etc. of y can also be obtained by calculating the corresponding sample estimates of $\{y_i'\}$[106]. In sections 7.3 to 7.5 we are specifically interested in the standard error of the mean (SEM) and the linear correlation, $\text{corr}[\cdot,\cdot]$. The latter is estimated by the sample Pearson correlation coefficients r. For scalar random variables p and q with

samples $\{p_i\}$ and $\{q_i\}$ of size n the following holds

$$\mathrm{SEM}_p := \frac{s_p}{\sqrt{n}} = \sqrt{\frac{1}{n(n-1)} \sum_{i=1}^{n} |p_i - \bar{p}|^2} \tag{7.26}$$

$$\widehat{\mathrm{corr}}[p,q] = r_{pq} = \frac{\sum_{i=1}^{n} (p_i - \bar{p})(q_i - \bar{q})^*}{\sqrt{\sum_{i=1}^{n} |p_i - \bar{p}|^2} \sqrt{\sum_{i=1}^{n} |q_i - \bar{q}|^2}}. \tag{7.27}$$

Here s denotes the corrected sample standard deviation, $\bar{p}$ the sample mean of the p_i, and $\widehat{\mathrm{corr}}$ the estimated correlation. The generalization to random vectors and objects of higher rank is straightforward by componentwise application of the above formulas. In the following, p_i is a scalar component of the ith sample x_i or y_i, e.g., $p_i = (\Sigma_{\mathrm{D\Gamma A},\mathbf{k}=(0,0),\nu=\pi/\beta})_i$ might be the ith measurement of the self-energy at a fixed momentum $\mathbf{k}$ and frequency ν.

Let us note an important caveat in using eq. (7.27) as estimator for a $k \times k$ correlation matrix r_{pq} with a large number of features k: While each component of the covariance converges as $1/\sqrt{n}$ regardless of k, the eigenvalues of the covariance matrix, which are used to construct independent errors, converge only as a function of n/k. In particular, the estimator yields a singular correlation matrix for any $n < k$.

For practical use, the whole derivation and discussion of the jackknife above can be condensed into three simple steps:

1. Resample
$$x_i \to x_i' = \frac{1}{n-1} \sum_{j \neq i} x_j = \frac{n\bar{x} - x_i}{n-1} \tag{7.28}$$
2. Transform
$$y_i' = n f(\bar{x}) - (n-1) f(x_i') \tag{7.29}$$
3. Calculate sample statistics of $\{y_i'\}$, e.g., eqs. (7.24), (7.26) and (7.27)

Another statistical method, similar to the jackknife, is the bootstrap. It is more powerful but usually requires a greater number of resamples to take advantage of that[107]. Depending on the specific problem, at least hundreds or thousands of new samples are drawn for the bootstrap method[106, 108] as opposed to the 16 to 256 jackknife samples that are used in sections 7.4 and 7.5. Since each resample requires a full DΓA calculation, the jackknife is computationally cheaper and therefore the method of choice.

7.2.6. Parallel implementation

The main focus of this paper is on the jackknife estimates of the self-energy and susceptibilities calculated within ADGA. In this case the parallelization is simple,

because the ADGA calculation is by far the most computationally intensive task and already implemented in a parallel way. Therefore, the actual jackknife part is programmed in serial and only the calls to the ADGA code are done in parallel.

7.3. Statistical analysis of the input: two-particle Green's function

Before we analyze the DΓA self-energy and DMFT susceptibilities, let us take a closer look at the input of the DMFT and DΓA calculations, namely the two-particle Green's function $G_2^{\nu\nu'\omega}$. In particular, we want to check if the correlations of the self-energy and susceptibilities are completely intrinsic or if they originate at least in part from the input. For this reason we estimate $\mathrm{corr}[G_{2,\uparrow\uparrow}^{\nu_1\nu_1'\omega_1}, G_{2,\uparrow\uparrow}^{\nu_2\nu_2'\omega_2}]$ for various frequency combinations, and plot two-dimensional cuts of this high-dimensional quantity.

All QMC simulations were done for the 2D square-lattice Hubbard model (HM) at half-filling using the following parameters: $U = 4t$, $\beta = \{2/t, 4/t\}$, where the hopping amplitude $t = 1$ serves as our energy unit. The hopping matrix in eq. (7.1) is taken to permit only nearest-neighbor hopping. The number of fermionic frequencies is 40 for $\beta = 2$ and 80 for $\beta = 4$. Due to the imposed particle-hole symmetry, the two-particle Green's function and therefore also its correlation matrix is purely real. Before the latter was estimated, the total number of n_t QMC measurements were divided equally into n_b bins. The $n_m = n_t/n_b$ measurements in each bin were then averaged and used as the samples for the estimations. All results in this section were obtained with $n_m = 2.4 \times 10^6$.

In fig. 7.1 the estimated correlation of

$$G_{2,\mathrm{cut1}}(\nu_1) := G_{2,\uparrow\uparrow}^{\nu=\nu_1,\nu'=\nu_1,\omega=0} \tag{7.30}$$

with itself is shown for two temperatures $\beta = 2$ (top) and $\beta = 4$ (bottom) and two numbers of bins $n_b = 16$ (left) and $n_b = 256$ (right). Although there is quite some noise in the plots with fewer bins, the diagonal matrix structure is evident in all four graphs (note the sign of the y-axis resembling the typical arrangement in a matrix). This suggests that the two-particle Green's function is uncorrelated at different frequencies, at least along the cut.

To further test this, we next consider the estimated correlation between

$$G_{2,\mathrm{cut2}}(\omega_1) := G_{2,\uparrow\uparrow}^{\nu=0,\nu'=0,\omega=\omega_1} \tag{7.31}$$

and $G_{2,\mathrm{cut1}}$ which is shown for $\beta = 2$ in fig. 7.2 and for $\beta = 4$ in fig. 7.3. The same numbers of bins are used as before. Apart from the noise, the correlation vanishes again.

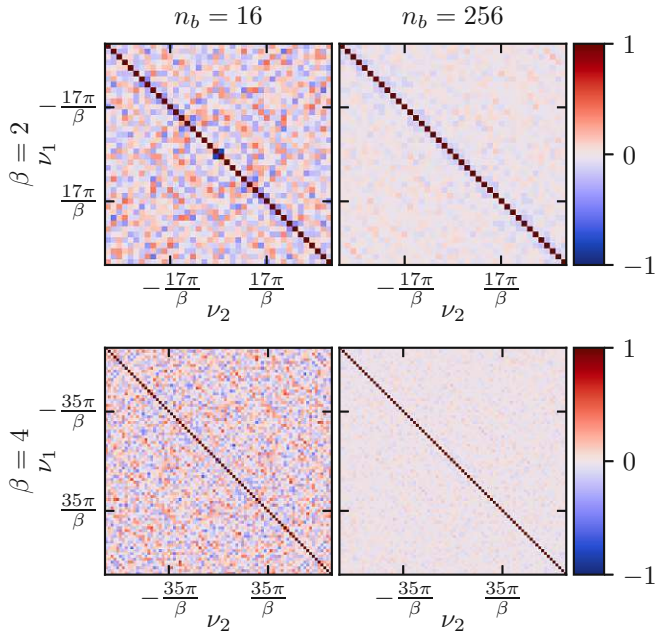

Figure 7.1.: Estimated correlation matrix $\widehat{\mathrm{corr}}[G_{2,\mathrm{cut1}}(\nu_1), G_{2,\mathrm{cut1}}(\nu_2)]$ for the two-particle Green's function at the cut $\nu = \nu' = \nu_i$, $\omega = 0$ comparing different temperatures and numbers of bins. The 40×40 matrices in the top row and the 80×80 matrices in the bottom row correspond to 40 and 80 fermionic frequencies, respectively.

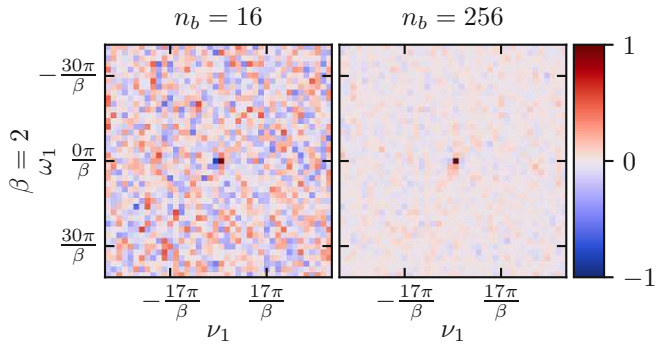

Figure 7.2.: Same as fig. 7.1 (top) but now for the estimated correlation matrix $\widehat{\mathrm{corr}}[G_{2,\mathrm{cut2}}(\omega_1), G_{2,\mathrm{cut1}}(\nu_1)]$, i.e., the correlation between cut2 with ω_1, $\nu' = \nu = 0$ and cut1 with $\omega = 0$, $\nu' = \nu = \nu_1$. The 41×40 correlation matrices correspond to 41 bosonic and 40 fermionic frequencies. As in fig. 7.1, for sufficiently many bins (right) the off-diagonal components of the correlation matrix vanish. (Note that in this figure there are no diagonal components, since there are different frequencies on the axes.)

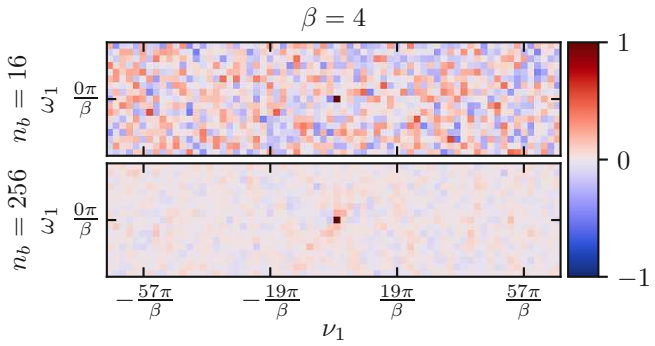

Figure 7.3.: Same as fig. 7.2 but now at $\beta = 4$. The 17×70 matrices correspond to 70 fermionic and 17 bosonic frequencies (which we reduced to save computational time as there was no measurable change in the self-energy).

Altogether, this suggests that it is reasonable to assume that the two-particle Green's function at different frequencies as calculated with QMC is uncorrelated. Since this is the input to the subsequent DMFT or DΓA calculations, any correlations of the output data must emerge through the post-processing.

7.4. Self-energy

From the local two-particle Green's function as well as the local one-particle Green's function as an input, the self-energy $\Sigma_{\mathrm{D\Gamma A},\nu\mathbf{k}}$ of the 2D square-lattice HM at half-filling is calculated in DΓA. All results in this section are generated using the same parameters as in section 7.3: $U = 4t$, $\beta = \{2/t, 4/t\}$, $t = 1$, $t' = 0$, i.e., only nearest neighbor hopping is considered. The DΓA calculations use nine bosonic as well as 40 and 80 fermionic frequencies for $\beta = 2$ and $\beta = 4$, respectively. The inner momentum-($\mathbf{k}$-)grid is 48×48 and the transfer momentum-($\mathbf{q}$-)grid is 12×12 for $\beta = 2$ and 24×24 for $\beta = 4$. Before jackknife resampling is applied, the total number n_t of QMC measurements of the two-particle Green's function is divided equally into n_b bins with $n_m = n_t/n_b$ measurements per bin which are averaged for each bin. These n_b averages are then used as the input samples for the jackknife. For a more compact notation and easier comparison of the multi panel figures in this section it is convenient to give the number of measurements as a multiple of $n_0 = 2.4 \times 10^6$.

7.4.1. Standard error of the mean

Figure 7.4 shows the imaginary part of the DΓA self-energy at $\beta = 2$ and $\beta = 4$ using 256 bins with n_0 QMC measurements each. Note that the error bars are enlarged by a factor of 500 for the left and 50 for the right plot. Taking this rescaling of the error into account, the SEM for $\beta = 4$ (right) is about 10 times higher than for $\beta = 2$ (left)

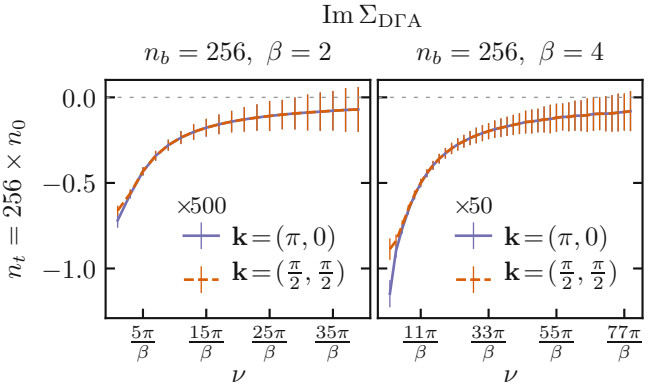

Figure 7.4.: Imaginary part and jackknife SEM of the DΓA self-energy at different temperatures. For better visibility, the errors bars are enlarged by a factor of 500 on the left and by 50 on the right.

but still very small. We do not plot the real part of the self-energy because on the Fermi surface at half-filling it is just a constant.

Since ADGA actually calculates two-particle corrections to the DMFT self-energy it is more reasonable to plot the error bars of the difference between the DMFT and DΓA self-energy, $\Sigma_{\mathrm{D\Gamma A},\mathbf{k}\nu} - \Sigma_{\mathrm{DMFT},\nu}$. In fig. 7.5 the imaginary part of this DΓA self-energy correction is plotted for $\beta = 4$ and various combinations of the total number of QMC measurements n_t and number of bins n_b. In the top (bottom) row $n_t = 16 \times n_0$ ($256 \times n_0$); in the left (right) column $n_b = 16$ (256) bins. It is obvious that the SEM scales with n_t. That is, the error for the larger number of measurements n_t (bottom row in fig. 7.5) is smaller than for a smaller n_t (top row in fig. 7.5), just as expected. However, there is practically no dependence of the error on the number of bins n_b (left vs right column of fig. 7.5). One can also see that even only $16 \times n_0 \approx 4 \times 10^7$ total measurements (top row in fig. 7.5) lead to still acceptable sizes of the error bars (note they are resized by a factor of ten).

7.4.2. Correlation matrix

Let us now turn to the correlation of the different frequency components of the DΓA self-energy. Figure 7.6 shows the real part of the estimate for the correlation of $\Sigma_{\mathrm{D\Gamma A},\mathbf{k}\nu}$ with $\Sigma_{\mathrm{D\Gamma A},\mathbf{k}\nu'}$ for $\beta = 4$ and $\mathbf{k} = (\pi, 0)$. (For the statistical analysis of the input data, we refer the reader to section 7.3.) It uses the same layout as fig. 7.5, i.e., $n_t = 16 \times n_0$ in the top row and $n_t = 256 \times n_0$ in the bottom one, with $n_b = 16$ on the left and $n_b = 256$ on the right. Contrary to the SEM, the estimated correlation matrix strongly depends on n_b as the comparison between the left and right column in fig. 7.6 shows. While increasing n_t does improve the noise slightly, a large number of jackknife samples is crucial for an acceptable noise level. It is evident in all four plots

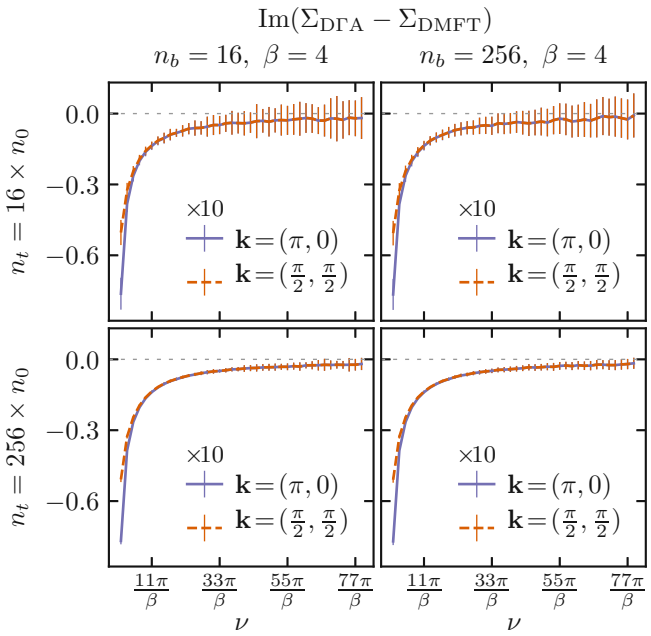

Figure 7.5.: Imaginary part and jackknife SEM of the difference between the DMFT and DΓA self-energy, $\Sigma_{\mathrm{D\Gamma A},\mathbf{k}\nu} - \Sigma_{\mathrm{DMFT},\nu}$, at $\beta = 4$. Different numbers of bins and total measurements are compared. For better visibility the error bars are enlarged by a factor of 10.

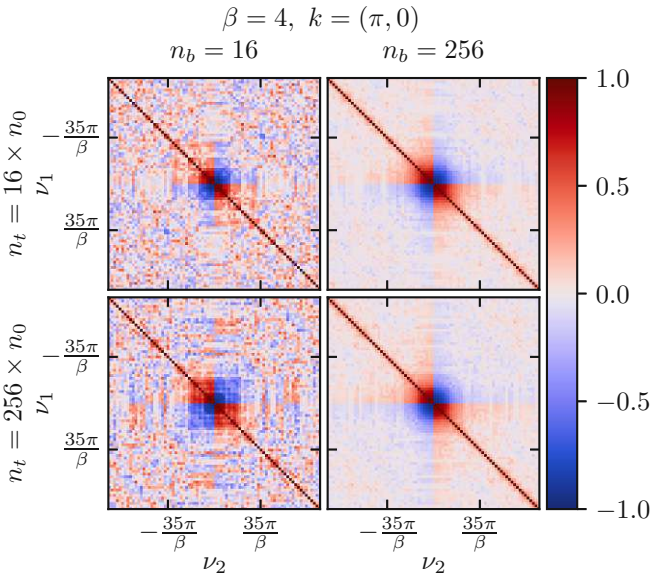

Figure 7.6.: Real part of the estimated correlation matrix $\widehat{\mathrm{corr}}[\Sigma_{\mathrm{D\Gamma A},\mathbf{k}\nu_1}, \Sigma_{\mathrm{D\Gamma A},\mathbf{k}\nu_2}]$. As in fig. 7.5 different numbers of bins and total measurements are compared. The 80×80 matrices correspond to 80 fermionic frequencies.

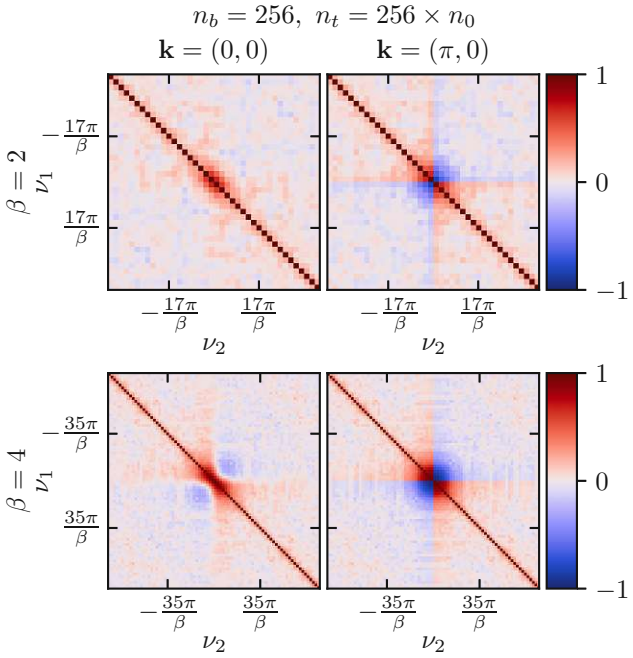

Figure 7.7.: Real part of the estimated correlation matrix $\widehat{\mathrm{corr}}[\Sigma_{\mathrm{D\Gamma A},\mathbf{k}\nu_1}, \Sigma_{\mathrm{D\Gamma A},\mathbf{k}\nu_2}]$ at different temperatures and $\mathbf{k}$-points. The 40×40 (top) and 80×80 matrices (bottom) correspond to 40 and 80 fermionic frequencies, respectively.

that the largest correlations appear in the low-frequency region. Disregarding noise, the only correlations outside of this area are those between low and high frequencies.

Figure 7.7 shows the dependence of the real part of the estimated correlation matrix on β (from the top to the bottom of fig. 7.7) and $\mathbf{k}$ (from left to right). One can see that the correlation increases slightly with increasing β (or decreasing temperature) and is also more pronounced for $\mathbf{k} = (\pi, 0)$ (right) than for $\mathbf{k} = (0, 0)$ (left). However, the general structure of the matrix – high correlation at low frequencies, very low correlation otherwise – is similar in all cases.

We do not plot the imaginary part of the estimated correlation matrix because with the chosen parameters (half-filling and $\mathbf{k}$-points on Fermi surface) it vanishes and shows only noise.

The cross-correlation between frequencies of the DΓA self-energy can be understood from Equation (7.15). It can be rewritten, such that we have the DMFT self-energy plus nonlocal corrections arising from the two-particle Green's function[19]. Both DMFT and DΓA self-energy have the same asymptotic behavior, thus nonlocal corrections have to be restricted to the lower Matsubara frequencies. Since here we consider the correlation arising from the two-particle Green's function, we can conclude that

they mainly influence the low-frequency region. Furthermore, in the model under consideration vertex corrections increase with lower temperatures, and the largest influence is to be expected at $\mathbf{k} = (\pi, 0)$, where the formation of a pseudo-gap can be observed.

The symmetries in figs. 7.6 and 7.7 can be explained by the definition of the estimated correlation coefficients and properties of the self-energy. Using eq. (7.27) and $\Sigma(\nu)^* = \Sigma(-\nu)$ yields

$$\begin{aligned} \widehat{\mathrm{corr}}[\Sigma(\nu_1), \Sigma(\nu_2)] &= \widehat{\mathrm{corr}}[\Sigma(\nu_2), \Sigma(\nu_1)]^* \\ &= \widehat{\mathrm{corr}}[\Sigma(\nu_2)^*, \Sigma(\nu_1)^*] \\ &= \widehat{\mathrm{corr}}[\Sigma(-\nu_2), \Sigma(-\nu_1)]. \end{aligned} \tag{7.32}$$

Therefore the real part of the correlation matrices is symmetric around the main- and antidiagonal.

7.5. Susceptibilities

For periodic systems, the density and magnetic DΓA susceptibilities $\chi_d(\mathrm{i}\omega, \mathbf{q})$ and $\chi_m(\mathrm{i}\omega, \mathbf{q})$ are the Fourier transform of the following imaginary time expectation values:

$$\chi_d(\tau, l - l') = \langle \mathrm{T}(n_{l\uparrow} + n_{l\downarrow})(\tau)(n_{l'\uparrow} + n_{l'\downarrow})(0)\rangle, \tag{7.33}$$

$$\chi_m(\tau, l - l') = \langle \mathrm{T}(n_{l\uparrow} - n_{l\downarrow})(\tau)(n_{l'\uparrow} - n_{l'\downarrow})(0)\rangle. \tag{7.34}$$

Here l and l' are lattice site indices, T is the time-ordering operator and $n_{l\sigma}$ is the electron density at site l with spin $\sigma \in \{\uparrow, \downarrow\}$. In DMFT, they are calculated in momentum space for the square-lattice HM at half-filling, using the Bethe–Salpeter equations discussed in section 7.2.1. All results in this section are generated using the same parameters as in section 7.3: $U = 4t$, $\beta = \{2/t, 4/t\}$, where $t = 1$ sets the energy unit, and only nearest-neighbor hopping is considered. Again, we use nine bosonic as well as 40 and 80 fermionic frequencies for $\beta = 2$ and $\beta = 4$, respectively. The inner momentum- or $\mathbf{k}$-grid (for the one-particle quantities and χ_0) is 48×48, whereas the transfer momentum- or $\mathbf{q}$-grid is 12×12 for $\beta = 2$ and 24×24 for $\beta = 4$. As before, the total number of QMC measurements n_t for the two-particle Green's function is given in multiples of $n_0 = 2.4 \times 10^6$ and divided into n_b bins, with $n_m = n_t/n_b$ measurements averaged per bin. These averages are then used as the input samples for the jackknife. Note that at half-filling, the susceptibilities and therefore also their correlation matrices are purely real.

7.5.1. Standard error of the mean

Figure 7.8 shows the density and magnetic susceptibilities at $\beta = 2$ and $\beta = 4$, where $n_t = 256 \times n_0$ measurements are divided into $n_b = 256$ bins. Since there is a transition

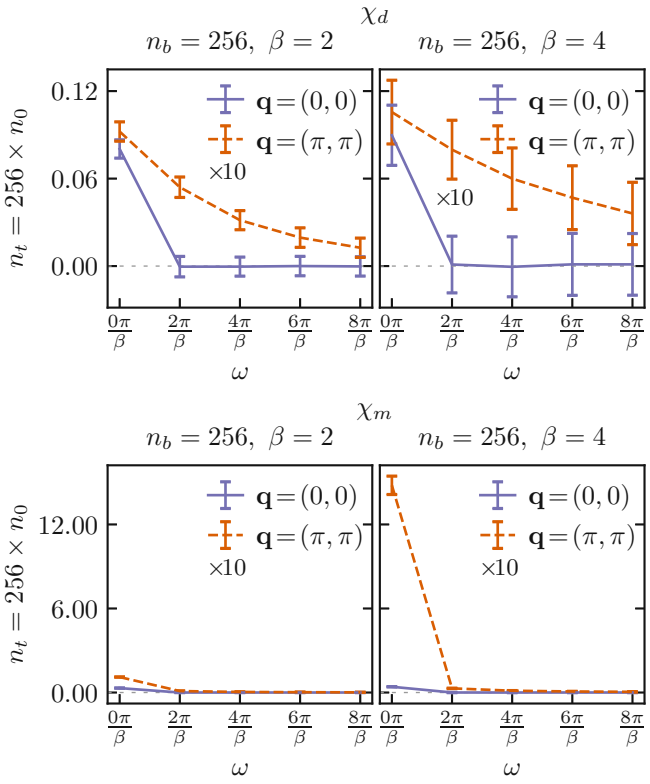

Figure 7.8.: Density and magnetic DMFT susceptibility, χ_d and χ_m, at different temperatures and momenta. For better visibility the error bars are enlarged by a factor of 10.

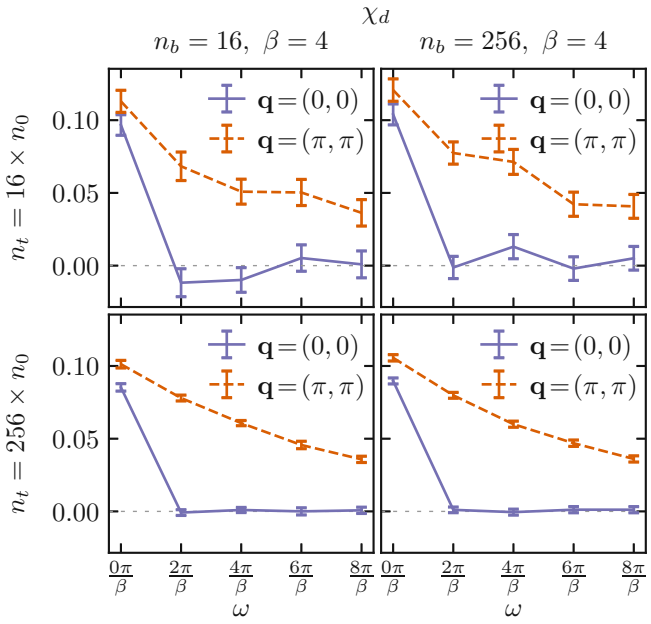

Figure 7.9.: DMFT density susceptibility χ_d at $\beta = 4$ for two different momenta $\mathbf{q}$, comparing different numbers of bins and total measurements.

to an antiferromagnetic phase at $\beta = 4.3$[109], $\chi_m(\mathbf{q} = (\pi, \pi))$ as well as its error are dominated by the contributions at $\omega = 0$. This makes it harder to compare the plots of the two susceptibilities, but one can still see that the SEM increases with β (left vs right panels) for both quantities, just like in the case of the DΓA self-energy.

The dependence on the total number of measurements n_t and the number of bins n_b is shown in fig. 7.9 for χ_d and in fig. 7.10 for χ_m; both at $\beta = 4$. They use the same layout as fig. 7.5, i.e., $n_t = 16 \times n_0$ in the top rows and $256 \times n_0$ in the bottom ones, with $n_b = 16$ on the left and 256 on the right. Only the error bars of χ_m are enlarged by a factor of 10. Similar to section 7.4 the SEM scales with the total number of measurements (top vs. bottom panels), but it does not depend on the number of jackknife samples n_b (left vs. right panels). Contrary to the results of the self-energy, even using a total of $256 \times n_0 \approx 6 \times 10^8$ measurements only yields borderline acceptable error bars. This means the main features of the χ_d curve are still recognizable, but larger error bars would render the signal statistically insignificant. Therefore, one should aim for at least $O(10^9)$ total measurements in this case.

7.5.2. Correlation matrix

The estimate for the correlation of the susceptibilities with themselves is shown in fig. 7.11. Both χ_d and χ_m are uncorrelated for both temperatures ($\beta = 2$ and $\beta = 4$)

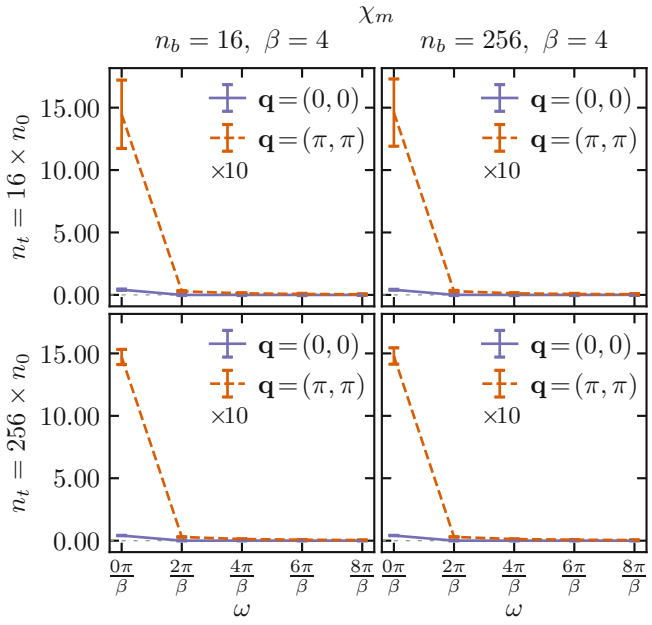

Figure 7.10.: Same as fig. 7.9 but for the magnetic susceptibility χ_m. For better visibility the error bars are enlarged by a factor of 10.

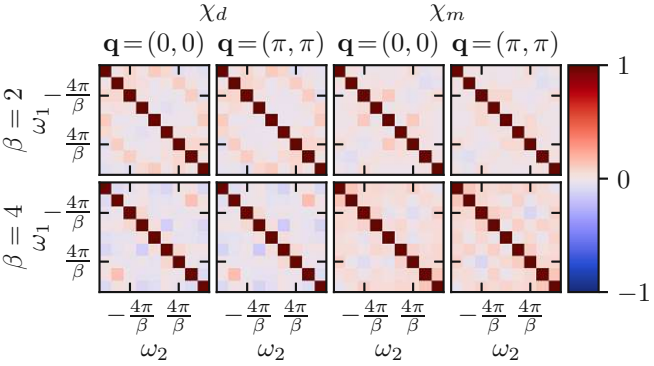

Figure 7.11.: Estimated correlation matrix of the DMFT susceptibilities $\widehat{\mathrm{corr}}[\chi_r(\omega_1), \chi_r(\omega_2)]$, $r \in \{m, d\}$ at different temperatures and momenta. A total number of $256 \times n_0$ measurements are binned into 256 jackknife samples. The 9×9 matrices correspond to nine bosonic frequencies.

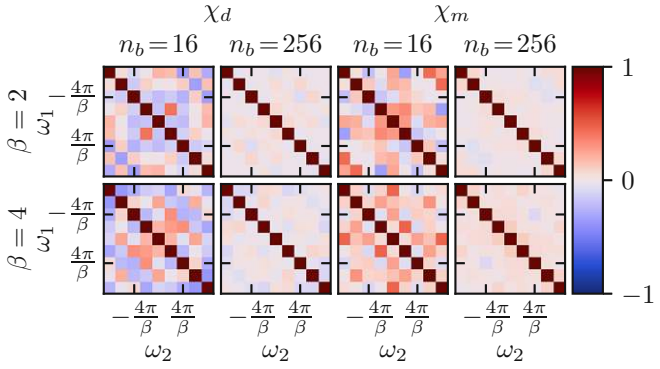

Figure 7.12.: Same as fig. 7.11 but now at $\mathbf{q} = (\pi, 0)$ and comparing different numbers of jackknife bins n_b for a total number of $16 \times n_0$ measurements.

and for both momenta [$\mathbf{q} = (0,0)$ and $\mathbf{q} = (\pi,\pi)$]. The same is true for $\mathbf{q} = (\pi, 0)$, shown in fig. 7.12, which studies the effects of using more jackknife bins. Clearly, a good estimate of the correlation matrix of the susceptibility requires more than $O(10)$ bins.

The symmetries of the correlation matrices in figs. 7.11 and 7.12 are the same as those in section 7.4.2. They are symmetric around the main- and antidiagonal because $\chi_{m,d}(\omega) = \chi_{m,d}(-\omega)$, which is the same property as that of the self-energy considering that the susceptibilities are also real.

7.6. Maximum entropy analytic continuation

Extracting real-frequency information, $A(\omega)$, out of Matsubara-frequency data, $y(\nu)$, amounts to solving the following fitting problem:

$$\min_A \left\| y(\nu) - \int \mathrm{d}\omega K(\nu,\omega) A(\omega) \right\| = \min_{\mathbf{A}} ||\mathbf{y} - K\mathbf{A}||, \tag{7.35}$$

where K is an integral kernel which is different for bosonic or fermionic functions. $\mathbf{y}$ and $\mathbf{A}$ are the Fourier coefficients of $y(\nu)$ and $A(\omega)$ in an appropriate basis. Equation (7.35) is minimal if and only if the log-likelihood:

$$L[\mathbf{A}] = -\tfrac{1}{2}(\mathbf{y} - K\mathbf{A})^\dagger C^{-1} (\mathbf{y} - K\mathbf{A}), \tag{7.36}$$

is maximal, where C is the covariance matrix (a positive definite symmetric matrix). Equations (7.35) and (7.36) are ill-posed on numerical data as the singular values of K drop super-exponentially.

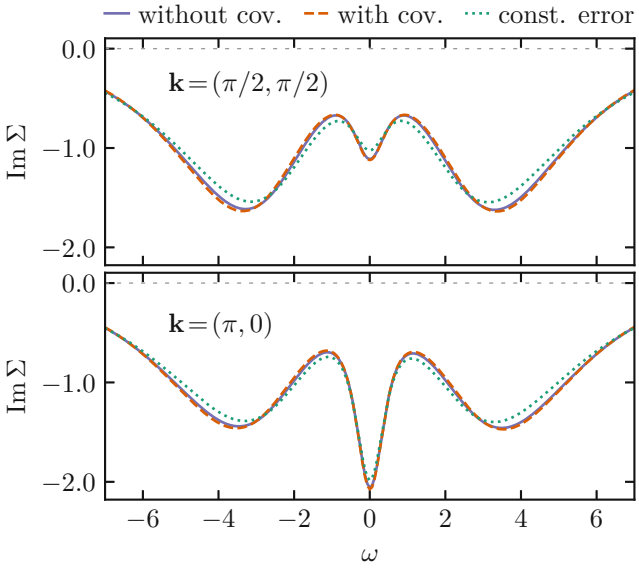

Figure 7.13.: Imaginary part of the self-energy on the real-frequency axis at different momenta $\mathbf{k}$, comparing the analytic continuation without covariance matrix, with the proper covariance matrix, and with a constant error.

The maximum entropy method [110] is a widely employed method to regularize this problem. Briefly, instead of eq. (7.35), we maximize an augmented functional:

$$Q_\alpha[\mathbf{A}] = L[\mathbf{A}] + \alpha S[\mathbf{A}|\mathbf{A}_0], \tag{7.37}$$

where $S[\mathbf{A}|\mathbf{A}_0]$ is the relative (information) entropy with respect to an *a priori* default model $\mathbf{A}_0$. This term regularizes the optimization and has to be scaled by a hyperparameter α. Equation (7.37) can be used on numerical data: $\mathbf{y}$ is now the sample mean and C is the sample covariance matrix in eq. (7.36).

Equation (7.36) can be evaluated much more efficiently, if the covariance matrix is diagonal. However, if that is not the case, we may still perform the transformation $C = \mathcal{U}^\dagger V \mathcal{U}$, where $\mathcal{U}$ is unitary and V is a positive definite diagonal matrix. Equation (7.36) then acquires the simpler form

$$L[\mathbf{A}] = -\frac{1}{2} \sum_j \frac{\left|\tilde{\mathbf{y}}_j - (\tilde{K}\mathbf{A})_j\right|^2}{V_j} \tag{7.38}$$

with $\tilde{\mathbf{y}} = \mathcal{U}\mathbf{y}$ and $\tilde{K} = \mathcal{U}K$.

If this rotation of the data and the kernel is done as a pre-processing step, then the remaining problem is identical to the case where the covariance matrix is diagonal. In

particular, it is still possible to treat real and imaginary part as separate variables by stacking $\tilde{\mathbf{y}} \to [\operatorname{Re}\tilde{\mathbf{y}}, \operatorname{Im}\tilde{\mathbf{y}}]$ and $\tilde{K} \to [\operatorname{Re}\tilde{K}, \operatorname{Im}\tilde{K}]$. We use the `ana_cont` library[111, 112] to perform analytic continuations of the DΓA self-energy at $\beta = 4$. To this end, we have to subtract the Hartree energy $U/2$, such that asymptotically also the real part approaches zero. Then the standard kernel for fermionic Green's functions can be used[113], and we obtain a function $A_\Sigma(\omega)$ which is related to the imaginary part of the self-energy by

$$A_\Sigma(\omega) = -\frac{1}{\pi} \operatorname{Im}\Sigma(\omega + \mathrm{i}0^+). \tag{7.39}$$

In fig. 7.13 we see that in this case the correlations are not strong enough to make the analytic continuation instable. However, using a constant error rather the one calculated by the jackknife method leads to a slightly different result.

7.7. Conclusion and discussion

We have implemented and studied a jackknife error estimate for typical DMFT and DΓA post-processing calculations after a QMC solution of the Anderson impurity problem. While mere QMC error bars have been analyzed before (also employing the jackknife[38, 114]), the error of the post-processed quantities such as the DMFT susceptibilities and the DΓA self-energies has not been systematically studied. Here, the QMC statistical error is propagated through nonlinear equations, namely the Bethe–Salpeter equation. In such a situation the jackknife method is the method of choice, and we make our routines that have been tested with QMC input from w2dynamics[82] available at ref. [115].

From a statistical point of view, our study reveals that the different components of the two-particle Green's function, which is the CT-HYB QMC output and main jackknife input, are uncorrelated. But a binning into $O(100)$ bins is necessary to remove the spurious off-diagonal components of the correlation matrix. The same holds for the DMFT susceptibility which is calculated through the Bethe–Salpeter equation. Because of the vanishing off-diagonal elements of the correlation (or covariance) matrix, an analytical continuation without covariance is possible.

The DΓA self-energy on the other hand has a nondiagonal correlation matrix. Its calculation consists of the Bethe–Salpeter equation, as in DMFT, and additionally the Schwinger–Dyson equation. We conclude that the latter leads to the correlations between the DΓA self-energy at different frequencies. This is also quite intuitive since the same (bosonic) frequency component of the susceptibility contributes to the DΓA self-energy at different fermionic frequencies. However, we have shown that the results of analytic continuation of the self-energy are hardly influenced by this. We thus conclude that the correlations introduced by two-particle corrections are still small enough to allow for a reliable interpretation of the results. Still one should keep in

mind that using the actual jackknife error, as opposed to a constant, does have a small influence on the analytic continuation.

We have further studied the SEM and observe that it hardly depends on the number of bins n_b into which the total number of measurements n_t is divided. However, as a matter of course the SEM depends strongly on n_t. Depending on the physical quantity studied and the required accuracy, a total number of measurements n_t of $O(10^7)$ to $O(10^9)$ is needed. Here, the error bars of the DMFT susceptibilities are somewhat larger than for the DΓA self-energy. The error also increases with decreasing temperature or larger interval $[0, \beta]$, as this interval is sampled less accurately if n_t is kept fixed.

Our paper has shown that the jackknife method is a valuable tool for calculating DMFT and DΓA error bars. Beyond the present paper, the statistical error of the one-particle Green's function can be included. However, with the use of symmetric improved estimators the errors of the one-particle Green's function are practically nonexistent. A further extension would be to consider the error of the DMFT self-consistency loop itself by drawing bins from statistically independent DMFT solutions. The latter can be achieved either by completely independent DMFT calculations or by determining the auto-correlation time of the DMFT loop and adjusting the binning to it. Our approach can be combined with various other methods to reduce the Monte Carlo noise[77, 79, 116] or the cutoff error of the frequency box[105, 117–120] as well as with compactifications of the vertex[121–123]. We hope that our paper will spread the seed for a proper error estimate in future DMFT calculations and diagrammatic extensions thereof.

8. Summary and outlook

In this thesis we ventured into the still hardly explored lands of three-particle correlations. After a short recapitulation of definitions and well-known facts from the one- and two-particle level we started with generalizing those theoretical basics to three particles. As expected this was in general accompanied by an increase in complexity. Even though the number of independent spin components of the three-particle Green's function can be reduced to just three, the number of possible frequency notations increased significantly, just to mention one complexity factor. Unlike the three notations for two-particle quantities, we showed that there are 15 two-particle and ten three-particle notations for three-particle quantities. The decomposition of the three-particle Green's function is also more complicated than that of the two-particle one with 16 instead of three terms, respectively. Furthermore, we introduced the vertex expansion as a general concept and then applied it to the three-particle Green's function. This yielded our first approximation for it using only one- and two-particle quantities.

In chapter 5 we presented an application for three-particle correlations: nonlinear, more precisely second-order, response theory. After deriving the necessary formulas we scanned the parameter regime for an Anderson impurity model (AIM) and found sizable second-order density, density-magnetic, and chiral response functions at different dopings. We also presented some results for a square lattice Hubbard model (HM). Most importantly though, we showed that in cases of significant second-order response functions the contribution from the full three-particle vertex is not negligible and sometimes even dominant.

After these reassuring results we went back to more theoretical base work in chapter 6. First we derived Bethe–Salpeter-like equations for three particles. Of course, they turned out to be much more involved than those on the two-particle level. Next we came to the main focus of that chapter: approximating the three-particle ladder with a geometric series using only irreducible two-particle vertices and Green's function lines. While this idea initially seemed rather simple, we found that the approximation needed to be more intricate than expected for it to reproduce all symmetries of the full three-particle vertex. Even then, the numerical results computed for an AIM were only qualitatively good for small values of the on-site Coulomb interaction.

In the last chapter we presented what was chronologically the author's first PhD project: statistical error estimation with jackknife. Apart from the code for resampling dynamical mean-field theory (DMFT) susceptibilities and dynamical vertex approximation (DΓA) self-energies, we also implemented error estimation directly in w2dynamics for quantities

like the DMFT self-energy. This allows us to reliably determine if the DMFT self-consistency loop is converged and if the desired precision is reached. Since most of our numerical results are based on DMFT solutions this proved to be a very useful feature for the present thesis even though it is not directly related to three-particle correlations.

After this brief summary, let us look ahead at what is still unanswered and might be of interest for future research. In section 2.7 we already mentioned that the Schwinger–Dyson equations form an infinite stack but only presented the lowest order one connecting one- and two-particle quantities. A derivation of the next order would give us more insight into how the three-particle vertex influences two-particle quantities. Since quantum Monte Carlo (QMC) measurements allow us to directly compute local two-particle Green's functions, one could use this as an additional test for approximations of the three-particle vertex: Compute a two-particle quantity with the corresponding Schwinger–Dyson equation using an approximated three-particle vertex and compare it to the exact QMC solution. It might even be interesting to check what happens when the three-particle vertex is completely neglected.

On the topic of approximations, since the approximate three-particle ladder fell short of expectations, one could compute numerical results for the two-particle vertex expansion of the three-particle Green's function and see if it performs better. Finishing the computation of the third-order terms and maybe expanding it to fourth order might even help with the approximate ladder. After all we believe that overcounting between ladders in different channels is only a problem up to some, hopefully low, number of two-particle vertices. Of course, it would also be very interesting to compute a ladder with the irreducible three-particle vertex. The corresponding equations are exact, but we do not have a feasible way of computing that vertex yet. An approximation will most likely be necessary, but it might be easier to find a good approximation for the local irreducible vertex than for the full one.

Finally, let us come back to the topic of nonlinear response functions. Even though we found sizable contributions to them, we only scanned a small parameter regime of a rather simple model. The question is, whether there are real materials and effects which show similar results. We mentioned Raman response as a real world example for second-order effects, but Raman scattering involves photons and typically also phonons. So, to compute real amplitudes one would need to consider the matrix elements for electron–photon coupling, or even include electron–phonon interactions as well. In a one-band model this requires nonlocal, i.e., momentum-dependent three-particle vertices. The approximate ladder could, in theory, use nonlocal Green's functions to get an approximation for such nonlocal three-particle correlations. However, it seems that better approximations or other methods for computing the three-particle vertex are necessary before such real-world applications are feasible.

A. Supplemental material: three-particle correlators and nonlinear response

Parts of this appendix marked with a vertical bar have already been published in Kappl et al. [55].

A.1. From spin correlators to second-order response functions

In this section we present all the details and explicit equations, purposefully omitted for brevity in section 5.2, to get from two- and three-particle correlators to the second-order density, density-magnetic, and chiral response functions. This is interesting if one actually wants to implement the computations since, in our case, w2dynamics can only directly measure the spin correlators.

We start by giving explicit formulas for eq. (5.13)

$$\chi_{nnn} = 2\Big(\chi_{\uparrow\uparrow\uparrow} + \chi_{\uparrow\uparrow\downarrow} + \chi_{\uparrow\downarrow\uparrow} + \chi_{\downarrow\uparrow\uparrow}\Big), \tag{A.1}$$

$$\begin{aligned}\chi_{nzz} &= 2\Big(\chi_{\uparrow\uparrow\uparrow} - \chi_{\uparrow\uparrow\downarrow} - \chi_{\uparrow\downarrow\uparrow} + \chi_{\downarrow\uparrow\uparrow}\Big) \\ &= 2\Big(\chi_{\uparrow\uparrow\overline{\downarrow}} + \chi_{\downarrow\uparrow\overline{\downarrow}}\Big),\end{aligned} \tag{A.2}$$

$$\chi_{xyz} = 2\mathrm{i}\Big(\chi_{\overline{\uparrow}\downarrow\uparrow} - \chi_{\overline{\uparrow}\downarrow\downarrow}\Big), \tag{A.3}$$

where we use SU(2) symmetry, introduce the second-order spin susceptibilities

$$\chi_{\sigma_1\dots\sigma_6} = \operatorname{conn} X_{\sigma_1\dots\sigma_6}, \tag{A.4}$$

and use the compact spin notation from eq. (4.9). Since subtracting the disconnected parts of the full correlators is a linear operation eqs. (A.1) to (A.3) also hold when replacing χ with X.

Section 4.3 shows that the 20 nonvanishing spin components of the three-particle quantities can be reduced to just three independent ones, namely $\uparrow\uparrow\uparrow$, $\uparrow\uparrow\downarrow$ and $\uparrow\overline{\uparrow\downarrow}$. All other components can be calculated from these by applying SU(2), swapping or time-reversal symmetry. This makes numerical computations much cheaper. Exploiting

this, we rewrite eqs. (A.1) to (A.3) in Matsubara space as

$$\chi^{\omega_1\omega_2}_{nnn} = 2\Big(\chi^{\omega_1\omega_2}_{\uparrow\uparrow\uparrow} + \chi^{\omega_1\omega_2}_{\uparrow\uparrow\downarrow} + \chi^{\omega_1\omega_3}_{\uparrow\uparrow\downarrow} + \chi^{\omega_3\omega_2}_{\uparrow\uparrow\downarrow}\Big), \tag{A.5}$$

$$\begin{aligned}\chi^{\omega_1\omega_2}_{nzz} &= 2\Big(\chi^{\omega_1\omega_2}_{\uparrow\uparrow\uparrow} - \chi^{\omega_1\omega_2}_{\uparrow\uparrow\downarrow} - \chi^{\omega_1\omega_3}_{\uparrow\uparrow\downarrow} + \chi^{\omega_3\omega_2}_{\uparrow\uparrow\downarrow}\Big) \\ &= 2\Big(\chi^{\omega_1\omega_2}_{\uparrow\overline{\uparrow}\downarrow} + \chi^{\omega_1\omega_3}_{\uparrow\overline{\uparrow}\downarrow}\Big),\end{aligned} \tag{A.6}$$

$$\chi^{\omega_1\omega_2}_{xyz} = 2\mathrm{i}\Big(\chi^{\omega_3\omega_1}_{\uparrow\overline{\uparrow}\downarrow} - \chi^{\omega_3\omega_2}_{\uparrow\overline{\uparrow}\downarrow}\Big), \tag{A.7}$$

where $\omega_3 = -\omega_1 - \omega_2$.

For the second-order spin susceptibilities the explicit form of eq. (5.6) reads

$$\begin{aligned}\chi^{\omega_1\omega_2}_{\sigma_1\sigma_2\sigma_3} = {} & X^{\omega_1\omega_2}_{\sigma_1\sigma_2\sigma_3} - \delta^{\omega_1 0}\delta^{\omega_2 0}\beta^2\langle\hat{n}_{\sigma_1}\rangle\langle\hat{n}_{\sigma_2}\rangle\langle\hat{n}_{\sigma_3}\rangle \\ & - \delta^{\omega_2 0}\beta\langle\hat{n}_{\sigma_2}\rangle\chi^{\omega_3}_{\sigma_3\sigma_1} \\ & - \delta^{\omega_3 0}\beta\langle\hat{n}_{\sigma_3}\rangle\chi^{\omega_1}_{\sigma_1\sigma_2} \\ & - \delta^{\omega_1 0}\beta\langle\hat{n}_{\sigma_1}\rangle\chi^{\omega_2}_{\sigma_2\sigma_3},\end{aligned} \tag{A.8}$$

$$\chi^{\omega_1\omega_2}_{\sigma_1\overline{\sigma_2}\sigma_3} = X^{\omega_1\omega_2}_{\sigma_1\overline{\sigma_2}\sigma_3} - \delta^{\omega_1 0}\beta\langle\hat{n}_{\sigma_1}\rangle\chi^{\omega_2}_{\overline{\sigma_3}\sigma_2}, \tag{A.9}$$

$$\chi^{\omega_1\omega_2}_{\overline{\sigma_1}\sigma_2\overline{\sigma_3}} = X^{\omega_1\omega_2}_{\overline{\sigma_1}\sigma_2\overline{\sigma_3}} - \delta^{\omega_2 0}\beta\langle\hat{n}_{\sigma_2}\rangle\chi^{\omega_3}_{\overline{\sigma_1}\sigma_3}, \tag{A.10}$$

$$\chi^{\omega_1\omega_2}_{\overline{\sigma_1}\sigma_2\sigma_3} = X^{\omega_1\omega_2}_{\overline{\sigma_1}\sigma_2\sigma_3} - \delta^{\omega_3 0}\beta\langle\hat{n}_{\sigma_3}\rangle\chi^{\omega_1}_{\overline{\sigma_2}\sigma_1}. \tag{A.11}$$

Similarly, using eq. (5.5) yields

$$\chi^{\omega}_{\sigma_1\sigma_2} = \langle \mathrm{T}\,\hat{n}_{\sigma_1}\hat{n}_{\sigma_2}\rangle^{\omega} - \delta^{\omega 0}\beta\langle\hat{n}_{\sigma_1}\rangle\langle\hat{n}_{\sigma_2}\rangle \tag{A.12}$$

$$\chi^{\omega}_{\overline{\sigma_1\sigma_2}} = \langle \mathrm{T}\,\hat{c}^\dagger_{\sigma_1}\hat{c}_{\sigma_2}\hat{c}^\dagger_{\sigma_2}\hat{c}_{\sigma_1}\rangle^{\omega} \tag{A.13}$$

for the linear spin susceptibilities. Together these equations complete the set of explicit formulas necessary to compute the second-order density, density-magnetic, and chiral response functions from two- and three-particle spin correlators.

Combining eq. (A.3) and eq. (A.11) shows that the disconnected terms for χ_{xyz} cancel, which means that it is directly given by X_{xyz}. This is similar to the two-particle case where the magnetic response function χ_{zz} equals the full correlator $X_{zz} = \langle \mathrm{T}\,\hat{\sigma}_z\hat{\sigma}_z\rangle$ [see eq. (5.19)] because there are no disconnected terms either.

In the special case of half-filling, i.e., $\langle \hat{n}_\sigma \rangle = 1/2 = 1 - \langle \hat{n}_\sigma \rangle$ we can further compute

$$\begin{aligned} X_{\sigma_1\sigma_2\sigma_3} &= \langle \mathrm{T}(1-\hat{n}_{\sigma_1})(1-\hat{n}_{\sigma_2})(1-\hat{n}_{\sigma_3})\rangle && \text{(A.14)} \\ &= \langle 1-\hat{n}_{\sigma_1}-\hat{n}_{\sigma_2}-\hat{n}_{\sigma_3}\rangle \\ &\quad + \langle \mathrm{T}(\hat{n}_{\sigma_1}\hat{n}_{\sigma_2}+\hat{n}_{\sigma_1}\hat{n}_{\sigma_3}+\hat{n}_{\sigma_2}\hat{n}_{\sigma_3})\rangle && \text{(A.15)} \\ &\quad - \langle \mathrm{T}\,\hat{n}_{\sigma_1}\hat{n}_{\sigma_2}\hat{n}_{\sigma_3}\rangle, \\ 2X_{\sigma_1\sigma_2\sigma_3} &= \sum_{i<j}\langle \mathrm{T}\,\hat{n}_{\sigma_i}\hat{n}_{\sigma_j}\rangle - \frac{1}{2}\,. && \text{(A.16)} \end{aligned}$$

This shows that the full, density-like, three-particle spin correlators only consist of disconnected terms for half-filling, or equivalently $\chi_{\sigma_1\sigma_2\sigma_3}$ vanishes. Looking at eqs. (A.1) and (A.2) this also implies that the second-order density and density-magnetic response functions vanish at half-filling.

A.2. Lehmann formula for the three-particle correlator

In the atomic limit, $\hat{H}_{\mathrm{AL}} = \epsilon(\hat{n}_\uparrow + \hat{n}_\downarrow) - h(\hat{n}_\uparrow - \hat{n}_\downarrow) + U\hat{n}_\uparrow\hat{n}_\downarrow$, where $\epsilon = -U/2$, we use the following Lehmann formula for the three-particle correlation function:

$$\begin{aligned} X(\tau_1,\tau_2) &= \langle \mathrm{T}\,\hat{\rho}_1(\tau_1)\hat{\rho}_2(\tau_2)\hat{\rho}_3(0)\rangle \\ &= \theta(\tau_1-\tau_2)\sum_{i,j,k} w_i \mathrm{e}^{\tau_1 E_{ij}+\tau_2 E_{jk}}\rho_1^{ij}\rho_2^{jk}\rho_3^{ki} \\ &\quad + \theta(\tau_2-\tau_1)\sum_{i,j,k} w_i \mathrm{e}^{\tau_2 E_{ij}+\tau_1 E_{jk}}\rho_2^{ij}\rho_1^{jk}\rho_3^{ki}. \end{aligned} \qquad \text{(A.17)}$$

Here, $\hat{\rho}_{1,2,3}$ are bosonic operators, θ is the Heaviside step function, $E_{ij} = E_i - E_j$, $w_i = \mathrm{e}^{-\beta E_i}/\mathcal{Z}$, $\mathcal{Z} = \sum_i \mathrm{e}^{-\beta E_i}$, and $\rho^{ij} = \langle i|\hat{\rho}|j\rangle$. The eigenstates of $\hat{H}_{\mathrm{AL}}$ are $|0\rangle$, $|\downarrow\rangle$, $|\uparrow\rangle$, and $|\updownarrow\rangle$ with eigenenergies $E_0 = 0$, $E_\downarrow = \epsilon + h$, $E_\uparrow = \epsilon - h$, and $E_\updownarrow = U + 2\epsilon$.

We transform $X(\tau_1,\tau_2)$ via eq. (5.26) to frequencies, taking care of degeneracies:

$$X^{\omega_1\omega_2} = \mathcal{X}(\omega_1,\omega_2,\hat{\rho}_1,\hat{\rho}_2) + \mathcal{X}(\omega_2,\omega_1,\hat{\rho}_2,\hat{\rho}_1), \qquad \text{(A.18)}$$

$$
\begin{aligned}
\mathcal{X}(\omega_x,\omega_y,\hat{\rho}_x,\hat{\rho}_y) = \sum_{i,j,k} w_i \rho_x^{ij}\rho_y^{jk}\rho_3^{ki}\Bigg\{ & \frac{1-\delta(\mathrm{i}\omega_y+E_{jk})}{\mathrm{i}\omega_y+E_{jk}}\Bigg[\\
& -\frac{\mathrm{e}^{\beta E_{ij}}-1}{\mathrm{i}\omega_x+E_{ij}}\big(1-\delta(\mathrm{i}\omega_x+E_{ij})\big)-\beta\delta(\mathrm{i}\omega_x+E_{ij}) \\
& +\frac{\mathrm{e}^{\beta E_{ik}}-1}{\mathrm{i}\omega_x+\mathrm{i}\omega_y+E_{ik}}\big(1-\delta(\mathrm{i}\omega_x+\mathrm{i}\omega_y+E_{ik})\big) \\
& +\beta\delta(\mathrm{i}\omega_x+\mathrm{i}\omega_y+E_{ik})\Bigg] \\
& +\left[\frac{\beta\mathrm{e}^{\beta E_{ij}}}{\mathrm{i}\omega_x+E_{ij}}-\frac{\mathrm{e}^{\beta E_{ij}}-1}{(\mathrm{i}\omega_x+E_{ij})^2}\right]\delta(\mathrm{i}\omega_y+E_{jk})(1-\delta(\mathrm{i}\omega_x+E_{ij})) \\
& +\frac{\beta^2}{2}\delta(\mathrm{i}\omega_y+E_{jk})\delta(i\omega_x+E_{ij})\Bigg\}.
\end{aligned}
\tag{A.19}
$$

Note that eqs. (A.17) to (A.19) are not restricted to the atomic limit.

A.3. Asymptotic behavior of $\chi^{(2)}$

Using the Lehmann representation one can show that bosonic, two-particle correlation functions can be expanded in the following series:

$$
\langle \hat{A}_i \hat{A}_j\rangle^z = -\frac{1}{z}\langle[\hat{A}_i,\hat{A}_j]\rangle+\frac{1}{z^2}\langle[[\hat{A}_i,\hat{H}],\hat{A}_j]\rangle+\dots, \tag{A.20}
$$

where z is a complex frequency, $\hat{H}$ is the Hamiltonian and $[\cdot,\cdot]$ denotes the commutator (see also [81, Appendix C]). Since

$$
\chi^{0\omega}_{nnn} = -\frac{\partial}{\partial\epsilon}\chi^{\omega}_{nn} = \left(\frac{\partial}{\partial\epsilon}X^{\omega}_{nn}-\delta^{\omega 0}\beta\langle\hat{n}\rangle^2\right) = \frac{\partial}{\partial\epsilon}X^{\omega}_{nn}, \tag{A.21}
$$

$$
\chi^{0\omega}_{nzz} = \frac{\partial}{\partial\epsilon}\chi^{\omega}_{zz} = \frac{\partial}{\partial\epsilon}X^{\omega}_{zz}, \tag{A.22}
$$

$$
\chi^{0\omega}_{xyz} = \frac{\partial}{\partial h_x}\chi^{\omega}_{yz} = \frac{\partial}{\partial h_x}X^{\omega}_{yz}, \tag{A.23}
$$

with Matsubara frequencies ω, evaluating the expansion at $z=\mathrm{i}\omega$ can be used to obtain the asymptotic behavior of slices of the second-order response functions:

$$
\chi^{0\omega}_{nnn} \approx -\frac{1}{(\mathrm{i}\omega)^2}\frac{\partial}{\partial\epsilon}\langle[[\hat{n},\hat{H}],\hat{n}]\rangle, \tag{A.24}
$$

$$
\chi^{0\omega}_{nzz} \approx -\frac{1}{(\mathrm{i}\omega)^2}\frac{\partial}{\partial\epsilon}\langle[[\hat{\sigma}_z,\hat{H}],\hat{\sigma}_z]\rangle, \tag{A.25}
$$

$$\chi^{0\omega}_{xyz} \approx -\frac{1}{\mathrm{i}\omega}\frac{\partial}{\partial h_x}\langle[\hat{\sigma}_y, \hat{\sigma}_z]\rangle. \tag{A.26}$$

The density and density-magnetic channels do not have a $1/(\mathrm{i}\omega)$ term since $[\hat{n}, \hat{n}]$ and $[\hat{\sigma}_z, \hat{\sigma}_z]$ vanish. According to [81], for an Anderson impurity model (AIM) the commutators in eqs. (A.24) and (A.25) are given by

$$\langle[[\hat{n}, \hat{H}_{\mathrm{AIM}}], \hat{n}]\rangle = \langle[[\hat{\sigma}_z, \hat{H}_{\mathrm{AIM}}], \hat{\sigma}_z]\rangle = -\langle\hat{H}_V\rangle = -\frac{2}{\beta}\sum_{\sigma\nu}\Delta^\nu_\sigma G^\nu_\sigma \tag{A.27}$$

where $\hat{H}_V$ is the hybridization term in the Hamiltonian of the AIM [last term in eq. (3.1)], Δ^ν_σ is the hybridization function and G^ν_σ is the one-particle Green's function of the impurity. Differentiating the latter with respect to ϵ yields

$$\begin{aligned}
\frac{\partial}{\partial\epsilon}G^\nu_\sigma &= -\frac{\partial}{\partial\epsilon}\langle \mathrm{T}\,\hat{c}_\sigma(\tau)\hat{c}^\dagger_\sigma\rangle^\nu && \text{(A.28)}\\
&= \beta\langle\hat{n}\rangle G^\nu_\sigma + \sum_{\sigma'}\langle \mathrm{T}\,\hat{n}_{\sigma'}(\tau')\hat{c}_\sigma(\tau)\hat{c}^\dagger_\sigma\rangle^{\nu 0} && \text{(A.29)}\\
&= \beta\langle\hat{n}\rangle G^\nu_\sigma + \sum_{\sigma'}\langle \mathrm{T}(1-\hat{c}_{\sigma'}(\tau')\hat{c}^\dagger_{\sigma'}(\tau'))\hat{c}_\sigma(\tau)\hat{c}^\dagger_\sigma\rangle^{\nu 0} && \text{(A.30)}\\
&= \beta(\langle\hat{n}\rangle - 2)G^\nu_\sigma - \sum_{\sigma'} P3^{\nu 0}_{\sigma'\sigma} && \text{(A.31)}
\end{aligned}$$

where $P3$ is the partially contracted two-particle Green's function

$$\begin{aligned}
P3^{\nu'\omega} &= \int_0^\beta\int_0^\beta G(\tau,\tau,\tau')\mathrm{e}^{\mathrm{i}(\omega\tau+(\nu'-\omega)\tau')}\,\mathrm{d}\tau\mathrm{d}\tau' && \text{(A.32)}\\
&= \frac{1}{\beta}\sum_\nu G^{\nu\nu'\omega}. && \text{(A.33)}
\end{aligned}$$

With

$$\frac{\partial}{\partial h_x}\langle[\hat{\sigma}_y, \hat{\sigma}_z]\rangle = 2\mathrm{i}\frac{\partial}{\partial h_x}\langle\hat{\sigma}_x\rangle = 2\mathrm{i}\chi^0_m \tag{A.34}$$

we can finally write

$$\begin{aligned}
\chi^{0\omega}_{nnn} &\approx -\frac{1}{\omega^2}\frac{\partial}{\partial\epsilon}\langle H_V\rangle && \text{(A.35)}\\
\chi^{0\omega}_{nzz} &\approx -\frac{1}{\omega^2}\frac{\partial}{\partial\epsilon}\langle H_V\rangle && \text{(A.36)}\\
\chi^{0\omega}_{xyz} &\approx -\frac{2}{\omega}\chi^0_m, && \text{(A.37)}
\end{aligned}$$

where

$$-\frac{\partial}{\partial\epsilon}\langle H_V\rangle = \frac{4}{\beta}\sum_{\nu}\Delta^{\nu}_{\uparrow}\Big(P3^{\nu 0}_{\uparrow\uparrow} + P3^{\nu 0}_{\uparrow\downarrow} + \beta(2-\langle\hat{n}\rangle)G^{\nu}_{\uparrow}\Big), \tag{A.38}$$

and we use SU(2) symmetry.

Acknowledgements

Let me start with my parents. I don't know how they did it, but not only did they nurture my curiosity about how the world and everything in it works, no, they also managed to make me enjoy school, learning and studying in general. Without the initial conditions they provided and the continued support they showed me my whole life, I would definitely not be who or where I am today, so my biggest thanks to *Franz* and *Isabella*.

Next I want to express my gratitude towards my supervisor *Karsten Held*. Apart from the obvious thing of giving me the chance to do this PhD in the first place, I want to thank him for the many meetings and discussions he found time for in his undoubtedly busy schedule as head of the institute. As someone with no background in solid states physics before my PhD I benefited greatly from them and his impressive understanding and knowledge of the field.

At this point I also want to thank *Anna Kauch*, *Markus Wallerberger*, *Matthias Pickem*, *Christian Eckhardt*, and *Friedrich Krien* for valuable discussions regarding my different projects. A special thanks goes to *Tin Ribic* who even found time next to his job in the industry to join meetings and help me debug my code.

Even though our group contains many more people who all made my time here more enjoyable I want to specifically mention my colleagues in the office with whom I spent most of my daily working hours. My thanks go to *Josef Kaufmann*, for patiently introducing me to w2dynamics and providing invaluable parameter files, to *Matthias Winder* who never failed to bring a fun and vivid atmosphere to the office, and to *Michael Wais* with whom I still like to spend the night in a fancy bar or one of Vienna's basements. Furthermore, I am grateful to *Clemens Watzenböck* for many fun and interesting discussions over lunch, a "beer", or while bouldering, and to *Matthias Reitner* who as my desk neighbor never got tired of my stupid questions and random thoughts that I dropped seemingly out of nowhere. I also want to thank *Paul Worm* for making sure that we often enough had lunch at Shu, co-organizing movie nights, and, again, for having great conversations with a matching level of humor.

Of course the time during a PhD is not just about studying and research. In the end, I therefore want to thank all my friends who accompanied me during this journey. Some of you were always down for games, drinks, talks, dancing, bouldering, movies, etc. You are all a major reason why I enjoy my life and managed to get through my doctorate even at times when my motivation was dwindling. Thank you.

List of publications

Peer-reviewed journal publications:

- Patrick Kappl, Markus Wallerberger, Josef Kaufmann, Matthias Pickem, and Karsten Held. "Statistical error estimates in dynamical mean-field theory and extensions thereof." In: *Phys. Rev. B* 102 (8 Aug. 2020), p. 085124. DOI: 10.1103/PhysRevB.102.085124. URL: https://link.aps.org/doi/10.1103/PhysRevB.102.085124
- Patrick Kappl, Friedrich Krien, Clemens Watzenböck, and Karsten Held. "Nonlinear responses and three-particle correlators in correlated electron systems exemplified by the Anderson impurity model." In: *Phys. Rev. B* 107 (20 May 2023), p. 205108. DOI: 10.1103/PhysRevB.107.205108. URL: https://link.aps.org/doi/10.1103/PhysRevB.107.205108
- Christian J. Eckhardt, Patrick Kappl, Anna Kauch, and Karsten Held. "A functional-analysis derivation of the parquet equation." In: *SciPost Phys.* 15 (2023), p. 203. DOI: 10.21468/SciPostPhys.15.5.203. URL: https://scipost.org/10.21468/SciPostPhys.15.5.203

Bibliography

[1] P. W. Anderson. "More Is Different". In: *Science* 177.4047 (1972), pp. 393–396. DOI: 10.1126/science.177.4047.393. eprint: https://www.science.org/doi/pdf/10.1126/science.177.4047.393. URL: https://www.science.org/doi/abs/10.1126/science.177.4047.393.

[2] Tin Ribic. "Path integral methods for strong non-local correaltions". PhD thesis. Vienna University of Technology, 2018.

[3] T. Ribic, P. Gunacker, S. Iskakov, M. Wallerberger, G. Rohringer, A. N. Rubtsov, E. Gull and K. Held. "Role of three-particle vertex within dual fermion calculations". In: *Phys. Rev. B* 96 (23 Dec. 2017), p. 235127. DOI: 10.1103/PhysRevB.96.235127. URL: https://link.aps.org/doi/10.1103/PhysRevB.96.235127.

[4] T. Ribic, G. Rohringer and K. Held. "Local correlation functions of arbitrary order for the Falicov-Kimball model". In: *Phys. Rev. B* 95 (15 Apr. 2017), p. 155130. DOI: 10.1103/PhysRevB.95.155130. URL: https://link.aps.org/doi/10.1103/PhysRevB.95.155130.

[5] A. Zee. *Quantum field theory in a nutshell*. second edition. Princeton University Press, 2010. ISBN: 0691140340.

[6] T. Matsubara. "A new approach to quantum-statistical mechanics". In: *Prog. Theor. Phys.* 14 (1955), p. 351.

[7] G. C. Wick. "Properties of Bethe–Salpeter Wave Functions". In: *Phys. Rev.* 96 (4 Nov. 1954), pp. 1124–1134. DOI: 10.1103/PhysRev.96.1124. URL: https://link.aps.org/doi/10.1103/PhysRev.96.1124.

[8] Georg Rohringer. "New routes towards a theoretical treatment of nonlocal electronic correlations". PhD thesis. Vienna University of Technology, 2013.

[9] D. Sénéchal, A. M. Tremblay and C. Bourbonnais. *Theoretical Methods for Strongly Correlated Electrons (CRM Series in Mathematical Physics)*. Springer, New York, 2003.

[10] G. C. Wick. "The Evaluation of the Collision Matrix". In: *Phys. Rev.* 80 (2 Oct. 1950), pp. 268–272. DOI: 10.1103/PhysRev.80.268. URL: https://link.aps.org/doi/10.1103/PhysRev.80.268.

[11] Ian Stewart. *From here to infinity*. English. Oxford University Press New York, 1996, x, 310 p. : ISBN: 0192832026.

[12] A. A. Abrikosov, L. P. Gorkov and I. E. Dzyaloshinski. *Methods of Quantum Field Theory in Statistical Physics*. New York: Dover, 1975.

[13] N. E. Bickers and D. J. Scalapino. "Conserving Approximations for Strongly Fluctuating Electron Systems". In: *Ann. Phys. (N. Y.)* 193 (1989), p. 206.

[14] G. Rohringer, A. Valli and A. Toschi. "Local electronic correlation at the two-particle level". In: *Phys. Rev. B* 86 (12 Sept. 2012), p. 125114. DOI: 10.1103/PhysRevB.86.125114. URL: http://link.aps.org/doi/10.1103/PhysRevB.86.125114.

[15] N. E. Bickers. "Self-Consistent Many-Body Theory for Condensed Matter Systems". In: *Theoretical Methods for Strongly Correlated Electrons*. Ed. by David Sénéchal, André-Marie Tremblay and Claude Bourbonnais. New York, NY: Springer New York, 2004, pp. 237–296. ISBN: 978-0-387-21717-8. DOI: 10.1007/0-387-21717-7_6. URL: https://doi.org/10.1007/0-387-21717-7_6.

[16] E. E. Salpeter and H. A. Bethe. "A Relativistic Equation for Bound-State Problems". In: *Phys. Rev.* 84 (6 Dec. 1951), pp. 1232–1242. DOI: 10.1103/PhysRev.84.1232. URL: https://link.aps.org/doi/10.1103/PhysRev.84.1232.

[17] F. J. Dyson. "The S Matrix in Quantum Electrodynamics". In: *Phys. Rev.* 75 (11 June 1949), pp. 1736–1755. DOI: 10.1103/PhysRev.75.1736. URL: https://link.aps.org/doi/10.1103/PhysRev.75.1736.

[18] G. Rohringer, H. Hafermann, A. Toschi, A. A. Katanin, A. E. Antipov, M. I. Katsnelson, A. I. Lichtenstein, A. N. Rubtsov and K. Held. "Diagrammatic routes to nonlocal correlations beyond dynamical mean field theory". In: *Rev. Mod. Phys.* 90 (2 May 2018), p. 025003. DOI: 10.1103/RevModPhys.90.025003. URL: https://link.aps.org/doi/10.1103/RevModPhys.90.025003.

[19] Anna Galler, Patrik Thunström, Patrik Gunacker, Jan M. Tomczak and K. Held. "Ab initio dynamical vertex approximation". In: *Phys. Rev. B* 95 (11 Mar. 2017), p. 115107. DOI: 10.1103/PhysRevB.95.115107. URL: http://link.aps.org/doi/10.1103/PhysRevB.95.115107.

[20] Ryogo Kubo. "Statistical-Mechanical Theory of Irreversible Processes. I. General Theory and Simple Applications to Magnetic and Conduction Problems". In: *Journal of the Physical Society of Japan* 12.6 (June 1957), pp. 570–586. DOI: 10.1143/jpsj.12.570. URL: https://doi.org/10.1143/jpsj.12.570.

[21] A. Altland and B. D. Simons. *Condensed Matter Field Theory*. 2nd ed. Cambridge University Press, 2010. DOI: 10.1017/CBO9780511789984.

[22] P.W. Anderson. "Localized Magnetic States in Metals". In: *Phys. Rev.* 124 (1961), p. 41.

[23] Jun Kondo. "Resistance Minimum in Dilute Magnetic Alloys". In: *Progress of Theoretical Physics* 32.1 (July 1964), pp. 37–49. ISSN: 0033-068X. DOI: 10.1143/PTP.32.37. eprint: https://academic.oup.com/ptp/article-pdf/32/1/37/5193092/32-1-37.pdf. URL: https://doi.org/10.1143/PTP.32.37.

[24] J. R. Schrieffer and P. A. Wolff. "Relation between the Anderson and Kondo Hamiltonians". In: *Phys. Rev.* 149 (2 Sept. 1966), pp. 491–492. DOI: 10.1103/PhysRev.149.491. URL: https://link.aps.org/doi/10.1103/PhysRev.149.491.

[25] A.C. Hewson. *The Kondo Problem to Heavy Fermions*. Cambridge University Press, 1993.

[26] Piers Coleman. *Introduction to Many-Body Physics*. Cambridge University Press, 2015. DOI: 10.1017/CBO9781139020916.

[27] J. Hubbard. "Electron Correlations in Narrow Energy Bands". In: *Proceedings of the Royal Society of London. Series A, Mathematical and Physical Sciences* 276.1365 (1963), pp. 238–257. DOI: 10.1098/rspa.1963.0204. URL: http://rspa.royalsocietypublishing.org/content/276/1365/238.abstract.

[28] Junjiro Kanamori. "Electron correlation and ferromagnetism of transition metals". In: *Progress of Theoretical Physics* 30.3 (1963), pp. 275–289.

[29] Martin C. Gutzwiller. "Effect of Correlation on the Ferromagnetism of Transition Metals". In: *Phys. Rev. Lett.* 10 (5 Mar. 1963), pp. 159–162. DOI: 10.1103/PhysRevLett.10.159. URL: http://link.aps.org/doi/10.1103/PhysRevLett.10.159.

[30] Fabian H. L. Essler, Holger Frahm, Frank Göhmann, Andreas Klümper and Vladimir E. Korepin. *The One-Dimensional Hubbard Model*. Cambridge University Press, 2005. DOI: 10.1017/CBO9780511534843.

[31] "The Hubbard model at half a century". In: *Nature Physics* 9.9 (Sept. 2013), pp. 523–523. ISSN: 1745-2481. DOI: 10.1038/nphys2759. URL: https://doi.org/10.1038/nphys2759.

[32] Arianna Montorsi, ed. *The Hubbard Model - A Reprint Volume*. World Scientific, Singapore, 1992.

[33] Eva Pavarini, Erik Koch, Alexander Lichtenstein and Dieter Vollhardt, eds. *DMFT: From Infinite Dimensions to Real Materials*. Vol. 8. Schriften des Forschungszentrums Jülich. Reihe Modeling and Simulation. Autumn School on Correlated Electrons, Jülich (Germany), 17 Sep 2018 - 21 Sep 2018. Jülich: Forschungszentrum Jülich GmbH Zentralbibliothek, Velag, 17th Sept. 2018, getr. Zählung. ISBN: 978-3-95806-313-6. URL: https://juser.fz-juelich.de/record/852559.

[34] G. Kotliar, S. Y. Savrasov, K. Haule, V. S. Oudovenko, O. Parcollet and C. A. Marianetti. "Electronic structure calculations with dynamical mean-field theory". In: *Rev. Mod. Phys.* 78 (3 Aug. 2006), p. 865. DOI: 10.1103/RevModPhys.78.865. URL: http://link.aps.org/doi/10.1103/RevModPhys.78.865.

[35] Walter Metzner and Dieter Vollhardt. "Correlated Lattice Fermions in $d = \infty$ Dimensions". In: *Phys. Rev. Lett.* 62 (Jan. 1989), pp. 324–327. DOI: 10.1103/PhysRevLett.62.324. URL: http://link.aps.org/doi/10.1103/PhysRevLett.62.324.

[36] Antoine Georges and Gabriel Kotliar. "Hubbard model in infinite dimensions". In: *Phys. Rev. B* 45.12 (Mar. 1992), pp. 6479–6483. DOI: 10.1103/PhysRevB.45.6479.

[37] A. Georges, G. Kotliar, W. Krauth and M. J. Rozenberg. "Dynamical mean-field theory of strongly correlated fermion systems and the limit of infinite dimensions". In: *Rev. Mod. Phys.* 68.1 (Jan. 1996), p. 13. DOI: 10.1103/RevModPhys.68.13.

[38] Eva Pavarini, Erik Koch, Dieter Vollhardt and Alexander Lichtenstein. *DMFT at 25: Infinite Dimensions*. Vol. 4. Reihe Modeling and Simulation 4. Jülich: Forschungszentrum Jülich Zentralbibliothek, Verlag (Jülich), 2014. ISBN: 978-3-89336-953-9. URL: https://juser.fz-juelich.de/record/155829.

[39] K. Held. "Electronic structure calculations using dynamical mean field theory". In: *Advances in Physics* 56 (2007), pp. 829–926. DOI: 10.1080/00018730701619647.

[40] Eva Pavarini and Erik Koch, eds. *Simulating Correlations with Computers*. Vol. 11. Schriften des Forschungszentrums Jülich Modeling and Simulation. Jülich: Forschungszentrum Jülich GmbH Zentralbibliothek, Verlag, 20th Sept. 2021, p. 420. ISBN: 978-3-95806-529-1. URL: https://juser.fz-juelich.de/record/896709.

[41] A. Tamai, M. Zingl, E. Rozbicki, E. Cappelli, S. Riccò, A. de la Torre, S. McKeown Walker, F. Y. Bruno, P. D. C. King, W. Meevasana, M. Shi, M. Radovi ć, N. C. Plumb, A. S. Gibbs, A. P. Mackenzie, C. Berthod, H. U. R. Strand, M. Kim, A. Georges and F. Baumberger. "High-Resolution Photoemission on Sr_2RuO_4 Reveals Correlation-Enhanced Effective Spin-Orbit Coupling and Dominantly Local Self-Energies". In: *Phys. Rev. X* 9 (2 June 2019), p. 021048. DOI: 10.1103/PhysRevX.9.021048. URL: https://link.aps.org/doi/10.1103/PhysRevX.9.021048.

[42] Yi Lu and Maurits W. Haverkort. "Exact diagonalization as an impurity solver in dynamical mean field theory". In: *The European Physical Journal Special Topics* 226.11 (July 2017), pp. 2549–2564. ISSN: 1951-6401. DOI: 10.1140/epjst/e2017-70042-4. URL: https://doi.org/10.1140/epjst/e2017-70042-4.

[43] Darya Medvedeva, Sergei Iskakov, Friedrich Krien, Vladimir V. Mazurenko and Alexander I. Lichtenstein. "Exact diagonalization solver for extended dynamical mean-field theory". In: *Phys. Rev. B* 96 (23 Dec. 2017), p. 235149. DOI: 10.1103/PhysRevB.96.235149. URL: https://link.aps.org/doi/10.1103/PhysRevB.96.235149.

[44] R. Bulla, T Costi and T. Pruschke. "Numerical renormalization group method for quantum impurity systems". In: *Rev. Mod. Phys.* 80 (2 Apr. 2008), p. 395. DOI: 10.1103/RevModPhys.80.395. URL: http://link.aps.org/doi/10.1103/RevModPhys.80.395.

[45] Emanuel Gull, Andrew J. Millis, Alexander I. Lichtenstein, Alexey N. Rubtsov, Matthias Troyer and Philipp Werner. "Continuous-time Monte Carlo methods for quantum impurity models". In: *Rev. Mod. Phys.* 83 (2 May 2011), pp. 349–404. DOI: 10.1103/RevModPhys.83.349. URL: https://link.aps.org/doi/10.1103/RevModPhys.83.349.

[46] Philipp Werner, Armin Comanac, Luca de'Medici, Matthias Troyer and Andrew J. Millis. "Continuous-Time Solver for Quantum Impurity Models". In: *Phys. Rev. Lett.* 97 (7 Aug. 2006), p. 076405. DOI: 10.1103/PhysRevLett.97.076405. URL: http://link.aps.org/doi/10.1103/PhysRevLett.97.076405.

[47] A. A. Katanin, A. Toschi and K. Held. "Comparing pertinent effects of antiferromagnetic fluctuations in the two- and three-dimensional Hubbard model". In: *Phys. Rev. B* 80 (Aug. 2009), p. 075104. DOI: 10.1103/PhysRevB.80.075104. URL: http://link.aps.org/doi/10.1103/PhysRevB.80.075104.

[48] E. Gull, M. Ferrero, O. Parcollet, A. Georges and A. J. Millis. "Momentum-space anisotropy and pseudogaps: A comparative cluster dynamical mean-field analysis of the doping-driven metal-insulator transition in the two-dimensional Hubbard model". In: *Phys. Rev. B* 82 (15 Oct. 2010), p. 155101. DOI: 10.1103/PhysRevB.82.155101. URL: http://link.aps.org/doi/10.1103/PhysRevB.82.155101.

[49] Emanuel Gull, Olivier Parcollet and Andrew J. Millis. "Superconductivity and the Pseudogap in the Two-Dimensional Hubbard Model". In: *Phys. Rev. Lett.* 110 (21 May 2013), p. 216405. DOI: 10.1103/PhysRevLett.110.216405. URL: http://link.aps.org/doi/10.1103/PhysRevLett.110.216405.

[50] Thomas Schäfer, Nils Wentzell, Fedor Šimkovic, Yuan-Yao He, Cornelia Hille, Marcel Klett, Christian J. Eckhardt, Behnam Arzhang, Viktor Harkov, Fran çois-Marie Le Régent, Alfred Kirsch, Yan Wang, Aaram J. Kim, Evgeny Kozik, Evgeny A. Stepanov, Anna Kauch, Sabine Andergassen, Philipp Hansmann, Daniel Rohe, Yuri M. Vilk, James P. F. LeBlanc, Shiwei Zhang, A.-M. S. Tremblay, Michel Ferrero, Olivier Parcollet and Antoine Georges. "Tracking the Footprints of Spin Fluctuations: A MultiMethod, MultiMessenger Study of the Two-Dimensional Hubbard Model". In: *Phys. Rev. X* 11 (1 Mar. 2021), p. 011058. DOI: 10.1103/PhysRevX.11.011058. URL: https://link.aps.org/doi/10.1103/PhysRevX.11.011058.

[51] A. N. Rubtsov, M. I. Katsnelson and A. I. Lichtenstein. "Dual fermion approach to nonlocal correlations in the Hubbard model". In: *Phys. Rev. B* 77 (Jan. 2008), p. 033101. DOI: 10.1103/PhysRevB.77.033101.

[52] G. Rohringer, A. Toschi, H. Hafermann, K. Held, V. I. Anisimov and A. A. Katanin. "One-particle irreducible functional approach: A route to diagrammatic extensions of the dynamical mean-field theory". In: *Phys. Rev. B* 88 (2013), p. 115112. URL: http://link.aps.org/doi/10.1103/PhysRevB.88.115112.

[53] A. Toschi, A. A. Katanin and K. Held. "Dynamical vertex approximation: A step beyond dynamical mean-field theory". In: *Phys. Rev. B* 75 (4 Jan. 2007), p. 045118. DOI: 10.1103/PhysRevB.75.045118. URL: https://link.aps.org/doi/10.1103/PhysRevB.75.045118.

[54] Josef Kaufmann, Christian Eckhardt, Matthias Pickem, Motoharu Kitatani, Anna Kauch and Karsten Held. "Self-consistent ladder dynamical vertex approximation". In: *Phys. Rev. B* 103 (3 Jan. 2021), p. 035120. DOI: 10.1103/PhysRevB.103.035120. URL: https://link.aps.org/doi/10.1103/PhysRevB.103.035120.

[55] Patrick Kappl, Friedrich Krien, Clemens Watzenböck and Karsten Held. "Nonlinear responses and three-particle correlators in correlated electron systems exemplified by the Anderson impurity model". In: *Phys. Rev. B* 107 (20 May 2023), p. 205108. DOI: 10.1103/PhysRevB.107.205108. URL: https://link.aps.org/doi/10.1103/PhysRevB.107.205108.

[56] M. Jarrell. "Hubbard model in infinite dimensions: A quantum Monte Carlo study". In: *Phys. Rev. Lett.* 69 (1 July 1992), pp. 168–171. DOI: 10.1103/PhysRevLett.69.168. URL: https://link.aps.org/doi/10.1103/PhysRevLett.69.168.

[57] Hiroaki Kusunose. "Influence of Spatial Correlations in Strongly Correlated Electron Systems: Extension to Dynamical Mean Field Approximation". In: *J. Phys. Soc. Jpn.* 75.5 (2006), p. 054713. DOI: 10.1143/JPSJ.75.054713. URL: http://jpsj.ipap.jp/link?JPSJ/75/054713/.

[58] C. Taranto, S. Andergassen, J. Bauer, K. Held, A. Katanin, W. Metzner, G. Rohringer and A. Toschi. "From Infinite to Two Dimensions through the Functional Renormalization Group". In: *Phys. Rev. Lett.* 112 (19 May 2014), p. 196402. DOI: 10.1103/PhysRevLett.112.196402. URL: http://link.aps.org/doi/10.1103/PhysRevLett.112.196402.

[59] Thomas Ayral and Olivier Parcollet. "Mott physics and spin fluctuations: a unified framework". In: *Phys Rev. B* 92 (15 2015), p. 115109. URL: http://link.aps.org/doi/10.1103/PhysRevB.92.115109.

[60] Gang Li. "Hidden physics in the dual-fermion approach: A special case of a nonlocal expansion scheme". In: *Phys. Rev. B* 91 (16 Apr. 2015), p. 165134. DOI: 10.1103/PhysRevB.91.165134. URL: http://link.aps.org/doi/10.1103/PhysRevB.91.165134.

[61] G. Rohringer, A. Toschi, A. Katanin and K. Held. "Critical Properties of the Half-Filled Hubbard Model in Three Dimensions". In: *Phys. Rev. Lett.* 107 (25 Dec. 2011), p. 256402. DOI: 10.1103/PhysRevLett.107.256402. URL: http://link.aps.org/doi/10.1103/PhysRevLett.107.256402.

[62] Andrey E. Antipov, Emanuel Gull and Stefan Kirchner. "Critical Exponents of Strongly Correlated Fermion Systems from Diagrammatic Multiscale Methods". In: *Phys. Rev. Lett.* 112 (22 June 2014), p. 226401. DOI: 10.1103/PhysRevLett.112.226401. URL: http://link.aps.org/doi/10.1103/PhysRevLett.112.226401.

[63] Daniel Hirschmeier, Hartmut Hafermann, Emanuel Gull, Alexander I. Lichtenstein and Andrey E. Antipov. "Mechanisms of finite-temperature magnetism in the three-dimensional Hubbard model". In: *Phys. Rev. B* 92 (14 Oct. 2015), p. 144409. DOI: 10.1103/PhysRevB.92.144409. URL: https://link.aps.org/doi/10.1103/PhysRevB.92.144409.

[64] T. Schäfer, A. A. Katanin, K. Held and A. Toschi. "Interplay of Correlations and Kohn Anomalies in Three Dimensions: Quantum Criticality with a Twist". In: *Phys. Rev. Lett.* 119 (4 July 2017), p. 046402. DOI: 10.1103/PhysRevLett.119.046402. URL: https://link.aps.org/doi/10.1103/PhysRevLett.119.046402.

[65] T. Schäfer, F. Geles, D. Rost, G. Rohringer, E. Arrigoni, K. Held, N. Blümer, M. Aichhorn and A. Toschi. "Fate of the false Mott-Hubbard transition in two dimensions". In: *Phys. Rev. B* 91 (12 Mar. 2015), p. 125109. DOI: 10.1103/PhysRevB.91.125109. URL: http://link.aps.org/doi/10.1103/PhysRevB.91.125109.

[66] Friedrich Krien, Paul Worm, Patrick Chalupa-Gantner, Alessandro Toschi and Karsten Held. "Explaining the pseudogap through damping and antidamping on the Fermi surface by imaginary spin scattering". In: *Communications Physics* 5.1 (Dec. 2022), p. 336. ISSN: 2399-3650. DOI: 10.1038/s42005-022-01117-5. URL: https://doi.org/10.1038/s42005-022-01117-5.

[67] Junya Otsuki, Hartmut Hafermann and Alexander I. Lichtenstein. "Superconductivity, antiferromagnetism, and phase separation in the two-dimensional Hubbard model: A dual-fermion approach". In: *Phys. Rev. B* 90 (23 Dec. 2014), p. 235132. DOI: 10.1103/PhysRevB.90.235132. URL: http://link.aps.org/doi/10.1103/PhysRevB.90.235132.

[68] Motoharu Kitatani, Naoto Tsuji and Hideo Aoki. "FLEX+DMFT approach to the d-wave superconducting phase diagram of the two-dimensional Hubbard model". In: *Phys. Rev. B* 92 (2015), p. 085104. URL: http://link.aps.org/doi/10.1103/PhysRevB.92.085104.

[69] Ado Jorio, Riichiro Saito, Gene Dresselhaus and Mildred S. Dresselhaus. "Quantum Description of Raman Scattering". In: *Raman Spectroscopy in Graphene Related Systems*. Wiley-Blackwell, 2011. Chap. 5, pp. 103–119. ISBN: 9783527632695. DOI: 10.1002/9783527632695.ch5.

[70] Habib Rostami, Mikhail I. Katsnelson and Marco Polini. "Theory of plasmonic effects in nonlinear optics: The case of graphene". In: *Phys. Rev. B* 95 (3 Jan. 2017), p. 035416. DOI: 10.1103/PhysRevB.95.035416. URL: https://link.aps.org/doi/10.1103/PhysRevB.95.035416.

[71] M. Vandelli, M. I. Katsnelson and E. A. Stepanov. "Resonant optical second harmonic generation in graphene-based heterostructures". In: *Phys. Rev. B* 99 (16 Apr. 2019), p. 165432. DOI: 10.1103/PhysRevB.99.165432. URL: https://link.aps.org/doi/10.1103/PhysRevB.99.165432.

[72] Habib Rostami, Mikhail I. Katsnelson, Giovanni Vignale and Marco Polini. "Gauge invariance and Ward identities in nonlinear response theory". In: *Annals of Physics* 431 (2021), p. 168523. ISSN: 0003-4916. DOI: 10.1016/j.aop.2021.168523. URL: https://doi.org/10.1016/j.aop.2021.168523.

[73] Yoshihiro Michishita and Robert Peters. "Effects of renormalization and non-Hermiticity on nonlinear responses in strongly correlated electron systems". In: *Phys. Rev. B* 103 (19 May 2021), p. 195133. DOI: 10.1103/PhysRevB.103.195133. URL: https://link.aps.org/doi/10.1103/PhysRevB.103.195133.

[74] Akira Kofuji, Yoshihiro Michishita and Robert Peters. "Effects of strong correlations on the nonlinear response in Weyl-Kondo semimetals". In: *Phys. Rev. B* 104 (8 Aug. 2021), p. 085151. DOI: 10.1103/PhysRevB.104.085151. URL: https://link.aps.org/doi/10.1103/PhysRevB.104.085151.

[75] Hartmut Hafermann, Kelly R. Patton and Philipp Werner. "Improved estimators for the self-energy and vertex function in hybridization-expansion continuous-time quantum Monte Carlo simulations". In: *Phys. Rev. B* 85 (20 May 2012), p. 205106. DOI: 10.1103/PhysRevB.85.205106. URL: http://link.aps.org/doi/10.1103/PhysRevB.85.205106.

[76] Hartmut Hafermann. "Self-energy and vertex functions from hybridization-expansion continuous-time quantum Monte Carlo for impurity models with retarded interaction". In: *Phys. Rev. B* 89 (23 June 2014), p. 235128. DOI: 10.1103/PhysRevB.89.235128. URL: https://link.aps.org/doi/10.1103/PhysRevB.89.235128.

[77] P. Gunacker, M. Wallerberger, T. Ribic, A. Hausoel, G. Sangiovanni and K. Held. "Worm-improved estimators in continuous-time quantum Monte Carlo". In: *Phys. Rev. B* 94 (12 Sept. 2016), p. 125153. DOI: 10.1103/PhysRevB.94.125153. URL: http://link.aps.org/doi/10.1103/PhysRevB.94.125153.

[78] Alice Moutenet, Wei Wu and Michel Ferrero. "Determinant Monte Carlo algorithms for dynamical quantities in fermionic systems". In: *Phys. Rev. B* 97 (8 Feb. 2018), p. 085117. DOI: 10.1103/PhysRevB.97.085117. URL: https://link.aps.org/doi/10.1103/PhysRevB.97.085117.

[79] J. Kaufmann, P. Gunacker, A. Kowalski, G. Sangiovanni and K. Held. "Symmetric improved estimators for continuous-time quantum Monte Carlo". In: *Phys. Rev. B* 100 (7 Aug. 2019), p. 075119. DOI: 10.1103/PhysRevB.100.075119. URL: https://link.aps.org/doi/10.1103/PhysRevB.100.075119.

[80] L. Kelvin. *Baltimore Lectures on Molecular Dynamics and the Wave Theory of Light*. C. J. Clay and Sons, London, 1904.

[81] Friedrich Krien, Erik G. C. P. van Loon, Hartmut Hafermann, Junya Otsuki, Mikhail I. Katsnelson and Alexander I. Lichtenstein. "Conservation in two-particle self-consistent extensions of dynamical mean-field theory". In: *Phys. Rev. B* 96 (7 Aug. 2017), p. 075155. DOI: 10.1103/PhysRevB.96.075155. URL: https://link.aps.org/doi/10.1103/PhysRevB.96.075155.

[82] Markus Wallerberger, Andreas Hausoel, Patrik Gunacker, Alexander Kowalski, Nicolaus Parragh, Florian Goth, Karsten Held and Giorgio Sangiovanni. "w2dynamics: Local one- and two-particle quantities from dynamical mean field theory". In: *Computer Physics Communications* 235 (2019), pp. 388–399. ISSN: 0010-

4655. DOI: https://doi.org/10.1016/j.cpc.2018.09.007. URL: http://www.sciencedirect.com/science/article/pii/S0010465518303217.

[83] Seung-Sup B. Lee, Fabian B. Kugler and Jan von Delft. "Computing Local Multipoint Correlators Using the Numerical Renormalization Group". In: *Phys. Rev. X* 11 (4 Oct. 2021), p. 041007. DOI: 10.1103/PhysRevX.11.041007. URL: https://link.aps.org/doi/10.1103/PhysRevX.11.041007.

[84] Patrick Kappl. *w2diag*. Version 0.5.0. https://gitlab.tuwien.ac.at/e138/e138-01/software/w2dynamics-tools/w2diag. 2022.

[85] Patrick Kappl and Friedrich Krien. *Numerical results for "Non-linear responses and three-particle correlators in correlated electron systems exemplified by the Anderson impurity model"*. Version 1.0.1. TU Wien, Mar. 2023. DOI: 10.48436/s8mva-42q75.

[86] Z. Alpicheshev. (private communication). 2022.

[87] Friedrich Krien and Anna Kauch. "The plain and simple parquet approximation: single-and multi-boson exchange in the two-dimensional Hubbard model". In: *The European Physical Journal B* 95.4 (Apr. 2022), p. 69. ISSN: 1434-6036. DOI: 10.1140/epjb/s10051-022-00329-6. URL: https://doi.org/10.1140/epjb/s10051-022-00329-6.

[88] Friedrich Krien, Anna Kauch and Karsten Held. "Tiling with triangles: parquet and $GW\gamma$ methods unified". In: *Phys. Rev. Res.* 3 (1 Feb. 2021), p. 013149. DOI: 10.1103/PhysRevResearch.3.013149. URL: https://link.aps.org/doi/10.1103/PhysRevResearch.3.013149.

[89] Hiroshi Shinaoka and Yuki Nagai. "Sparse modeling of large-scale quantum impurity models with low symmetries". In: *Phys. Rev. B* 103 (4 Jan. 2021), p. 045120. DOI: 10.1103/PhysRevB.103.045120. URL: https://link.aps.org/doi/10.1103/PhysRevB.103.045120.

[90] Markus Wallerberger and Karsten Held. "Trie-based ranking of quantum many-body states". In: *Phys. Rev. Res.* 4 (3 Sept. 2022), p. 033238. DOI: 10.1103/PhysRevResearch.4.033238. URL: https://link.aps.org/doi/10.1103/PhysRevResearch.4.033238.

[91] Patrick Kappl, Markus Wallerberger, Josef Kaufmann, Matthias Pickem and Karsten Held. "Statistical error estimates in dynamical mean-field theory and extensions thereof". In: *Phys. Rev. B* 102 (8 Aug. 2020), p. 085124. DOI: 10.1103/PhysRevB.102.085124. URL: https://link.aps.org/doi/10.1103/PhysRevB.102.085124.

[92] Antoine Georges and Gabriel Kotliar. "Hubbard model in infinite dimensions". In: *Phys. Rev. B* 45 (Mar. 1992), pp. 6479–6483. DOI: 10.1103/PhysRevB.45.6479. URL: http://link.aps.org/doi/10.1103/PhysRevB.45.6479.

[93] V I Anisimov, A I Poteryaev, M A Korotin, A O Anokhin and G Kotliar. "First-principles calculations of the electronic structure and spectra of strongly correlated systems: dynamical mean-field theory". In: *Journal of Physics: Condensed Matter* 9 (1997), pp. 7359–7367. URL: http://stacks.iop.org/0953-8984/9/7359.

[94] A. I. Lichtenstein and M. I. Katsnelson. "Ab initio calculations of quasiparticle band structure in correlated systems: LDA++ approach". In: *Phys. Rev. B* 57 (Mar. 1998), pp. 6884–6895. DOI: 10.1103/PhysRevB.57.6884.

[95] K. Held, I. A. Nekrasov, G. Keller, V. Eyert, N. Blümer, A. K. McMahan, R. T. Scalettar, Th. Pruschke, V. I. Anisimov and D. Vollhardt. "Realistic investigations of correlated electron systems with LDA + DMFT". In: *physica status solidi (b)* 243.11 (2006). previously appeared as Psi-k Newsletter No. 56 (April 2003), pp. 2599–2631. ISSN: 1521-3951. DOI: 10.1002/pssb.200642053. URL: http://dx.doi.org/10.1002/pssb.200642053.

[96] M. Ulmke, V. Jani š and D. Vollhardt. "Anderson-Hubbard model in infinite dimensions". In: *Phys. Rev. B* 51 (16 Apr. 1995), pp. 10411–10426. DOI: 10.1103/PhysRevB.51.10411. URL: https://link.aps.org/doi/10.1103/PhysRevB.51.10411.

[97] K. Held, M. Ulmke, N. Blümer and D. Vollhardt. "Correlated-electron theory of strongly anisotropic metamagnets". In: *Phys. Rev. B* 56 (22 Dec. 1997), pp. 14469–14480. DOI: 10.1103/PhysRevB.56.14469. URL: https://link.aps.org/doi/10.1103/PhysRevB.56.14469.

[98] M. H. Hettler, M. Mukherjee, M. Jarrell and H. R. Krishnamurthy. "Dynamical cluster approximation: Nonlocal dynamics of correlated electron systems". In: *Phys. Rev. B* 61 (19 May 2000), pp. 12739–12756. DOI: 10.1103/PhysRevB.61.12739. URL: http://link.aps.org/doi/10.1103/PhysRevB.61.12739.

[99] Rupert G. Miller. "A Trustworthy Jackknife". In: *Ann. Math. Statist.* 35.4 (Dec. 1964), pp. 1594–1605. DOI: 10.1214/aoms/1177700384. URL: https://doi.org/10.1214/aoms/1177700384.

[100] Rupert G. Miller. "The Jackknife–A Review". In: *Biometrika* 61.1 (1974), pp. 1–15. ISSN: 00063444. URL: http://www.jstor.org/stable/2334280.

[101] Emanuel Gull, Andrew J. Millis, Alexander I. Lichtenstein, Alexey N. Rubtsov, Matthias Troyer and Philipp Werner. "Continuous-time Monte Carlo methods for quantum impurity models". In: *Rev. Mod. Phys.* 83.2 (May 2011), p. 349. DOI: 10.1103/RevModPhys.83.349. URL: http://link.aps.org/doi/10.1103/RevModPhys.83.349.

[102] Anna Galler, Patrik Thunström, Josef Kaufmann, Matthias Pickem, Jan M. Tomczak and Karsten Held. "The AbinitioDΓA Project v1.0: Non-local correlations beyond and susceptibilities within dynamical mean-field theory". In: *Computer Physics Communications* 245 (2019), p. 106847. ISSN: 0010-4655. DOI: https://doi.org/10.1016/j.cpc.2019.07.012. URL: http://www.sciencedirect.com/science/article/pii/S0010465519302243.

[103] P. Gunacker, M. Wallerberger, E. Gull, A. Hausoel, G. Sangiovanni and K. Held. "Continuous-time quantum Monte Carlo using worm sampling". In: *Phys. Rev. B* 92 (15 Oct. 2015), p. 155102. DOI: 10.1103/PhysRevB.92.155102. URL: http://link.aps.org/doi/10.1103/PhysRevB.92.155102.

[104] Nicolaus Parragh, Alessandro Toschi, Karsten Held and Giorgio Sangiovanni. "Conserved quantities of $SU(2)$-invariant interactions for correlated fermions and the advantages for quantum Monte Carlo simulations". In: *Phys. Rev. B* 86 (15 Oct. 2012), p. 155158. DOI: 10.1103/PhysRevB.86.155158. URL: http://link.aps.org/doi/10.1103/PhysRevB.86.155158.

[105] Josef Kaufmann, Patrik Gunacker and Karsten Held. "Continuous-time quantum Monte Carlo calculation of multiorbital vertex asymptotics". In: *Phys. Rev. B* 96 (3 July 2017), p. 035114. DOI: 10.1103/PhysRevB.96.035114. URL: https://link.aps.org/doi/10.1103/PhysRevB.96.035114.

[106] Bradley Efron. *The Jackknife, the Bootstrap and Other Resampling Plans*. Philadelphia, Pennsylvania: Society for Industrial and Applied Mathematics, 1982. DOI: 10.1137/1.9781611970319. URL: https://statistics.stanford.edu/sites/g/files/sbiybj6031/f/BIO%5C%2063.pdf.

[107] B. Efron. "Bootstrap Methods: Another Look at the Jackknife". In: *Ann. Statist.* 7.1 (Jan. 1979), pp. 1–26. DOI: 10.1214/aos/1176344552. URL: https://doi.org/10.1214/aos/1176344552.

[108] R.R. Wilcox. *Fundamentals of Modern Statistical Methods: Substantially Improving Power and Accuracy*. Springer New York, 2010. ISBN: 9781441955241. URL: https://books.google.at/books?id=uUNGzhdxk0kC.

[109] Jan Kuneš. "Efficient treatment of two-particle vertices in dynamical mean-field theory". In: *Phys. Rev. B* 83 (8 Feb. 2011), p. 085102. DOI: 10.1103/PhysRevB.83.085102. URL: http://link.aps.org/doi/10.1103/PhysRevB.83.085102.

[110] Mark Jarrell and J. E. Gubernatis. "Bayesian inference and the analytic continuation of imaginary-time quantum Monte Carlo data". In: *Physics Reports* 269.3 (1996), pp. 133–195. ISSN: 0370-1573. DOI: DOI:10.1016/0370-1573(95)00074-7. URL: http://www.sciencedirect.com/science/article/B6TVP-3VTNGGS-3/2/5f7d5c3a6ee0870df8970b51e47592d2.

[111] D. Geffroy, J. Kaufmann, A. Hariki, P. Gunacker, A. Hausoel and J. Kune š. "Collective Modes in Excitonic Magnets: Dynamical Mean-Field Study (Supplemental material)". In: *Phys. Rev. Lett.* 122 (12 Mar. 2019), p. 127601. DOI: 10.1103/PhysRevLett.122.127601. URL: https://link.aps.org/doi/10.1103/PhysRevLett.122.127601.

[112] Josef Kaufmann. *Ana-cont*. https://github.com/josefkaufmann/ana_cont.git. 2019.

[113] J. M. Luttinger. "Analytic Properties of Single-Particle Propagators for Many-Fermion Systems". In: *Phys. Rev.* 121 (4 Feb. 1961), pp. 942–949. DOI: 10.1103/PhysRev.121.942. URL: https://link.aps.org/doi/10.1103/PhysRev.121.942.

[114] Martin Bercx, Florian Goth, Johannes S. Hofmann and Fakher F. Assaad. "The ALF (Algorithms for Lattice Fermions) project release 1.0. Documentation for the auxiliary field quantum Monte Carlo code". In: *SciPost Phys.* 3 (2 2017), p. 013. DOI: 10.21468/SciPostPhys.3.2.013. URL: https://scipost.org/10.21468/SciPostPhys.3.2.013.

[115] Patrick Kappl. *jackknife*. https://gitlab.com/PatrickKappl/jackknife. 2019.

[116] Hartmut Hafermann, Kelly R. Patton and Philipp Werner. "Improved estimators for the self-energy and vertex function in hybridization-expansion continuous-time quantum Monte Carlo simulations". In: *Phys. Rev. B* 85 (20 May 2012), p. 205106. DOI: 10.1103/PhysRevB.85.205106. URL: https://link.aps.org/doi/10.1103/PhysRevB.85.205106.

[117] Nils Wentzell, Gang Li, Agnese Tagliavini, Ciro Taranto, Georg Rohringer, Karsten Held, Alessandro Toschi and Sabine Andergassen. "High-frequency asymptotics of the vertex function: Diagrammatic parametrization and algorithmic implementation". In: *Phys. Rev. B* 102 (8 Aug. 2020), p. 085106. DOI: 10.1103/PhysRevB.102.085106. URL: https://link.aps.org/doi/10.1103/PhysRevB.102.085106.

[118] Motoharu Kitatani, Thomas Schäfer, Hideo Aoki and Karsten Held. "Why the critical temperature of high-T_c cuprate superconductors is so low: The importance of the dynamical vertex structure". In: *Phys. Rev. B* 99 (4 Jan. 2019), p. 041115. DOI: 10.1103/PhysRevB.99.041115. URL: https://link.aps.org/doi/10.1103/PhysRevB.99.041115.

[119] Friedrich Krien. "Efficient evaluation of the polarization function in dynamical mean-field theory". In: *Phys. Rev. B* 99 (23 June 2019), p. 235106. DOI: 10.1103/PhysRevB.99.235106. URL: https://link.aps.org/doi/10.1103/PhysRevB.99.235106.

[120] A. Katanin. "Improved treatment of fermion-boson vertices and Bethe-Salpeter equations in nonlocal extensions of dynamical mean field theory". In: *Phys. Rev. B* 101 (3 Jan. 2020), p. 035110. DOI: 10.1103/PhysRevB.101.035110. URL: https://link.aps.org/doi/10.1103/PhysRevB.101.035110.

[121] Lewin Boehnke, Hartmut Hafermann, Michel Ferrero, Frank Lechermann and Olivier Parcollet. "Orthogonal polynomial representation of imaginary-time Green's functions". In: *Phys. Rev. B* 84 (7 Aug. 2011), p. 075145. DOI: 10.1103/PhysRevB.84.075145. URL: https://link.aps.org/doi/10.1103/PhysRevB.84.075145.

[122] Hiroshi Shinaoka, Junya Otsuki, Kristjan Haule, Markus Wallerberger, Emanuel Gull, Kazuyoshi Yoshimi and Masayuki Ohzeki. "Overcomplete compact representation of two-particle Green's functions". In: *Phys. Rev. B* 97 (20 May 2018), p. 205111. DOI: 10.1103/PhysRevB.97.205111. URL: https://link.aps.org/doi/10.1103/PhysRevB.97.205111.

[123] Hiroshi Shinaoka, Dominique Geffroy, Markus Wallerberger, Junya Otsuki, Kazuyoshi Yoshimi, Emanuel Gull and Jan Kuneš. "Sparse sampling and tensor network representation of two-particle Green's functions". In: *SciPost Phys.* 8 (1 2020), p. 12. DOI: 10.21468/SciPostPhys.8.1.012. URL: https://scipost.org/10.21468/SciPostPhys.8.1.012.

[124] Christian J. Eckhardt, Patrick Kappl, Anna Kauch and Karsten Held. "A functional-analysis derivation of the parquet equation". In: *SciPost Phys.* 15 (2023), p. 203. DOI: 10.21468/SciPostPhys.15.5.203. URL: https://scipost.org/10.21468/SciPostPhys.15.5.203.